CONFORMAL SOL-GEL COATINGS ON THREE-DIMENSIONAL NANOSTRUCTURED TEMPLATES

A Dissertation
Presented to
The Academic Faculty

By

Michael R. Weatherspoon

In Partial Fulfillment
Of the Requirements for the Degree
Doctor of Philosophy in the
School Materials Science and Engineering

Georgia Institute of Technology

April 2008

CONFORMAL SOL-GEL COATINGS ON THREE-DIMENSIONAL NANOSTRUCTURED TEMPLATES

Approved by:

Dr. Kenneth H. Sandhage, Advisor
School of Materials Science and Engineering
Georgia Institute of Technology

Dr. E. Kent Barefield
School of Chemistry and Biochemistry
Georgia Institute of Technology

Dr. W. Brent Carter
School of Materials Science and Engineering
Georgia Institute of Technology

Dr. Uwe H. F. Bunz
School of Chemistry and Biochemistry
Georgia Institute of Technology

Dr. Rina Tannenbaum
School of Materials Science and Engineering
Georgia Institute of Technology

Date Approved: December 7, 2007

To my loving family, Kendra, Sydney, and Jake

ACKNOWLEDGEMENTS

I would like to sincerely express my gratitude to my advisor, Professor Kenneth H. Sandhage, for his guidance, kindness, and support which he has shown to me and my family during our time here at the Georgia Institute of Technology. Dr. Sandhage has gone out of his way on many occasions to help me personally to develop as a scientist and to support my family. I would also like to thank my committee members, Profs. Brent Carter, Rina Tannenbaum, E. Kent Barefield, and Uwe Bunz for their suggestions and valuable advice. I have had the distinct pleasure of working with some of the brightest and most talented individuals while working in Dr. Sandhage's group. I would like to thank my lab mates, Matthew Dickerson, Samuel Shian, Phillip Graham, Zihao Bao, Shawn Allen, David Lipke, Eric Ernst, Dr. Yunnan Fang, Dr. Ye Cai, Dr. Ben Church, and Dr. Michael Haluska for their scientific advice, technical skills, and willingness to discuss ideas. In addition, I would like to thank Todd Walters for his friendship, example, and willingness to help me with SEM related problems. The MSE faculty, administrative, and financial staffs have also been an extreme pleasure to work with. I would like to especially thank Susan Bowman and Mechelle Kitchings for their friendly help in dealing with academic and financial questions and problems.

I have been blessed with many more significant influences throughout my life that have always supported me and encouraged me to accomplish my dreams. My parents, David and Denice Weatherspoon, have instilled within me the desire to work hard and never give up in any circumstance. My in-laws have also been a great source of support and encouragement even though I dragged their daughter and grandchildren across the

country in search of a higher education in the beautiful South. I would have never been able to accomplish this endeavor without the love and support of my wife, Kendra. She has encouraged me through my deepest trials and celebrated with me in my miniscule and significant accomplishments. She has made our experience extremely enjoyable by planning family retreats to venture out on weekends which have broadened our educational experience by attending many cultural Southern activities throughout the South. We have truly accomplished this grand feat together. My children, Sydney and Jake, have also shown me unconditional love and provided many opportunities to set the books down to wrestle, shoot some hoops, play catch, ride bikes, or take a swim which relieved the stresses and monotony of research.

This research was supported by the Air Force Office of Scientific Research (Dr. Joan Fuller and Dr. Hugh DeLong, program managers) and the Office of Naval Research (Dr. Mark Spector, program manager).

TABLE OF CONTENTS

LIST OF FIGURES

SUMMARY

Sol-gel processing techniques, such as spin coating and dip coating, have successfully been utilized over the past several decades to apply conformal coatings on planar substrates; however, controlled film growth on three-dimensional (3-D) nanostructured templates using the sol-gel process remains a significant challenge. Obstacles such as, uncontrolled hydrolyzation and condensation of metal alkoxide precursors on nanostructured surfaces are a few of the obstacles which lead to coatings with undesirable thicknesses and excess inorganic particles. A little over a decade ago, a surface sol-gel process was developed which utilizes stepwise film growth of anhydrous metal alkoxide precursors with hydroxylated surfaces. The surface sol-gel process provides control over the applied coating thickness and is viewed as a wet chemical analog to atomic layer deposition (ALD).

The work presented in this dissertation has focused on applying conformal sol-gel derived coatings with controlled thicknesses on 3-D nanostructured templates. The templates utilized in this work were derived from biological species, such as diatoms and butterflies, as well as a synthetic photoresist polymer (SU-8). Coatings were applied on the templates using a conventional reflux/evaporation deposition process and a custom-built computer controlled surface sol-gel pumping system. The coatings applied using the reflux/evaporation process yielded conformal coatings with uncontrolled film thicknesses whereas the coatings applied using the surface sol-gel process yielded conformal coatings with controlled thicknesses.

Barium titanate and europium-doped barium titanate coatings were applied on diatom frustules using the reflux/evaporation deposition process. The silica-based diatom frustules had to first be converted into magnesia/silicon composite replicas using a gas/solid displacement reaction to render the template chemically compatible with the barium titanate-based coating. Conformal titanate-based coatings were obtained on the magnesia frustule replicas possessing uncontrolled thicknesses and excess inorganic particles using the reflux/evaporation deposition process. The europium-doped barium titanate coated frustules exhibited bright red photoluminescent properties upon stimulation with an ultraviolet light source.

Silica-based diatom frustules were also utilized as 3-D nanostructured templates for fabrication of a micro-scale nitric oxide gas sensor. Tin oxide coatings were applied on the silica frustules using the automated surface sol-gel pumping system. An organic dendrimer method was developed for amplifying hydroxyl groups on the silica frustule surfaces to enhance the surface sol-gel deposition process. Conformal coatings with controlled thicknesses were obtained on the hydroxyl amplified frustule surfaces; however, little if any deposition was observed on the frustules that were not subjected to the hydroxyl amplification process. A single tin oxide coated diatom frustule served as a gas sensor component which was sensitive to very low concentrations of nitric oxide gas.

The automated surface sol-gel system was also used to apply multicomponent tin oxide-doped titania alkoxide chemistries on the wing scales of a blue Morpho butterfly. The alkoxide solutions reacted directly with the OH functionalities provided by the native chitin chemistry of the scales. The tin oxide served as a rutile nucleating agent which allowed the titania to completely crystallize in the high refractive index rutile titania

phase with doping concentrations of tin oxide as low as 7 mol% after annealing at 450^{o}C. The tin oxide-doped titania coatings were both nanocrystalline and nanothick and replicated the nanostructured scales with a high degree of accuracy. Undoped titania coatings applied on the scales required a heat treatment of 900^{o}C to crystallize the coating in the rutile titania phase which led to adverse coarsening effects which destroyed the nanostructed features of the scales.

Tin oxide-doped titania coatings were also deposited on synthetic polymer (SU-8) photonic crystal structures using the automated surface sol-gel process. The hydroxyl concentration on the SU-8 surface was amplified using tris(hydroxymethyl)amino-methane which decreased the hydrophobicity of the SU-8 template and provided reactive OH functionalities for surface sol-gel deposition of the tin oxide-doped titania alkoxide precursor. The coating was crystallized in an acidic solution at 80^{o}C which led to the formation of rutile titania inverse opal photonic crystal structures which maintained the overall structure and ordering of the template. The underlying SU-8 template was successfully removed using an oxygen plasma etch.

CHAPTER 1

INTRODUCTION

1.1 Research Motivation

Materials fabricated using templates in multifarious forms are encountered throughout our daily lives. Clothing, automobiles, aircraft, computers, are all created using template-assisted fabrication to save time and ensure accuracy during mass production. Biology also utilizes template-assisted fabrication for mass production purposes; in fact, DNA (the basic building block of life) serves as a template for RNA synthesis [1]. Thus, templates themselves can be made from nucleic acids, metals, plastics, or even cloth which may or may not be incorporated into the final structure. The template possesses architectural designs and engineering properties which are required for building the desired structure. Mankind has become highly skilled at utilizing template-assisted assembly for mass producing very large three-dimensional (3-D) structures such as trains, planes, and automobiles; however, we continue to struggle in the mass production of very small 3-D structures, especially on the nanoscale.

Nanostructures possess dimensions lying between one nanometer (nm) to one-thousand nanometers. It is therefore little wonder that we struggle to fabricate nanostructures that cannot be seen without the aid of electron microscopy. However, our fascination with nanostructured materials stems from the fact that the properties of materials can change drastically at the nanoscale. For example, sensors become more sensitive and efficient due to an increase in the surface area per unit volume of the material [2], and skillfully engineered nanoporous materials (photonic crystals) can guide

or even trap light [3, 4]. Such applications would provide major technological advances in the fields of medicine, quantum computing, lighting, and solar cells [5-8].

The advent of the scanning electron microscope (SEM) and the atomic force microscope (AFM) enables topographical features to be viewed down to several nanometers. Later advances in the development of lithographic techniques, such as electron beam lithography or focused ion beam (FIB) milling, have opened many avenues which allow for patterning or manipulating nanostructures [9-12]. However, such equipment costs hundreds of thousands of dollars and requires a high degree of skill to operate. Besides being expensive, creating nanostructures using such tools requires a lot of time which in turn leads to low production capability [13].

While mankind continues to struggle with manufacturing nanostructured materials, Nature is well adept at mass producing nanostructures (both polymeric and ceramic) with high finesse which serve specific purposes. For example, certain beetles and butterflies possess nanoporous photonic crystal-like structures that are constructed from the biopolymer, chitin, which interacts with electromagnetic radiation (light) thereby producing brilliant reflections of colored light [14, 15]. Such bright reflections serve as signaling mechanisms to startle predators or to attract a mate [14].

Other nanostructured microorganisms can be found in aquatic environments. For example, diatoms are unicellular micro-algae which incorporate silicic acid from their surroundings to form a rigid 3-D amorphous silica cell wall called a frustule [16, 17]. Frustule dimensions usually range from 20-200 μm in diameter and possess intricate nanopore structures [16]. It is estimated that there are over 100,000 different diatom species, each of which possesses a unique frustule morphology [18, 19]. Through the

process of self division, a single parent diatom can generate enormous numbers of daughter diatoms with frustules of identical shape. For example, 40 continuous reproduction cycles from a single parent diatom would yield more than 1 trillion (2^{40}) descendent diatoms, each with the same frustule morphology [18, 19]. No man-made process is currently capable of directly generating such precisely-replicated 3-D microscale, nanostructured assemblies n such a massive scale under ambient conditions. And herein lies a portion of the motivation behind the work presented in this dissertation; to utilize Nature's skillful nanoengineering abilities as a means of massively producing low cost nanostructures that we can use as templates for generating new devices. However, the chemical composition of the silica frustule or the chitin butterfly wing must be altered in order to utilize the precision and massive parallelism of such biological assembly for a variety of nanostructured devices possessing desirable optical, electronic, magnetic, chemical, or other properties.

Nanocoating is a versatile method for replicating nanoscale entities with new chemical compositions. Successful nanocoating techniques must possess the ability to apply conformal and continuous coatings. There are several deposition techniques which have been utilized for coating materials such as chemical vapor deposition (CVD) [20], pulsed laser deposition (PLD) [21], magnetron sputtering [22], atomic layer deposition [23], dip coating [24], sol-gel coating [25], and electrochemical deposition [26]. Conformal and continuous nanocoatings cannot be realized on 3-D templates using line-of-sight PLD and magnetron sputtering techniques due to shadowing effects. Of the above deposition techniques we believe that the sol-gel process is a cheap and versatile technique for coating complex shaped 3-D nanostructures. There are however a number

of issues which must first be overcome to enable the sol-gel process to reliably produce controlled, conformal, and continuous coatings on nanostructured templates. This dissertation seeks to address these issues.

The first issue to be dealt with in coating nanostructured templates using typical sol-gel processing is control over the coating thickness. A variety of sol-gel coatings that have been applied to nanostructured templates in the literature utilize a complete submersion protocol [27-30]. Control over the coating thickness is dependent upon variables such as reactant concentration, aging time, pH, and temperature [30]. The presence of so many variables requires optimization of the reaction conditions (for a given template) and careful monitoring to allow for reproducible results. Other factors such as syneresis (spontaneous shrinkage) of the gel leads to contraction of the gel network as a result of bond formation and expulsion of liquid from the pores which reduces the volume of the gel by a factor of 5 to 10 compared to the wet gel and introduces stress in the system [31]. This stress is usually manifested in the form of cracks in the coating. Aggregation of the templates in solution is another possibility when using submersion sol-gel processing due to the formation of polymer networks between the templates. As R. A. Caruso and M. Antionetti stated, "One of the main challenges in coating nanostructured templates is to achieve a homogeneous layer of the inorganic material without the formation of free (excess) inorganic particles in solution" [32].

In 1996 Kunitake *et al*. introduced the surface sol-gel process, which enables molecular-scale control of film thickness on hydroxylated substrates [33]. This process is self-limited and is viewed as a wet chemical analog of atomic layer deposition (ALD).

The self-limiting factor is based upon the consumption of surface hydroxyl groups via nucleophillic reaction between the surface hydroxyls and a metal-alkoxide precursor by which metal-oxide bonds are covalently grafted to the surface. The chemisorbed alkoxide layer is then rehydrolyzed with water to regenerate hydroxyl groups for continued step-wise film growth [33, 34]. In their first publication, Kunitake *et al*. stated, "this process, in principle, can be applied to various material surfaces irrespective of their shape and size, if the surface is modified with hydroxyl group" [33]. Since this time there has been some 160 or so publications that have utilized the surface sol-gel process for obtaining controlled, conformal, and continuous coatings on surfaces such as, metallic surfaces [33-45], latex polymer surfaces [46-50], cellulose [51-56], DNA and mosaic viruses [47, 57], microcontact-printed self assembled monolayers [58], and mesoporous silica materials [59, 60]. While this is not an exhaustive list, it serves to demonstrate the wide range of applicable substrates that may be utilized by this process for obtaining controlled film growth of metal oxides. However, there are certain aspects of this process which can be improved to enable it to become a versatile alternative to more expensive layer-by-layer deposition techniques such as ALD.

Over the past several years, the surface sol-gel process has been conducted under atmospheric conditions. Metal-alkoxide precursors are generally used due to their highly reactive nature and susceptibility towards nucleophilic attack; however, under atmospheric conditions the alkoxide will adsorb moisture from the air which can cause the formation of oligomers or precipitation of the stock solutions leading to abnormal film growth. Accordingly, Kunitake *et al*. has reported that the stock solution has to be replaced with fresh solution after every 4-5 deposition cycles to maintain normal film

growth behavior [33]. Only one article has been published (of the 160) in which the depositions were performed under dry conditions achieved within a filtration flask sealed with a rubber septum and equipped with a stopcock on the filtration end of the assembly [59]. In the past, this process has also required appreciable manual labor (e.g., repetitive dipping of substrates into solutions, or adding solutions to filtration flasks). Both of the above short comings were addressed in this thesis research by engineering an automated surface sol-gel deposition system inside of a dry, inert atmosphere glove box.

The driving motivation behind the work presented in this dissertation was to develop an inexpensive and highly versatile automated sol-gel based deposition tool capable of applying controlled, conformal, and continuous metal oxide coatings on nanostructured templates, thereby endowing them with new materials properties. Nanostructured ceramic, biopolymer, and synthetic polymer templates were coated using this tool to demonstrate its versatility. Surface functionalization protocols were also developed to allow for an amplification of reactive hydroxyl groups on both the ceramic and synthetic polymer templates to allow for continuous film growth.

1.2 Chemical Systems Studied

In this dissertation, three different sol-gel chemistries were examined: barium titanate ($BaTiO_3$) derived from barium titanium ethyl-hexano isopropoxide, tin oxide (SnO_2) derived from tin (IV) isopropoxide, and titania (TiO_2) derived from titanium (IV) isopropoxide.

Barium titanate is a wide band gap (~ 3 eV [61]) perovskite ceramic compound with attractive electronic, optical, ferroelectric, and piezoelectric properties and has been used in numerous device applications, such as capacitors, thermistors, sensors,

waveguides, and actuators [62]. Barium titanate possesses a relatively high solid solubility for a variety of rare earth activator cations (e.g., Ce, Nd, Sm, Eu, Gd, Dy, Ho, Er) [61, 63-65] and can therefore be utilized as a lattice for phosphor materials. The properties of many phosphor materials are dependent upon the size distribution of the particles [66, 67]. There are numerous diatom species which possess sizes which lie within the optimum phosphor particle size range of 1-8 microns [16]. Therefore, diatom frustules were coated with rare earth doped barium titanate to endow the frustules with phosphorescent properties.

Titania exists in three main crystallographic phases. Anatase (tetragonal) and brookite (orthorhombic) are common metastable phases, while rutile (tetragonal) is the stable phase at ambient pressure. Each crystalline phase has different properties that are desired for different applications. Anatase is attractive for photocatalytic and bioremediation purposes [68] while rutile is highly sought after for use in photonic crystal applications due to its high refractive index [69]. However, considerable grain growth and sintering occur during the anatase to rutile phase transformation at elevated temperatures which makes it difficult to obtain nanocoatings capable of replicating the periodic nanostructure of a photonic crystal template [70-85]. There is one demonstration, however, which utilized a template of liquid oil droplets in an emulsion that was stabilized by surfactant and suspended in a titania sol to generate rutile titania with 70 nm grain sizes [83]. However, the polydispersity of the emulsion template prevented long range order in the resulting particle assembly. A method for producing rutile titania nanocoatings on ordered, nanostructured templates is still needed and will be discussed more fully in Chapters 5 and 6 of this dissertation.

Tin oxide is a well known semiconducting material and has been utilized as a sensor for detecting polluting, poisonous, and explosive gases, such as NO_x, NO_2, CO, H_2 [86-91]. Tin oxide (cassiterite) crystallizes in the tetragonal rutile phase at ambient pressure [92, 93]. This is of significance because it can be utilized as a rutile template for other materials. For example, doping titania sols with tin oxide has been shown to be an effective method for producing rutile titania at much lower temperatures and with much smaller grain sizes [92-94]. As shown in Chapters 5 and 6, rutile titania nanocoatings can be realized by doping the titanium isopropoxide solution with tin isopropoxide.

1.3 The Sol-Gel Process

1.3.1 Basic Sol-Gel Reactions and Terminology

Sol-gel processing provides a highly versatile "wet chemical" approach for the fabrication of homogeneous multicomponent ceramics [95]. The *sol* consists of a well mixed colloidal suspension of solid particles in a liquid. These particles are so small (~1-1000 nm) that surface charges and van der Waals forces dominate any interactions of the molecules [31, 96]. Precursors used to prepare a colloidal *sol* usually consist of metal organics, metals, or inorganic salts dissolved in an organic liquid. Metal alkoxide precursors are distinguishable from organometallic precursors in that alkoxides are stabilized with metal-oxygen-carbon bonds, whereas organometallics are stabilized with direct metal-carbon bonds [95]. The use of metal alkoxide, $M(OR)_n$, precursors is the most popular in sol-gel processing because the metal has been stabilized in its highest oxidation state by the electronegative OR groups, which renders the metal group quite susceptible to nucleophilic attack by water or OH groups [31].

The chemistry of the sol-gel process is based on hydroxylation and condensation of molecular precursors [31]. When alkoxides react with water, a hydroxyl moiety becomes attached to the metal atom. This reaction is called hydrolysis and is described by the following reaction:

$$M(OR)_n + H_2O \Rightarrow HO\text{-}M(OR)_{n-1} + ROH \quad (1.1)$$

where M represents the metal and R the alkyl group (e.g., ethyl, *i*-propyl, *n*-butyl etc). Hydrolysis may go to completion if the alkoxide is reacted with enough water, resulting in all of the OR groups being replaced by OH groups [95]. Condensation takes place when two partially hydrolyzed molecules link together and liberate a small molecule, such as water or alcohol according to the following reaction:

$$(OR)_nM\text{-}OH + HO\text{-}M(OR)_n \Rightarrow (OR)_nM\text{-}O\text{-}M(OR)_n + H_2O \quad (1.2)$$

This reaction can continue so as to build a larger molecular network through the process of polymerization [31].

Less reactive precursors can be catalyzed using either an acid or a base to help control the hydrolysis and condensation processes. Usually the pH of the water that is added during the hydrolysis step is altered using acids such as HCl and HNO_3, or a base such as NH_3 or NaOH. In the case where an acid catalyst is used, the negatively charged alkoxy groups can be protonated by H_3O^+ ions [95]. By adding an acidic catalyst to less reactive alkoxide precursors (e.g., alkoxysilanes), the hydrolysis rate can be greatly

enhanced resulting in all of the OR groups being hydrolyzed as long as enough water is added [97, 98]. On the other hand, basic catalysts tend to activate the condensation reaction resulting in highly cross-linked polymers and particulate gels [99].

The hydrolysis and condensation reactions can both generally be activated by increasing the solution temperature. As a result, the hydrolysis and condensation rates of less reactive alkoxides can be improved by increasing the temperature. On the other hand, for highly-reactive precursors such as transition metal oxides, the reaction temperature can be lowered in order to slow down the hydrolysis and condensation processes. Other factors such as alkoxide concentration, solvent evaporation, and nature of the solvent can also contribute to the hydrolysis and condensation processes [95].

Once the polymerization event is completed, and the molecular network has been extended throughout the solution, the substance is said to be a *gel* [31]. Gels can be considered as multiphase systems in which the solvent molecules are trapped inside a continuous oxide polymer network [95]. Thus, it would be possible to travel from one side of the sample to the other in the solid phase without ever having to enter the liquid phase. Such continuity provides the gel with elastic characteristics [31]. However, upon evaporation of the volatile solvent, the volume of the gel network can be reduced by a factor of 5 to 10 compared to the original wet gel [31]. Uncontrolled evaporation (*e.g.*, firing gel films with a rapid heating rate) can lead to surface defects such as voids and mud cracking [31].

Due to the amorphous nature of gel films, subsequent heat treatments are required to obtain a desired crystalline phase. Heat treating generally leads to a volume decrease of the oxide network since the crystalline phase tends to have a higher density than the

amorphous phase. Thus, densely packed metal oxide gel films are desired to minimize discontinuities and voids in the crystalline film. Heat treating may also lead to cracking or spalling of the coating material due to stresses which arise from large mismatches in the coefficients of thermal expansion between the underlying substrate and the applied sol-gel coating.

1.3.2 The Surface Sol-Gel Process

The surface sol-gel process separates the hydrolysis and condensation reactions into separate steps which are illustrated in Figures 1.1(a-e) [33]. Surfaces bearing hydroxyl groups (Figure 1.1(a)) are a prerequisite to obtain conformal and continuous film growth using the surface sol-gel process. The first step involves a nucleophilic reaction between the OH groups and the metal groups of the alkoxide (Figure 1.1(b)), which yields a metal oxide bond that is covalently grafted to the surface (Figure 1.1(c)). After this step, the substrate is rinsed with an anhydrous solvent to remove any physisorbed alkoxide. This is an essential step to maintain uniform film growth and to avoid forming nodule-like precipitates on the surface. The unreacted alkoxy groups of the chemisorbed alkoxide are then fully hydrolyzed with water (Figure 1.1(d)) through another nucleophilic reaction to regenerate reactive OH groups (Figure 1.1(e)) available for further film growth by repeating the steps in the process.

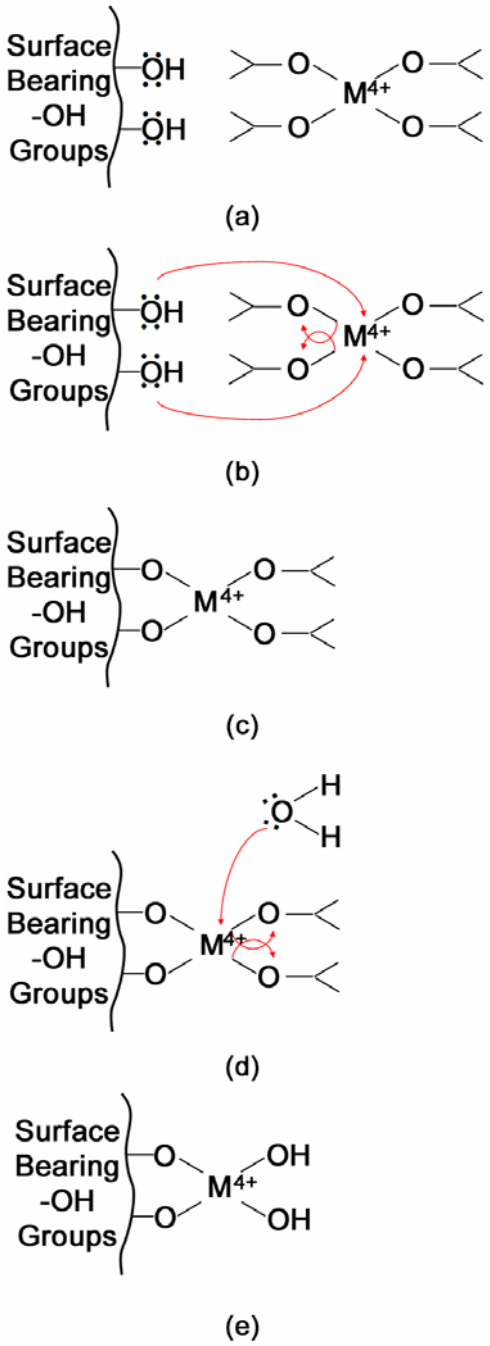

Figure 1.1: The surface sol-gel process employs hydroxylated surfaces and anhydrous metal alkoxide precursors (a) which undergo nucleophilic surface reactions (b) to obtain a metal-oxide bond which is covalently grafted to the surface (c). Further film growth requires hydrolysis of any unbound alkoxy groups by water (d) to regenerate OH groups (e) for continued growth.

1.4 References

[1] D. Voet, J. G. Voet, C. W. Pratt, *Fundamentals of Biochemistry*, John Wiley & Sons, New York (1999).

[2] Z. Bao, M. R. Weatherspoon, S. Shian, Y. Cai, P. D. Graham, S. M. Allan, G. Ahmad, M. D. Dickerson, B. C. Church, Z. Kang, H. W. Abernathy III, C. J. Summers, M. Liu, K. H. Sandhage, *Nature*, **446,** 172-175 (2007).

[3] E. Yablonovitch, *Physical Review Letters*, **58**, 2059-2062 (1987).

[4] S. John, *Physical Review Letters*, **58**, 2486-2489 (1987).

[5] T. Wilk, S. C. Webster, A. Kuhn, G. Rempe, *Science*, **317**, 488 (2007).

[6] J.-Y. Kim, M.-K. Kwon, K.-S. Lee, S.-J. Park, S. H. Kim, K.-D. Lee, *Applied Physics Letters*, **91**, 181109 (2007).

[7] L. Zeng, Y. Yi, C. hong, B. A. Alamariu, J. Liu, X. Duan, L. C. Kimerling, *Materials Research Society Symposium Proceedings*, **891**, 251-256 (2005).

[8] Y. A. Morch, I. Donati, B. L. Strand, G. Skjak-Braek, *Biomacromolecules*, **8**, 2809-2814 (2007).

[9] T. R. Bedson, P. D. Nellist, R. E. Palmer, J. P. Wilcoxon, *Microelectronic Engineering*, **53**, 187-190 (2000).

[10] A. Giguere, J. Beerens, B. Terreault, *Nanotechnology*, **17**, 600-606 (2006).

[11] T. Nagata, P. Ahmet, Y. Yamauchi, Y. Sakuma, T. Sekiguchi, T. Chikyow, *Nuclear Instruments and Methods in Physics Research B*, **242**, 250-252 (2006).

[12] R. Kometani, T. Morita, K. Watanabe, t. Hoshino, K. Kondo, H. Kanda, Y. Haruyama, T. Kaito, J. Fujita, M. Ishida, Y. Ochiai, S. Matsui, *Journal of Vacuum Science and Technology B*, **22**, 257-263 (2004).

[13] L. Pain, B. Icard, S. Manakli, J. todeschini, B. Minghetti, V. Wang, D. Henry, *Microelectronic Engineering*, **83**, 749-753 (2005).

[14] M. Srinivasarao, *Chemical Reviews*, **99**, 1835-1961 (1999).

[15] A. R. Parker, H. E. Townley, *Nature Nanotechnology*, **2**, 347-353 (2007).

[16] F. E. Round, R. M. Crawford, D. G. Mann, *The Diatoms: Biology & Morphology of the Genera*, Cambridge University Press, Cambridge, England (1990).

[17] Y. Wang, J. Lu, J. Mollet, M. R. Gretz, K. D. Hoagland, *Plant Physiology*, **113**, 1071-1080 (1997).

[18] J. C. Lewin, R. R. L. Guillard, *Annual Review of Microbiology*, 17, 373-414 (1963).

[19] M. Hildebrand, R. Wetherbee, *Progress in Molecular and Subcellular Biology*, Springer-Verlag, Berlin, Germany, 11-57 (2003).

[20] R. Bacsa, Y. Kihn, M. verelst, J. Dexpert, W. Bacsa, P. Serp, *Surface & Coatings Technology*, **201**, 9200-9204 (2007).

[21] E. Gyorgy, J. Santiso, A. Figueras, A. Giannoudakos, M. Kompitsas, I. N. Mihailescu, *Journal of Applied Physics*, **98**, 084302 (2005).

[22] C. Corbella, E. Bertran, M. C. Polo, E. Pascual, J. L. Andujar, *Diamond & Related Materials*, **16**, 1828-1834 (2007).

[23] D. Losic, G. Triani, P. J. Evans, A. Atanacio, J. G. Mitchell, N. H. Voelcker, *Journal of Materials Chemistry*, **16**, 4029-4034 (2006).

[24] A. Yang, Z. Cui, *Journal of Nanoparticle Research*, **9**, 245-250 (2007).

[25] M. R. Weatherspoon, S. M. Allan, E. Hunt, Y. Cai, K. H. Sandhage, *Chemical Communications*, 651-653 (2005).

[26] H. Natter, R. Hempelmann, *Electrochimica Acta*, **49**, 51-61 (2003).

[27] A. P. Philipse, M. P. B. van Bruggen, C. Pathmamanoharan, *Langmuir*, **10**, 92-99 (1994).

[28] L. M. Liz-Marzán, M. Giersig, P. Mulvaney, *Langmuir*, **12**, 4329-4335 (1996).

[29] N. Kawahashi, C. Persson, E. J. Matijević, *Journal of Materials Chemisty*, **1**, 577-582 (1991).

[30] N. Kawahashi, E. J. Matijević, Journal of Colloid Interface Science, **138**, 534-542 (1990).

[31] C. J. Brinker, G. W. Scherer, *Sol-gel science: The physics and chemistry of sol-gel processing*, Academic Press, San Diego (1990).

[32] R. A. Caruso, M. Antonietti, *Chemistry of Materials*, **13**, 3272-3282 (2001).

[33] I. Ichinose, H. Senzu, T. Kunitake, *Chemistry Letters*, 831-832 (1996).

[34] I. Ichinose, H. Senzu, T. Kunitake, *Chemistry of Materials*, **9**, 1296-1298 (1997).

[35] I. Ichinose, T. Kawakami, T. Kunitake, *Advanced Materials*, **10**, 535-539 (1998).

[36] J. Huang, I. Ichinose, T. Kunitake, A. Nakao, *Nano Letters*, **2**, 669-672 (2002).

[37] J. Huang, I. Ichinose, T. Kunitake, A. Nakao, *Langmuir*, **18**, 9048-9053 (2002).

[38] Y. Aoki, T. Kunitake, *Advanced Materials*, **16**, 118-122 (2004).

[39] Y. Aoki, T. Kunitake, A. Nakao, *Chemistry of Materials*, **17**, 450-458 (2005).

[40] S. Paul, J. Huang, I. Ichinose, *New Journal of Chemistry*, **29**, 1058-1063 (2005).

[41] T. Yonezawa, H. Matsune, T. Kunitake, *Chemistry of Materials*, **11**, 33-35 (1999).

[42] T. Kunitake, S. Lee, *Analytica Chimica Acta*, **504**, 1-6 (2004).

[43] L. Bao, S. M. Mahurin, S. Dai, *Analytical Chemistry*, **76**, 4531-4536 (2004).

[44] T. Ito, Y. Okayama, S. Shiratori, *Thin Solid Films*, **393**, 138-142 (2001).

[45] M. Fang, C. H. Kim, B. R. Martin, T. E. Mallouk, Journal of Nanoparticle Research, **1**, 43-49 (1999).

[46] S. Fujikawa, T. Kunitake, *International Journal of Nanoscience*, **1**, 617-620 (2002).

[47] S. Fujikawa, T. Kunitake, *Langmir*, **19**, 6545-6552 (2003).

[48] Y. Li, T. Kunitake, S. Fujikawa, *Colloids and Surfaces A*, **275**, 209-217 (2006).

[49] J. Huang, I. Ichinose, T. Kunitake, *Angewandte Chemie International Ed.*, **45**, 2883-286 (2006).

[50] Y. Li, T. Kunitake, S. Fujikawa, *Journal of Physical Chemistry B*, **110**, 13000-13004 (2006).

[51] J. Huang, T. Kunitake, *Journal of the American Chemical Society*, **125**, 11834-11835 (2003).

[52] J. Huang, T. Kunitake, S. Onoue, *Chemmical Communications*, 1008-1009 (2004).

[53] J. Huang, N. Matsunaga, K. Shimanoe, N. Yamazoe, T. Kunitake, *Chemistry of Materials*, **17**, 3513-3518 (2005).

[54] Y. Aoki, J. Huang, T. Kunitake, *Journal of Materials Chemistry*, **16**, 292-297 (2006).

[55] J. He, T. Kunitake, T. Watanabe, *Chemical Comunications*, 795-796 (2005).

[56] J. Huang, I. Ichinose, T. Kunitake, *Chemical Communications*, 1717-1719 (2005).

[57] S. Fujikawa, R. Takaki, T. Kunitake, *Langmuir*, **21**, 8899-8904 (2005).

[58] N. I. Kovtyukhova, E. V. Buzaneva, C. C. Waraksa, B. R. Martin, T. E. Mallouk, *Chemistry of Materials*, **12**, 383-389 (2000).

[59] W. Yan, B. Chen, S. M. Mahurin, E. W. Hagaman, S. Dai, S. H. Overbury, *Journal of Physical Chemistry B*, **108**, 2793-2796 (2004).

[60] D. Sun, Z. Liu, J. He, B. Han, J. Zhang, Y. Huang, *Microporous and Mesoporous Materials*, **80**, 165-171 (2005).

[61] J. Li, M. Kuwbara, *Science and Technology of Advanced Materials*, **4**, 143 (2003).

[62] J. Zeng, C. Lin, J. Li, K. Li, *Materials Letters*, **38**, 112 (1999).

[63] C. Eylem, G. Saghi-Szabo, B. H. Chen, B. Eichhorn, J. L. Peng, R.Greene, L. Salamanca-Riba, S. Nahm, *Chemistry of Materials*, **4**, 1038 (1992).

[64] D. Kolar, *Materials Research Society Symposium Proceedings*, **453**, 425 (1997).

[65] H. Kishi, N. Kohzu, K. Sugino, H. Ohsato, Y. Iguchi, T. Okuda, *Journal of the European Ceramic Society*, **19**, 1043 (1999).

[66] M. F. Yan, T. C. D. Huo, H. C. Ling, *Journal of the Electrochemical Society*, **134**, 493 (1987).

[67] K. Ohno, T. Abe, *Journal of the Electrochemical Society*, **141**, 1252 (1994).

[68] S. Sahni, S. B. Reddy, B. S. Murty, *Materials Science and Engineering A*, **452-453**, 758-762 (2007).

[69] X. Wang, M. Fujimaki, K. Awazu, *Optics Express*, **13**, 1486-1497 (2005).

[70] J. E. G. J. Wijnhoven, L. Bechger, *Chemistry of Materials*, **13**, 4486-4499 (2001).

[71] L. Gundlach, R. Ernstorfer, F. Willig, *Journal of Physical Chemistry C*, **111**, 13586-13594 (2007).

[72] J.-M. Wu, B. Qi, *Journal of the American Ceramic Society*, **90**, 657-660 (2007).

[73] H. Koyama, M. Fujimoto, T. Ohno, H. Suzuki, J. Tanaka, *Journal of the American Ceramic Society*, **89**, 3536-3540 (2006).

[74] J.-M. Wu, B. Huang, M. Wang, A. Osaka, *Journal of the American Ceramic Society*, **89**, 2660-2663 (2006).

[75] E. Mine, M. Hirose, M. Kubo, Y. Kobayashi, D. Nagao, M. Konno, *Journal of Sol-Gel Science and Technology*, **38**, 91-95 (2006).

[76] K. Fujita, J. Konishi, K. Nakanisi, K. Hirao, *Applied Physics Letters*, **85**, 5595-5597 (2004).

[77] O. Diwald, T. Thompson, T. Zubkov, Ed. G. Goralski, S. D. Walck, J. T. Yates, *Journal of Physical Chemistry B*, **108**, 6004-6008 (2004).

[78] J. S. King, C. W. Neff, D. L. Heineman, E. D. Graugnard, C. J. Summers, *Materials Research Society Symposium Proceedings*, **797**, 75-80 (2004).

[79] K. Awazu, M. Fujimaki, Y. Ohki, T. Komatsubara, *Materials Research Society Symposium Proceedings*, **797**, 69-74 (2004).

[80] T. A. Egerton, I. R. Tooley, *Journal of Physical Chemistry B*, **108**, 5066-5072 (2004).

[81] X. Jiang, T. Herricks, Y. Xia, *Advanced Materials*, **15**, 1205-1209 (2003).

[82] J. E. G. J. Wijnhoven, L. Bechger, W. L. Vos, *Chemistry of Materials*, **13**, 4486-4499 (2001).

[83] V. N. Manoharan, A. Imhof, J. D. Thorne, D. J. Pine, *Advanced Materials*, **13**, 447-450 (2001).

[84] T. Sekiya, M. Igarashi, S. Kurita, S. Takekawa, M. Fujisawa, *Journal of Electron Spectroscopy and Related Phenomena*, **92**, 247-250 (1998).

[85] A. N. Shultz, W. Jang, W. M. Hetherington III, D. R. Baer, L.-Q. Wang, M. H. Engelhard, *Surface Science*, **339**, 114-124 (1995).

[86] G. Sberveglieri, S. Groppelli, P. Nelli, *Sensors and Actuators B*, **4**, 457-461 (1991).

[87] A. T.-Silver, A. S-Juárez, *Materials Science and Engineering B*, **110**, 268-271 (2004).

[88] T. Hyodo, K.Sasahara, Y. Shimizu, M. Egashira, *Sensors and Actuators B*, **106**, 580-590 (2005).

[89] Y. Shimizu, N. Nakashima, T. Hyodo, M. Egashira, *Journal of Electroceramics*, **6**, 209-217 (2001).

[90] M. Law, H. King, B. Messer, F. Kim, P. Yang, *Angewandte Chemie International Ed.*, **41**, 2405-2408 (2002).

[91] I. Sayago, J. Gutiérrez, L. Arés, J. I. Robla, M. C. Horrillo, J. Getino, J. Rino, J. A. Agapito, *Sensors and Actuators B*, **26-27**, 19-23 (1995).

[92] K-N. P. Kumar, K. Keizer, A. J. Burggraaf, T. Okubo, H. Nagamoto, *Journal of Materials Chemistry*, **3**, 923-929 (1993).

[93] K-N. P. Kumar, K. Keizer, A. J. Burggraaf, *Journal of Materials Science Letters*, **13**, 59-61 (1994).

[94] P. K. Nair, F. Mizukai, J. Nair, M. Salou, Y. Oosawa, H. Izutsu, K. Maeda, T. Okubo, *Materials Research Bulletin*, **33**, 1495-1502 (1998).

[95] J. Livage, M. Henry, C. Sanchez, *Progress in Solid State Chemistry*, **18**, 259 (1998).

[96] R. Roy, Science, **238**, 1664 (1987).

[97] E. J. A. Pope, J. D. Mackenzi, *Journal of Non-Crystalline Solids*, **87**, 185 (1986).

[98] H. Schmidt, H. Scholze, A. Kaiser, *Journal of Non-Crystalline Solids*, **63**, 1 (1984).

[99] C. J. Brinker, K. D. Keefer, d. W. Schaefer, R. A. Assink, B. D. Kay, C. S. Ashley, *Journal of Non-Crystalline Solids*, **63**, 45 (1984).

CHAPTER 2: EXPERIMENTAL APPARATI AND CHARACTERIZATION METHODS

2.1 Introduction

For this thesis, two different methods were utilized for applying functional metal-oxide coatings to biological and lithographically patterned substrates. Both methods are based on sol-gel processing. The first method, which was utilized at the beginning of this thesis research, incorporated a refluxing/evaporation coating technique where mesoporous powders (diatom frustules) were charged directly into the sol-gel based solution. Continuous metal-oxide coatings with varied thickness were obtained on the frustule substrates following a series of refluxing and evaporation steps. At times, the coatings were difficult to reproduce due to uncontrolled factors, such as fluctuations of the relative humidity in the air (a seasonal problem in Atlanta, GA) which led to premature precipitation due to reaction of moisture with the metal alkoxide precursors.

The second coating method employed in this thesis yielded major improvements upon both problems encountered (i.e., uncontrolled coating thicknesses and premature precipitation of the alkoxide precursors) using the reflux/evaporation coating technique. After searching the literature and reading Kunitake's papers on the surface sol-gel process, it became readily apparent that this layer-by-layer coating process could also be employed to apply metal-oxide coatings on diatom frustules (and other hydroxylated scaffold surfaces) to achieve coatings with desired thicknesses. The literature is already rich with examples demonstrating linear uniform film growth per surface sol-gel adsorption cycle for many alkoxide precursors (e.g., $Ti(O\text{-}nBu)_4$, $Al(O\text{-}nBu)_3$, $Zr(O\text{-}nPr)_4$, $Nb(O\text{-}nBu)_5$, $Si(O\text{-}Me)_4$, $B(OEt)_3$ [1, 2]) which proves the validity and versatility of this

process. However, prior published work utilizing the surface sol-gel process has been performed under uncontrolled atmospheric conditions. As a result, the alkoxide solutions absorbed moisture from the air and formed oligomers in the alkoxide stock solutions [1]. The oligomers can also adsorb on hydrolyzed surfaces and thereby disrupt the expected uniform film growth behavior per adsorption cycle of the surface sol-gel process. This thesis addresses the problem of uncontrolled precipitation and polymerization of the alkoxide solutions during surface sol-gel processing by performing the reactions inside a controlled atmosphere (dry nitrogen) glove box.

Prior surface sol-gel processing has also been performed by hand dipping substrates into solutions or by manually adding solutions to a vacuum filtration unit. Such processing techniques are cumbersome and time consuming, especially if the coating protocol involves multiple (10 or more) adsorption cycles. This thesis also addresses this problem through the development of a custom-built automated pumping system for performing the surface sol-gel process (inside the controlled atmosphere glove box). This automated coating system increases experimental reproducibility, reduces the likelihood of human error, and frees up valuable manpower. Such improvements to the surface sol-gel process make this process a more viable and lower cost alternative to other layer-by-layer (e.g., atomic layer deposition (ALD)) techniques.

2.2 Experimental Setup for the Reflux/Evaporation Sol-Gel Coating Process

Typical experiments employing the reflux/evaporation coating technique in this thesis utilized a common chemical distillation experimental setup. A modified Barnstead International electrothermal heating and stirring mantle (Figure 2.1(a)) was used to

uniformly heat the sol-gel solutions. The factory-supplied analog heating control of the mantle was replaced with an Omega CN820 digital temperature controller to allow better precision over changing the applied temperature of the mantle. The temperature was relayed to the Omega controller using a type K thermocouple situated at the bottom of the mantle as shown in Figure 2.1(b). A round bottom flask containing the sol-gel precursor solution and diatom frustules along with a magnetic stir bar was centered directly over the thermocouple. Kalonite wool was packed around the upper surface of the flask to help maintain the heat inside the reaction vessel. The solution temperature was monitored with a thermocouple and was found to be plus or minus 3% upon equilibration of the set point temperature of the CN820 controller.

As discussed earlier in Section 1.3.1, the hydrolysis and condensation reactions in sol-gel processing can be activated by increasing the solution temperature. However, alkoxide precursors tend to consist of volatile alcohol-based solutions with boiling points around 80-90^{o}C. Thus, in order to prevent the uncontrolled evaporation of the volatile solvent, the solutions were refluxed by attaching a Liebig condenser to the round bottom flask as shown in Figure 2.1(c). Typical coating experiments usually employed three refluxing steps for time periods ranging from 1 to 3 hours.

Controlled evaporation of the solvent was achieved by lowering the temperature of the solution and adding a Liebig condenser (which is connected to a second round bottom flask) to the refluxing arrangement shown in Figure 2.1(c). The evaporation step in the sol-gel process enhanced the condensation reaction through elimination of the water or alcohol molecules generated during the condensation reaction. It has been reported that slow evaporation of the volatile solvent can lead to coatings that are less

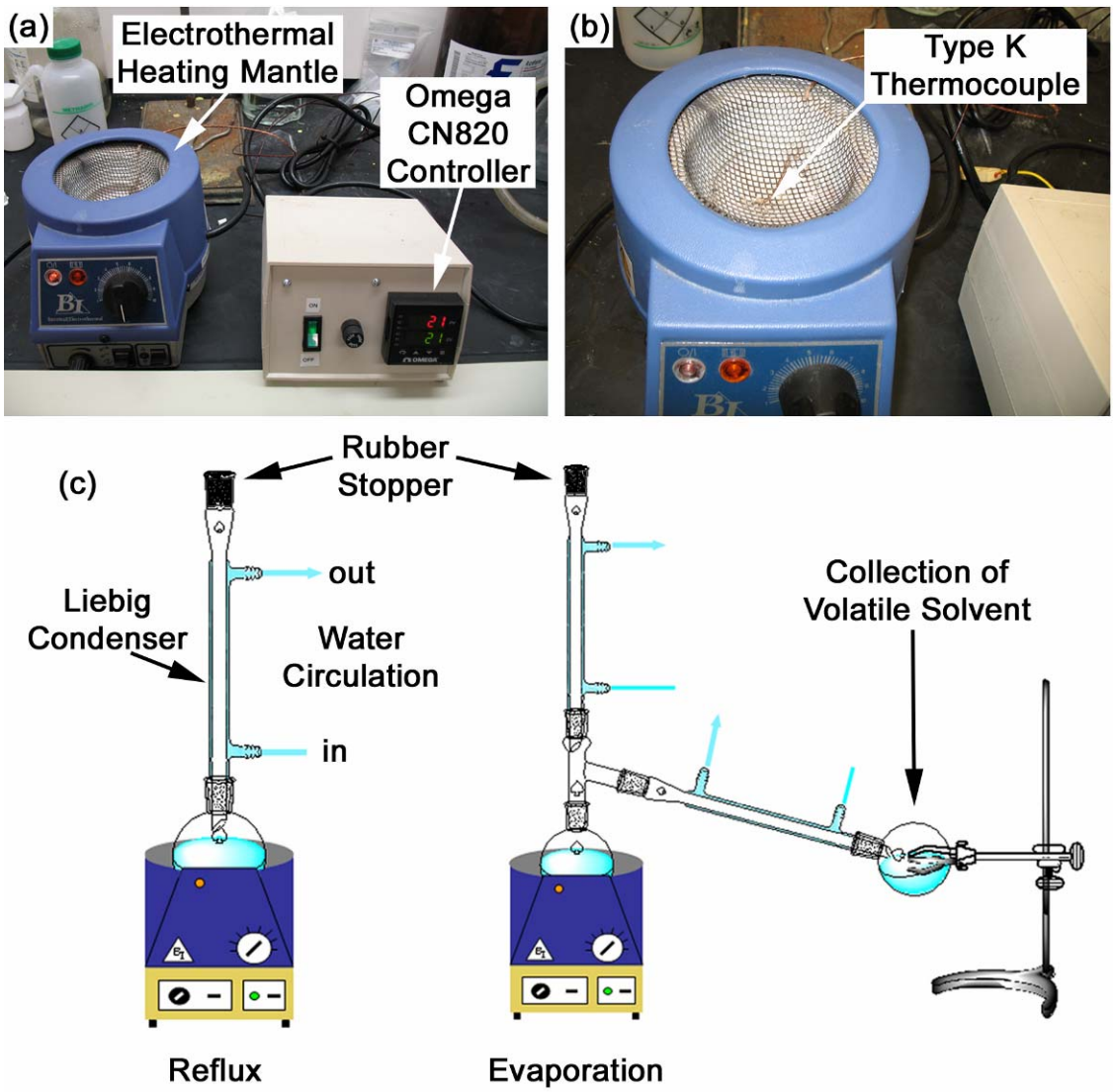

Figure 2.1: Experimental setup for the coating processes utilizing heat activated sol-gel processing. The factory-supplied analog heating controller of a Barnstead International electrothermal heating mantle was replaced with an Omega CN820 digital temperature controller (a) to more readily control the applied temperature of the mantle using a type K thermocouple situated at the bottom of the mantle (b). Refluxing and evaporation iterations in this coating process utilized a round bottom flask (containing the precursor and powder samples) and Liebig condenser columns (c).

mud-cracked than for cases where the evaporation proceeds rapidly [3, 4].

The distinct advantage of utilizing this reflux/evaporation coating technique is that less reactive precursors can be thermally activated, for enhanced reaction rates. By modifying the temperature controller on the electrothermal heating mantle, the temperature for both refluxing and evaporation steps could be precisely controlled. Also, the solution could be magnetically stirred to allow for continuous exposure of the solution to all template surfaces.

The disadvantage of this process is that it is not well suited for applying uniform coatings to flat (wafer) substrates and to delicate biologically-derived surfaces, such as butterfly wings. This process also requires manual exchange of the glassware configuration between the reflux and evaporation steps, and manual changing of the temperature of the controller. Also, of considerable note, the alkoxide precursor tended to condense on all available surfaces (including the round bottom flask) during the evaporation step. Upon retrieving the samples from the flask using a spatula, the alkoxide that condensed on the glass surface became mixed with the coated templates. Such incorporation of residual alkoxide resulted in nodule formation on the surface of the template samples.

2.3 Custom-Built Automated Pumping System for Surface Sol-gel Processing

An automated pumping system was custom-built for controllably and reproducibly coating hydroxylated surfaces in a layer-by-layer manner using the surface sol-gel process. This custom-designed system utilized computer-control to manipulate fluids during the surface sol-gel process. The idea behind the development of this system was to eliminate time consuming and mundane manual tasks (such as dipping substrates

into solutions or pouring solutions into vacuum filtration units) associated with the serial surface sol-gel process. The simple design of this automated pumping system is illustrated in Figure 2.2.

The vacuum filtration unit (pictured in Figure 2.2) was a critical design component of this system because it housed the substrate to be coated and contained the solution required for the hydrolysis and condensation reactions. The pore size of the filter material needed to be small enough to eliminate the passage of the solution for desired periods of reaction time. A fritted glass filter possessing pore sizes < 4 – 8 μm met this requirement. Such fritted glass filters require vacuum suction in order for the solution to pass through the pores. Vacuum filtration units of various sizes which contained fritted glass filters with the desired pore sizes were obtained from Ace Glass (Vineland, NJ).

The addition of the solutions to the vacuum filtration unit was accomplished using peristaltic pumps controlled by a computer. The volume of the solution added to the filtration unit was simply controlled by the time during which the peristaltic pump was allowed to run, which made this process extremely versatile for accommodating substrates requiring larger or smaller volumes. A more detailed explanation of the engineering design and fabrication details of the automated pumping system is presented below.

The automated surface sol-gel pumping system was housed within a controlled atmosphere (dry nitrogen) glove box to prevent the premature hydrolysis and subsequent polymerization of the moisture sensitive alkoxide precursors used in this thesis for

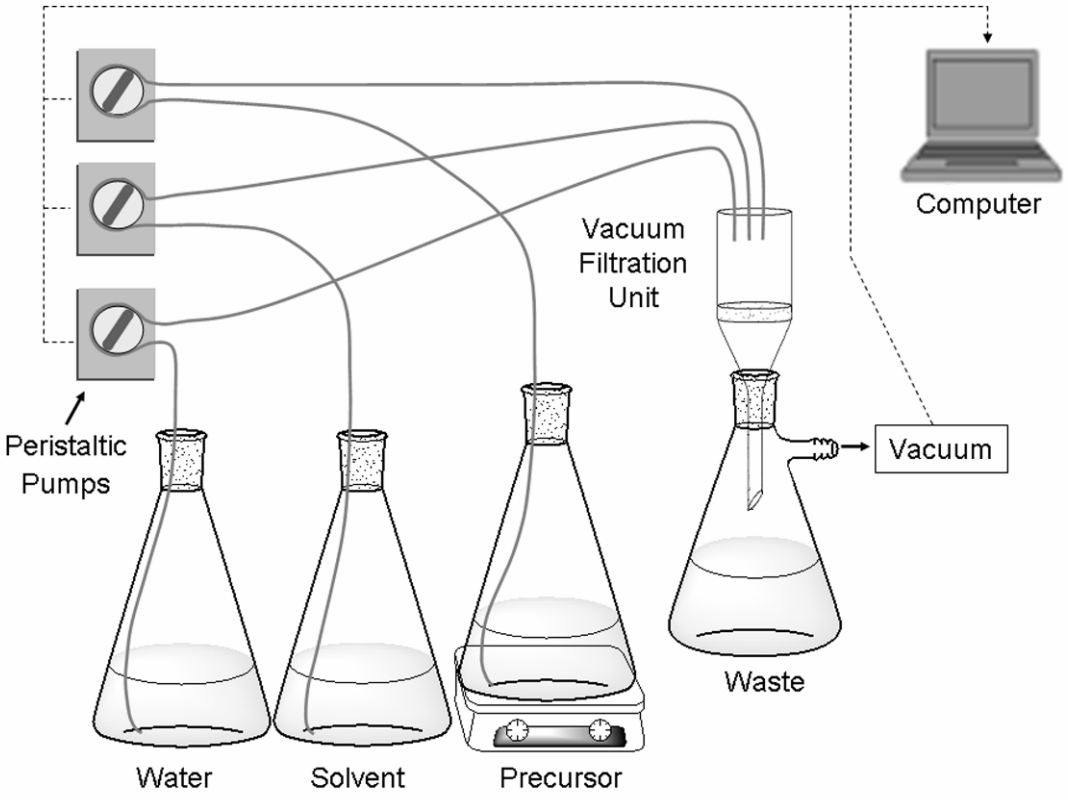

Figure 2.2: Schematic illustration of the automated pumping system utilized for controllably and reproducibly coating hydroxylated surfaces with functional metal-oxide coatings derived from alkoxide precursors. The system employed a vacuum filtration unit which supported the structures to be coated (wafers or powder) and was the location where the hydrolysis and condensation reactions occurred in the surface sol-gel process. The peristaltic pumps and vacuum pump were all computer controlled.

applying thin metal-oxide coatings on hydroxylated surfaces. Performing the surface sol-gel reactions inside of the glove box provided an element of control which was lacking in the previous surface sol-gel demonstrations reported in the literature. Not only did the dry atmosphere of the glove box provide stability against premature polymerization of the surface sol-gel stock solutions (resulting in uncontrolled film growth), but it also provided a suitable facility for long term storage of the moisture-sensitive alkoxide precursors.

The glove box used to house the automated surface sol-gel pumping system was custom built (Figure 2.3(b)). This glove box was equipped with a photohelic controller attached to two solenoid valves for regulation of the pressure inside of the glove box. One of the solenoid valves was attached to a vacuum pump and the other was attached to the in-house nitrogen system supplied in the MS&E building at the Georgia Institute of Technology. The nitrogen which entered the glove box passed through a Drierite™ Ascarite desiccator column, shown in Figure 2.3(a), to absorb moisture from the inert gas before it entered the glove box (Note: the maximum operable pressure for the nitrogen gas entering the solenoid valve was 30 psi which was adjusted by the pressure regulator pictured in Figure 2.3(a)). The glove box was equipped with a Vacuum Atmospheres HE-493 DRI-TRAIN system which circulated the gas inside of the glove box past a heated copper media column to maintain a dry atmosphere. The humidity inside of the glove box was monitored using an Omega RH32 relative humidity sensor.

LabView 8.0 software was used to control the various pumps of the system. The LED (light emitting diode) buttons of the LabView program (Figure 2.3(c)) were programmed to interface with the digital outputs of a National Instruments USB-6008

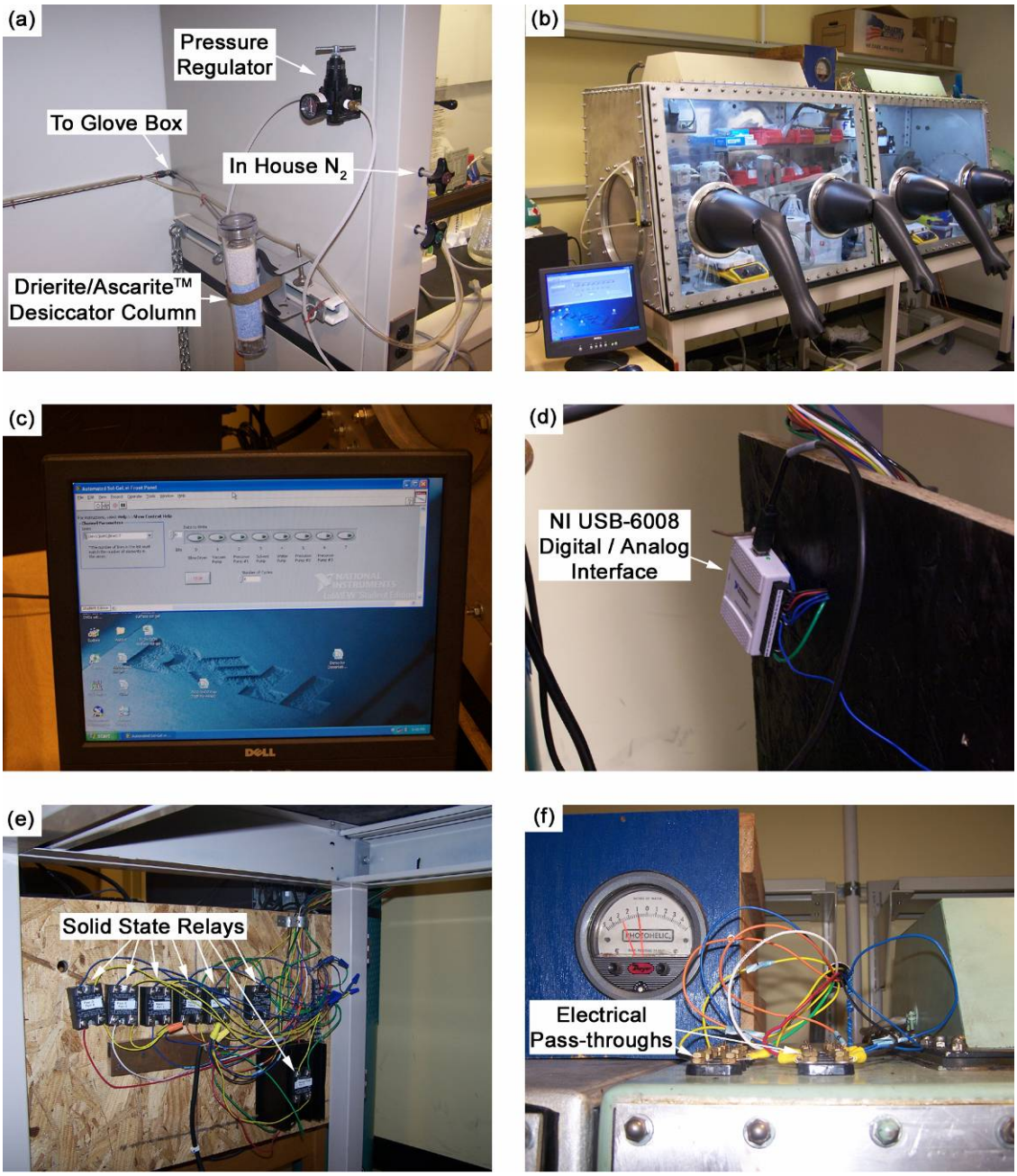

Figure 2.3: Photographs showing the engineering details of the automated surface sol-gel pumping system housed inside of a controlled atmosphere dry nitrogen glove box. The in-house nitrogen first passed through a Drierite/Ascerite™ desiccator column (a) and into the glove box (b) through a pressure-controlled electric solenoid valve. LabView 8.0 software (c) was used as the control software which interfaced with a NI USB-6008 DAQ module (d) which supplied an electric signal to open and close the solid state relays (e) which allow current/voltage to flow from the wall outlet (120 V) into the glove box through electrical pass-throughs situated on the top of the glove box (f). Further details are continued on the next page.

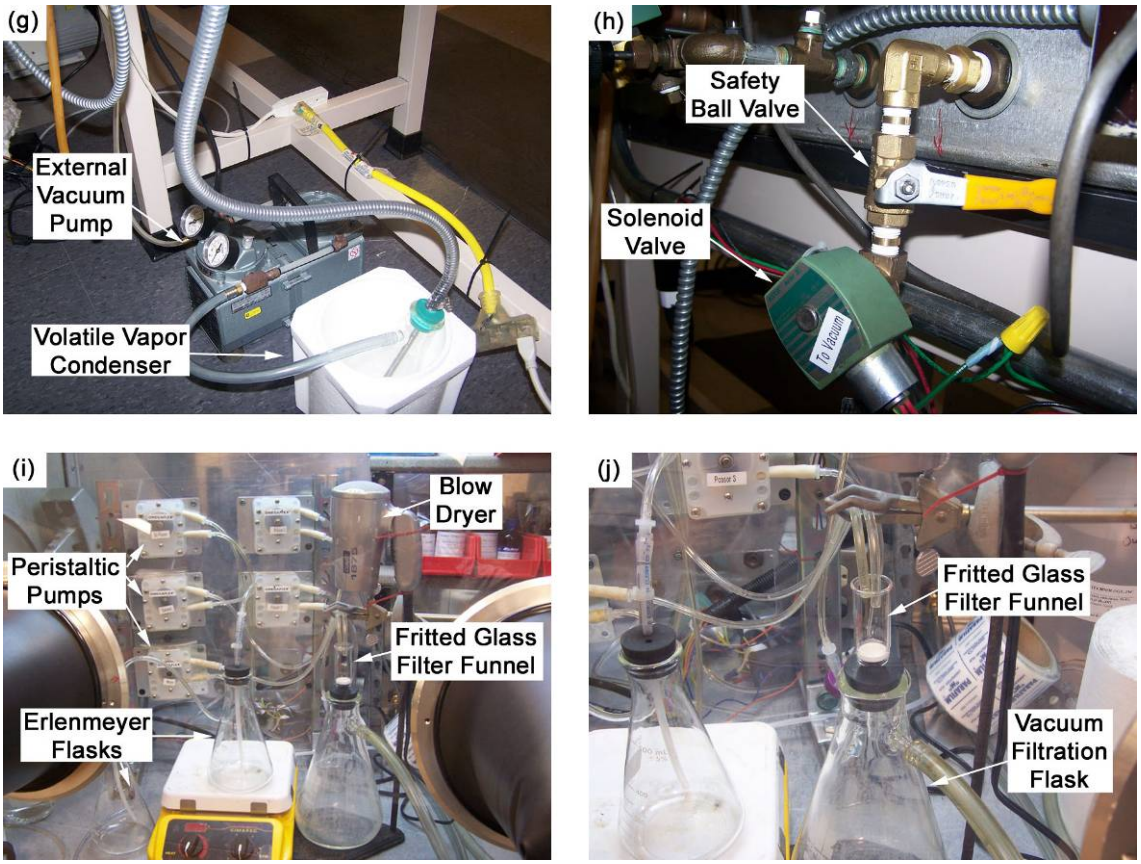

Figure 2.3 continued: Photographs showing the processes which were controlled using LabView. The external vacuum pump (g) (used for evacuating the solutions in the fritted glass filter funnel) was connected to a vacuum filtration flask in (j) through a solenoid valve (h) to help prevent external air from entering into the glove box. Both the vacuum pump and solenoid valve were controlled with a single solid-state relay (i.e., when the pump turned on or off, the solenoid valve opened or closed, respectively). Five internal peristaltic pumps (i) (used for controllably pumping the solutions into the fritted glass filter funnel) and a blow dryer (i) (used for drying the samples) were also controlled using LabView.

data acquisition (DAQ) module (Figure 2.3(d)) equipped with 8 analog inputs, 2 analog outputs, 12 digital input/outputs, and an onboard +5V output (200 mA maximum) power supply. The digital output channels of the DAQ were wired to several solid-state relays (3-30 VAC/DC, obtained from McMaster Car, Atlanta, GA) (Figure 2.3(e)).

When one of the LED buttons of the LabView program was depressed (illuminated by clicking on it with the left mouse button), a 3V signal was sent from the DAQ to the corresponding solid-state relay which energized the relay and closed the electrical circuit allowing the voltage from the wall outlet (120 V) to pass through the relay. The voltage/current was then passed into the glove box through electrical pass-throughs located on the top of the glove box (Figure 2.3(f)). Current continued to flow, and the corresponding pumps (pictured in Figures 2.3(g and i)) continued to run, as long as the LED button of the LabView program was depressed.

A minor set back in the electrical design of this system was encountered when the pumps were actually wired to the relays. The relays required a minimum of 3V to close the relay and the DAQ would supply a maximum of 3.5V. However, the input impedance of the relays was too low and therefore required a lifting current from an additional source. The additional current was supplied by wiring the onboard 5 V power supply in series with a 4 kΩ resistor to each of the output terminals (Figure 2.4). This electrical configuration supplied the additional current from the DAQ to energize and close the solid-state relays when the LED button of the LabView program was depressed.

Although the LabView program pictured in Figure 2.3(c) seemed straight forward and easy to use (i.e., mouse clicking on the LED buttons simply turned a process on or off), manual control of the order and timing of the pumps was required. Thus, another

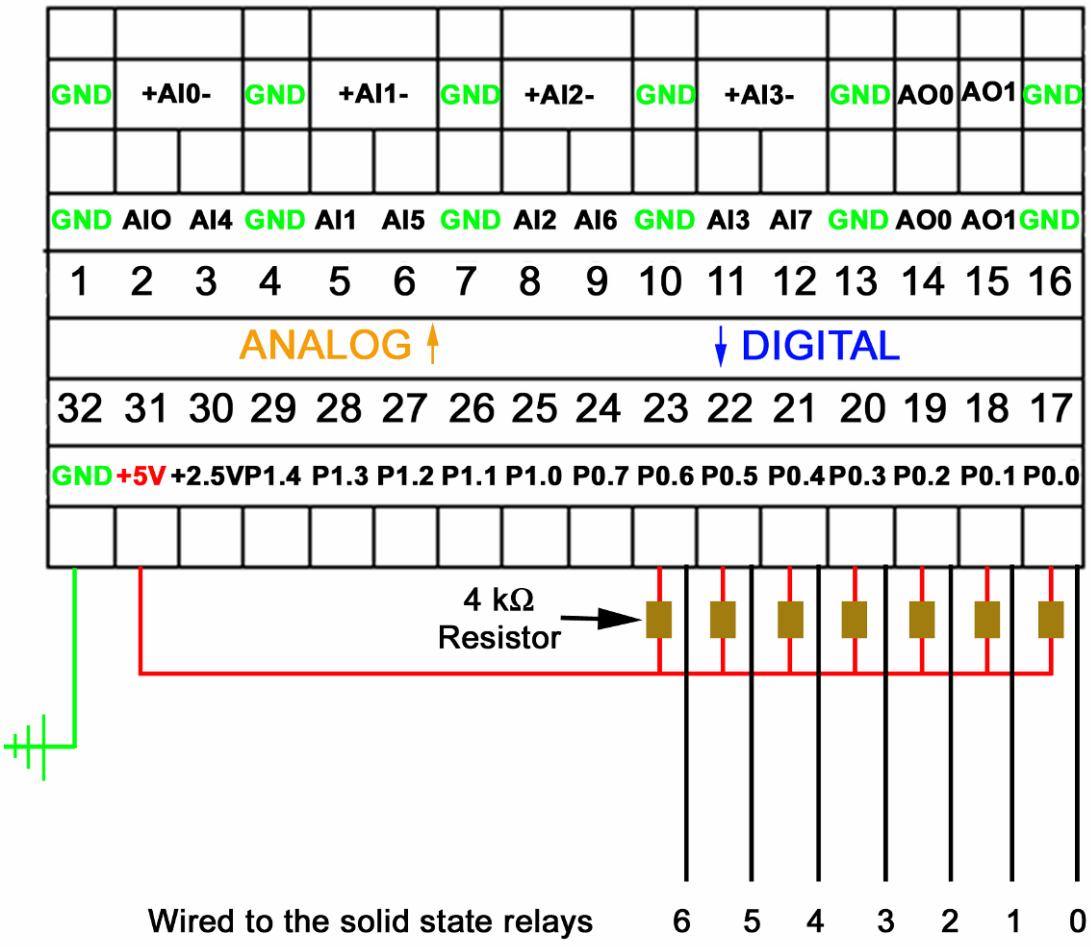

Figure 2.4: The electrical wiring diagram of the NI USB-6008 DAQ showing the electrical wiring configuration which supplied the additional lifting current necessary for controlling the solid state relays using the onboard 5V power supply and a 4 kΩ resistor. The following pumps/valves were wired to the solid state relays which were wired to the following DAQ channels: (0) blow dryer, (1) external vacuum pump and solenoid valve, (2) precursor pump 1, (3) solvent pump, (4) water pump, (5) precursor pump 2, and (6) precursor pump 3.

program called AutoIt v3 was used to automate the mouse clicks to depress the LED buttons to turn the pumps on and off. AutoIt is a freeware program (downloadable off of the internet) which uses a BASIC-like scripting language to automate general Windows-based tasks, such as simulating keystrokes and mouse movements. One of the benefits of using this program to control the automated process was that the scripts used to run any experiment could be saved for later reference. This benefit provided a method for identifying and reproducing an experiment under the exact same reaction conditions. Appendix A provides a sample AutoIt program and a detailed explanation of the use of this program for controlling the system.

One of the critical design issues for maintaining a dry atmosphere inside of the glove box (and also for freeing up limited space) was to situate the vacuum pump on the outside of the glove box, as shown in Figure 2.3(g). Operation of the pump inside of the glove box would result in wet vapor being exhausted directly into the glove box. In order to evacuate the solutions from the fritted glass filter funnel, the external vacuum pump (Figure 2.3(g)) was connected to the vacuum filtration flask (Figure 2.3(j)) via a solenoid valve-controlled pass-through (Figure 2.3(h)). The solenoid valve connected the vacuum filtration flask to the external vacuum pump with a vacuum hose which first led to an ice-cooled volatile vapor condenser, pictured in Figure 2.3(g). The solenoid valve and the vacuum pump were operated by the same solid-state relay, so that the solenoid valve opened and closed when the vacuum pump turned on and off, respectively. A hose leading to an evacuable hood was connected to the external vacuum pump so that the alcohol vapors were not pumped directly into the lab atmosphere. Also, rubber stoppers containing a plastic tube were used to cork the Erlenmeyer flasks (Figure 2.3 (i and j))

containing the precursor, solvent, and water solutions to prevent these solutions from vaporizing into the glove box over the course of an experimental run.

A typical reaction protocol for the surface-sol gel experiments consisted of situating the hydroxyl-terminated template (diatom frustules, lithographically-derived photonic crystals, or butterfly wings) inside of the fritted glass filter funnel. The alkoxide precursor was then pumped into the funnel to completely submerge the substrate. After the precursor was allowed to react with the surface hydroxyl groups of the substrate (usually around 5-10 min), the solution was then evacuated by vacuum filtration for 18 seconds. Solvent was then immediately pumped into the funnel (still under vacuum) to rinse away any of the physisorbed alkoxide using four rinsing cycles of 8 second durations. Water was then pumped into the funnel to reactivate surface hydroxyls on the preceding chemisorbed alkoxide layer. The hydroxyl reactivation step usually lasted for 1 min and was followed by vacuum filtration for 8 seconds. Solvent was again pumped into the funnel (under vacuum) to help rinse away any remaining water molecules using four rinsing cycles of 8 second durations. The blow dryer, pictured in Figure 2.3(j), was then turned on while the vacuum pump was still running to help speed up the drying process by aspirating hot air past the samples for 3-5 minutes before the alkoxide precursor was again pumped into the funnel.

2.4 Typically Used Characterization Methods

The morphologies of the diatom frustules, lithographically-patterned photonic crystals, and butterfly scales were evaluated with a field emission scanning electron microscope (1530 SEM, LEO/Zeiss Electron Microsopy, Gmbh, Thornwood, NY) equipped with energy-dispersive X-ray analysis capability.

The crystal structures of the converted templates were evaluated at room temperature using X-ray diffraction (XRD) analyses (Alpha-1, PANalytical Corp., Almelo, the Netherlands). High temperature X-ray diffraction (HTXRD) analyses performed on the Eu-doped $BaTiO_3$ precursor coatings applied to MgO diatom frustules, and the tin oxide doped titania gels, were performed using an X-pert Pro MPD diffractometer (PANalytical Corp., Almelo, the Netherlands) equipped with a platinum strip heater (HTK2000 furnace, Anton-Paar, Gmbh, Graz, Austria). The diffractometer used a vertical theta-theta goniometer, 0.5^o divergence slits, and a solid-state detector (Xcelerator, PANalytical). The temperature of the heating strip was calibrated using standard reference materials (SRM 759, NIST, Gaithersburg, MD). HTXRD analyses were performed with the help of Dr. Michael S. Haluska (Georgia Institute of Technology).

Transmission electron microscopy and electron diffraction was performed by Dr. Ye Cai (Georgia Institute of Technology). The analyses were conducted using a JEOL 4000 EX instrument (Japan Electron Optics Laboratory, Tachikawa, Tokyo) to evaluate the structure and phase content of the coatings applied on the biological and lithographically patterned templates.

All other characterization techniques are described within the chapters in which they were utilized.

2.5 References

[1] I. Ichinose, H. Senzu, T. Kunitake, *Chemistry Letters*, 831-832 (1996).

[2] I. Ichinose, H. Senzu, T. Kunitake, *Chemistry of Materials*, **9**, 1296-1298 (1997).

[3] C. Garzella, E. Comini, E. Tempesti, C. Irigeri, G. Sbervaglieri, *Sensors and Actuators B*, **68**, 189-196 (2000).

[4] M. Veith, S. Mathur, A. Kareiva, M. Jilavi, M. Zimmer, V. Huch, *Journal of Materials Chemistry*, **9**, 3069-3079 (1999).

CHAPTER 3: COATING PHYTOPLANKTON WITH PHOTOLUMINESCENT PEROVSKITE

The research presented in this chapter has been reported in the following publications:

i) M. R. Weatherspoon, S. M. Allan, E. Hunt, Y. Cai, K. H. Sandhage, *Chem. Commun.*, **5**, 651-653, (2005).

ii) M. R. Weatherspoon, M. S. Haluska, Y. Cai, J. S. King, C. J. Summers, R. L. Snyder, K. H. Sandhage, *J. Electrochem. Soc.*, **153**, H34-H37 (2006).

iii) M. R. Weatherspoon, S. M. Allan, C. S. Gaddis, Y. Cai, M. S. Haluska, R. L. Snyder, K. H. Sandhage, *Mater. Res. Soc. Sypm. Proc.*, **873E**, K1.8.1-K1.8.6, (2005).

3.1 Introduction

In this Chapter, the fabrication of perovskite $BaTiO_3$ microparticles with controlled 3-D morphologies, using phytoplankton (diatom) frustules as templates, is demonstrated. Considerable research has been devoted to produce microparticles possessing controlled shapes for phosphor powder-based applications. The properties of powder-based phosphors (e.g., brightness, uniformity, resolution, efficiency, stability) depend upon the morphologies and size distributions of the powder [1-7]. Phosphors with controlled morphologies and size distributions can exhibit enhanced resolution and brightness through higher packing densities which can lead to a more uniform light intensity distribution for optical displays [8-10]. Optimal phosphor size distributions lie between 1-8 μm [5, 7, 11]. Conventional processing methods are not capable of yielding chemically-tailored phosphor microparticles in this size range with precisely-controlled 3-D morphologies. The general practice of producing micron-sized phosphor particles

usually employs a milling step after the reaction synthesis is completed which causes undesirable defects and degradation in the brightness of the phosphor powders [11, 12].

The silicified skeletons of diatoms (frustules) could be utilized as templates for producing phosphor powders with precisely-controlled shapes and sizes. Maximum frustule dimensions for various diatom species range from <1 to >10^2 μm [13, 14]. Thus, it is possible to select a specific diatom species (possessing size dimensions which lie within the optimal phosphor particle size of 1 – 8 μm) that, upon sustained reproduction, would provide billions or more templates of identical shape and size. Conversion of such structures into controlled shape/size phosphor materials could enhance the packing density of coatings and lead to increased brightness and resolution of devices.

Aulacoseira diatom frustules were coated with europium-doped barium titanate (Eu-doped $BaTiO_3$) as a proof of principle, because these frustules could readily be obtained in the form of diatomaceous earth (DE) from a local hardware store. $BaTiO_3$ was selected as the host lattice because it is a wide band gap semiconductor (3.2 eV) possessing the perovskite crystal structure which offers a large spectral range overwhich a rare earth dopant may emit light [15]. $BaTiO_3$ also possesses a relatively high solid solubility for a variety of rare earth activator cations (e.g., Ce, Nd, Sm, Eu, Gd, Dy, Ho, Er) [15-18]. Europium was chosen as a luminescent activator due to the significant level of doping (up to 8 mol %) reported for Eu cations in $BaTiO_3$ prior to the onset of concentration quenching of photoluminescence [15].

One of the challenges faced in this research is chemical incompatibility of the silica-based chemistry of the *Aulacoseira* diatom frustules with $BaTiO_3$. This challenge was overcome by first converting the silica (SiO_2) frustules into magnesia (MgO), which

is chemically compatible with $BaTiO_3$. The conversion of the SiO_2-based frustules into MgO was accomplished using a gas/solid displacement reaction which preserved the microscale shape and nanoscale features of the original frustules. $BaTiO_3$ coatings were then applied to the MgO-bearing frustules using the refluxing/evaporation technique described in Section 2.2. This coating technique was utilized owing to the ease in which the dopant could be dissolved into the alkoxide solution and for the added benefit of solution temperature control (Note: the surface sol-gel system was not built at this time). The Eu^{3+}-doped $BaTiO_3$-bearing frustules exhibited bright red emission upon stimulation with a 337 nm (UV) light source. This work demonstrated that microparticles with well-controlled 3D morphologies and non-natural multicomponent ceramic compositions can be produced by merging the self-assembly ability of biomineralizing micro-organisms with synthetic chemical tailoring.

3.2 Experimental Procedure

3.2.1 Materials

The barium titanium ethylhexano isopropoxide ($BaTi(OOC8H_{15})(OC_3H_7)_5$ 99.5%), anhydrous ethanol (94-96%), europium (III) nitrate (99.9%), sodium hydroxide pellets (98%), and magnesium flakes (99.8%) were all purchased from Alfa Aesar Chemical Co. (Ward Hill, MA). The 1020-iron tubing (2.5 cm in dia.) was purchased from TW Metals (Atlanta, GA).

3.2.2 Conversion of the Silica-Based Frustules into Magnesia/Silicon Composites

The chemical conversion of the silica diatom frustules was accomplished inside sealed steel reaction tubes (20 cm long by 2.5 cm in dia.) shown schematically in Figure

3.1(a). One end of the tube was crimped and TIG welded shut. Magnesium flakes were then added to this end of the tube and a slight crimp was placed 8 cm from the welded end of the tube to prevent mixing of the reactants. The silica diatom frustules (Figure 3.1(b)) were thinly spread inside of a custom built steel boat (constructed from metal foil 8 cm long by 2 cm wide) and placed at the opposite end of the steel tube. This end of the tube was then crimped and welded shut in air. The as-prepared reaction vessels were then thrust into the hot zone of the furnace to allow for magnesium vaporization and reaction with the silica frustules.

3.2.3 Photoluminescence Characterization

Photoluminescence measurements were conducted courtesy of Jeff King (Georgia Institute of Technology) at room temperature using 337 nm (UV) excitation from an externally triggered (Chopper Sync II, Spiricon, Inc., Logan, UT), pulsed N_2 laser (LN1000, Laser Photonics, Orlando, FL). The specimens were excited at 45^o incidence and the emission was collected at normal incidence (as shown in Figure 3.2) using a collimating lens (74-UV, Ocean Optic, Inc., Dunedin, FL) and a fiber probe (LG-455-020-3, Acton Research Corp., Acton, MA). The fiber probe was coupled to an emission monochromator (Spectra Pro 500i, Acton Research Corp.) affixed with a thermoelectrically cooled photo sensor module (H7422-50, Hammamatsu Co., Bridgewater, NJ).

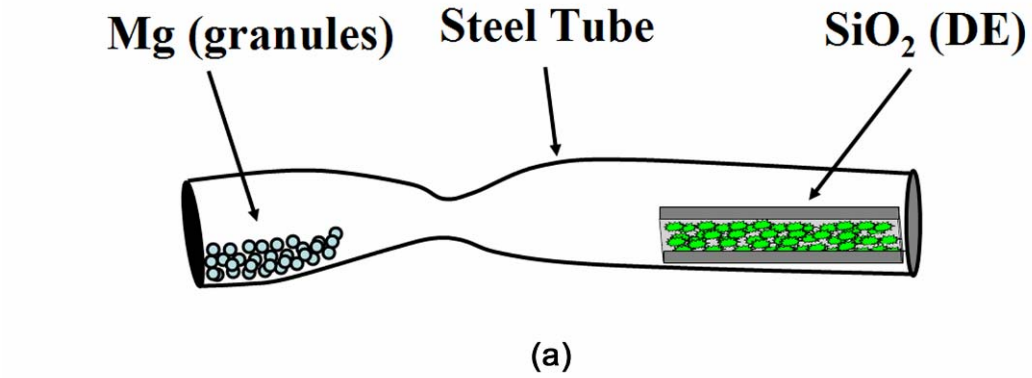

(a)

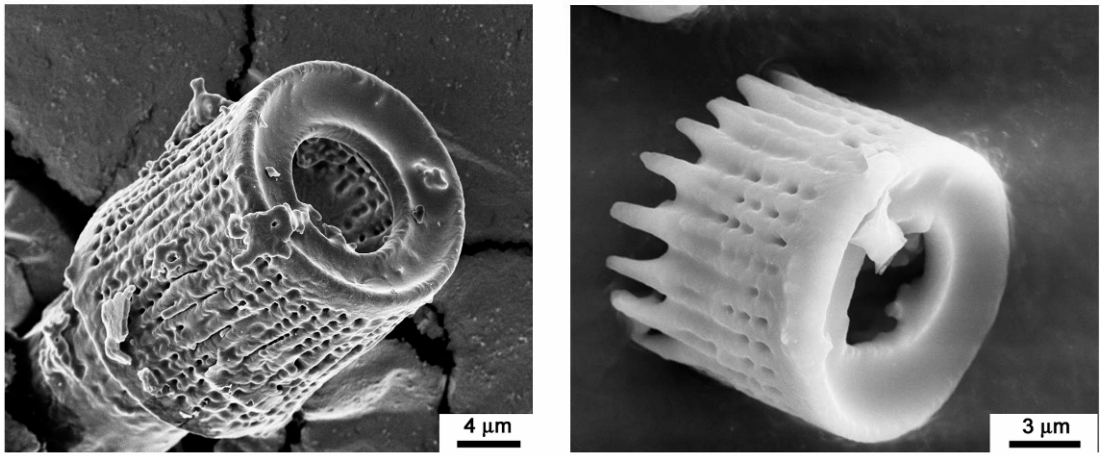

(b)

Figure 3.1: Schematic illustration of the mild steel reaction vessel (a) which was utilized to convert SiO_2 diatomaceous earth (DE) (b) into MgO/Si composites at 900^{o}C. Each end of the tube was welded shut to contain the Mg reactant gas. *Aulacoseira* diatom frustules (shown in b) possessed a cylindrical shape with rows of fine pores and intercalating fingerlike extensions.

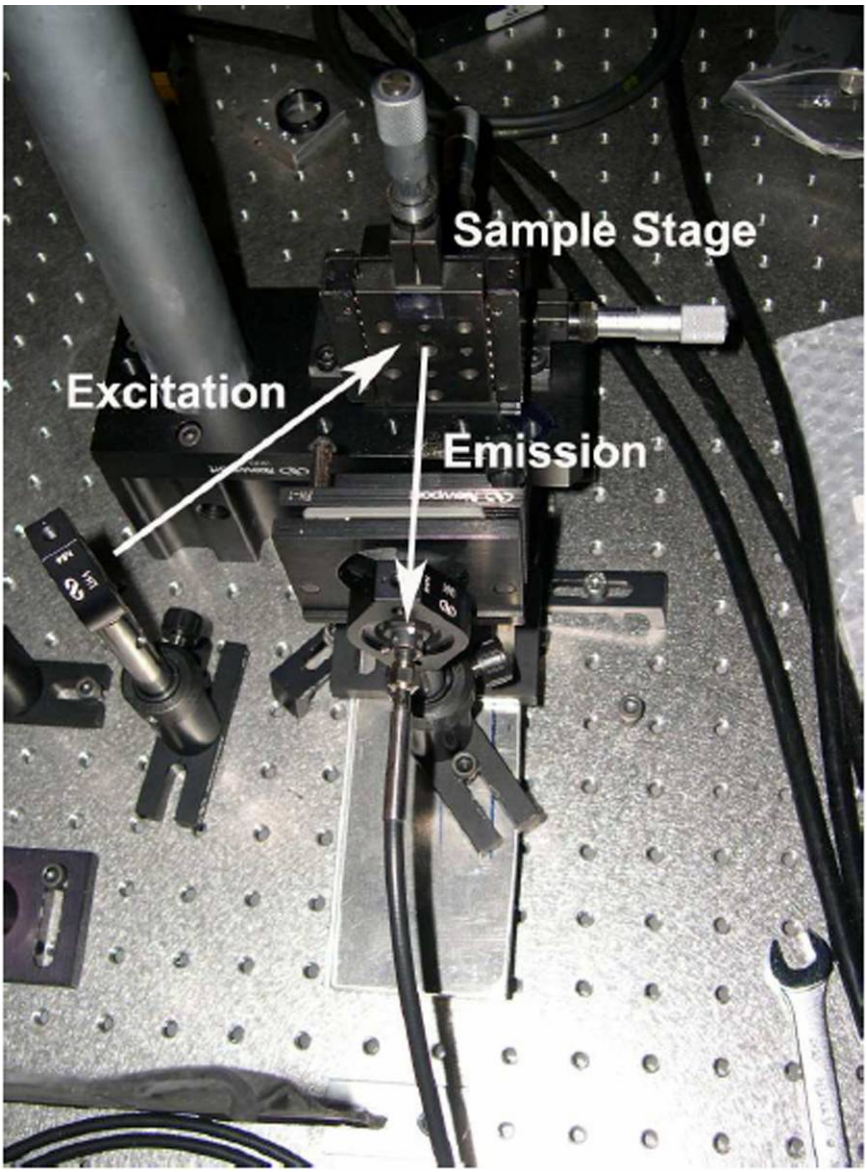

Figure 3.2: Sample setup for pulsed laser nitrogen laser photoluminescence (picture provided courtesy of Jeff King).

3.3 Results and Discussion

3.3.1 Chemical Incompatibility Between Barium Titanate and Silica

Most sol-gel synthesis techniques produce amorphous metal oxide products after the gel is dried. To produce a crystalline phase, the gel must be annealed to elevated temperatures. However, such heat treatment of a gel coating may result in a chemical reaction between the coating material and the substrate resulting in an undesirable product phase. For example, the $BaTiO_3$-SiO_2 binary phase diagram (Figure 3.3) reveals that these two oxides may form several barium-titanium-silicate compounds when heated [19]. Several authors have also reported that the direct deposition of $BaTiO_3$ on Si wafers is complicated by interdiffusion with the native SiO_2 layer which forms on the wafer [20-23]. Therefore, it was expected that direct application of thin sol-gel derived $BaTiO_3$ coatings on silica-based diatom frustules would result in an undesirable barium-titanium-silicate product phase.

To avoid the formation of such undesired silicate phases and produce continuous crack-free $BaTiO_3$ coatings, the underlying frustule/scaffold must possess good chemical and thermal compatibility (i.e., no reaction and similar coefficient of thermal expansion) with the $BaTiO_3$ phase. One such compatible material is magnesia (MgO). The BaO-TiO_2-MgO ternary phase diagram (Figure 3.4) reveals that MgO and $BaTiO_3$ share a tie line, which indicates that these two compounds are chemically compatible and that no new compounds can form between these oxides at ambient pressure [24]. Several techniques, such as, pulsed laser deposition (PLD) [25], RF magnetron sputtering [26], and laser molecular beam epitaxy [23], have successfully been utilized to deposit $BaTiO_3$ coatings on planar MgO surfaces. Also, the coefficient of thermal expansion for MgO ($12.6 \times 10^{-6}/^{o}C$) [27] is not far from that of cubic $BaTiO_3$ ($9.8 \times 10^{-6}/^{o}C$) [28]. Therefore,

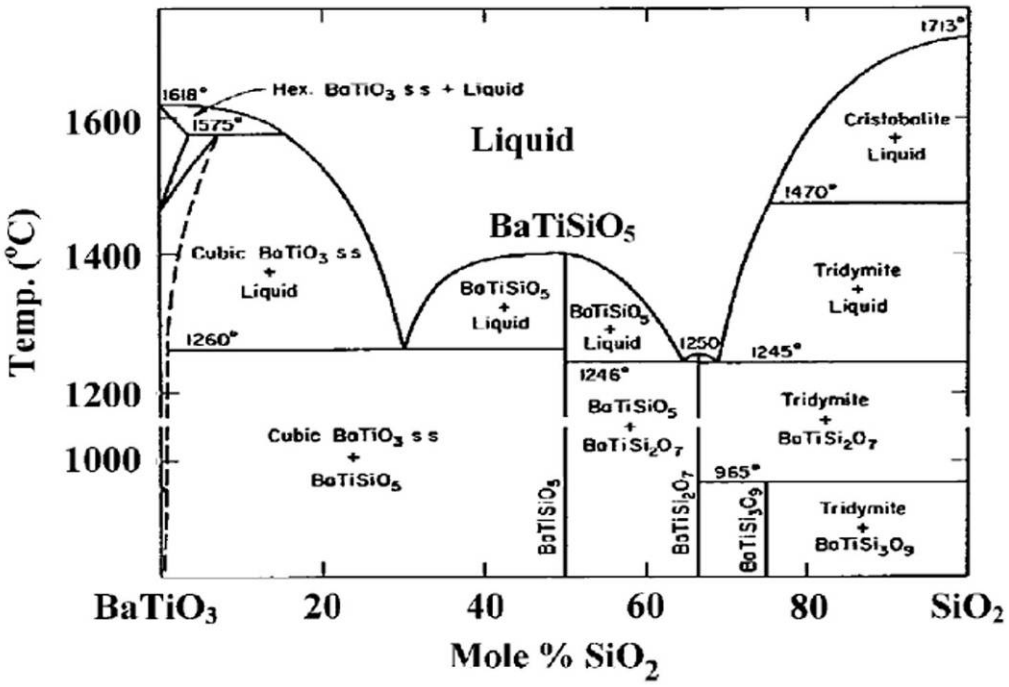

Figure 3.3: $BaTiO_3$-SiO_2 binary phase diagram (reprinted with permission from the American Ceramic Society) [19].

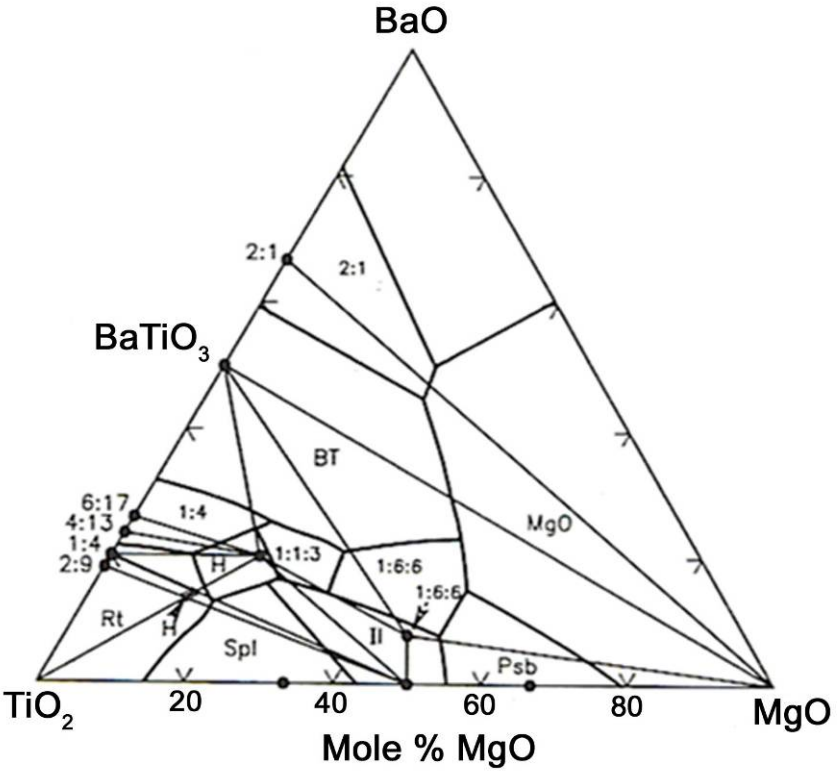

Figure 3.4: BaO-TiO_2-MgO ternary phase diagram (reprinted with permission from the American Ceramic Society) [24].

cracking, spalling, and inter-diffusion/reaction of the $BaTiO_3$ coating should be minimized by utilizing MgO as the scaffold material.

3.3.2 Conversion of Silica Diatom Frustules to Magnesia/Silicon Composite Replicas

It has been demonstrated by Sandhage, et al. that silica-based diatom frustules can be converted into MgO while retaining the micro- and nano- scale features of the original frustule [29]. Such conversion was conducted inside of sealed low carbon steel tubes to maintain control over the vapor species. The sealed reaction vessels were heated for 4 h at 900^{o}C in a horizontal tube furnace. The conversion took place by means of the following oxidation-reduction gas/solid displacement reaction:

$$2Mg(g) + SiO_2(s) \rightarrow 2MgO(s) + Si(s) \quad (3.1)$$

where the Si product can either be a solid or a liquid depending upon the reaction conditions. Optimization of the reaction conditions for obtaining the solid MgO and Si product phases was a major focus in this work to obtain suitable MgO-based replicas to be coated with $BaTiO_3$.

The formation of a solid Si product is expected if reaction (3.1) occurs under near stoichiometric reaction conditions. It is also possible for another solid intermetallic compound form if there is an excess of Mg(g) in the system. In this case, the Si product from reaction (3.1) can further react with the excess Mg(g) to form the following magnesium silicide (Mg_2Si) compound:

$$2Mg(g) + Si(s) \rightarrow Mg_2Si(s) \quad (3.2)$$

In the case where there is a large excess of Mg(g) present, a low melting point (638.6^{o}C) eutectic alloy of Mg-Si can be formed at a silicon composition of 1.16 atomic% as demonstrated in the Mg-Si phase diagram shown in Figure 3.5 [30]. Thus, the Si-bearing reaction products can include a liquid at reaction temperatures ≥ 638.6^{o}C.

Figures 3.6(a-d) are secondary electron (SE) images which show the morphology of the converted *Aulacoseira* frustules after reaction with Mg(g) at 900^{o}C for 1.5 h with Mg:SiO_2 ratios of 2.3, 2.5, 3.1, 3.7 : 1. An excess of Mg metal was used in all cases to ensure complete conversion of the silica frustules and also to account for the atmospheric oxygen which was sealed with the reactants inside of the steel reaction vessels. In all cases, the horizontal tube furnace was preheated to 900^{o}C and then the specimen-bearing steel reaction vessels were thrust into the hot zone. After the heat treatment was finished, the tubes were pushed to the end of the furnace tube to allow for cooling before the specimens were extracted (Note: such reactions were conducted using steel furnace tubes because mullite furnace tubes will crack when the specimens were thrust into and out of the furnace). The temperature inside the furnace was monitored using a reference thermocouple.

It was observed that the fine morphological features of the *Aulacoseira* frustules were preserved when the molar ratios of reaction (3.1) varied by as much as 4% above the stoichiometric ratio (Figures 3.6a-b). However, nodules were observed on the surface and in the pores of the frustules. Figure 3.7a is a representative EDS spectrum obtained when the nodules found on the surface of the frustules in Figures 3.6(a-b) were analyzed. This spectrum reveals a strong peak for Si with smaller peaks for Mg and O. The Mg and

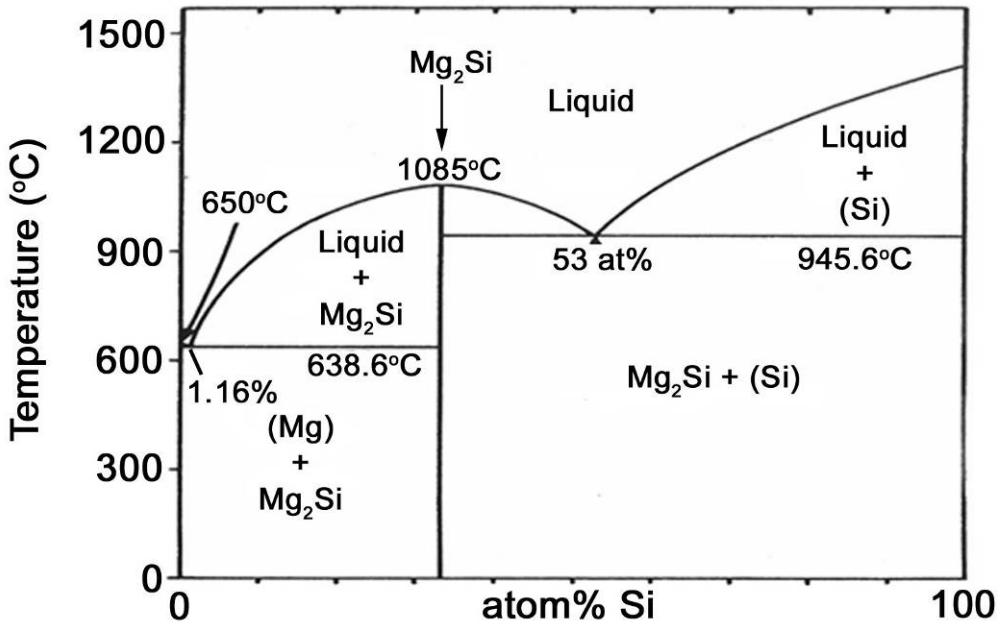

Figure 3.5: The Mg-Si phase diagram (reproduced with permission from the Metallurgical Society) [30].

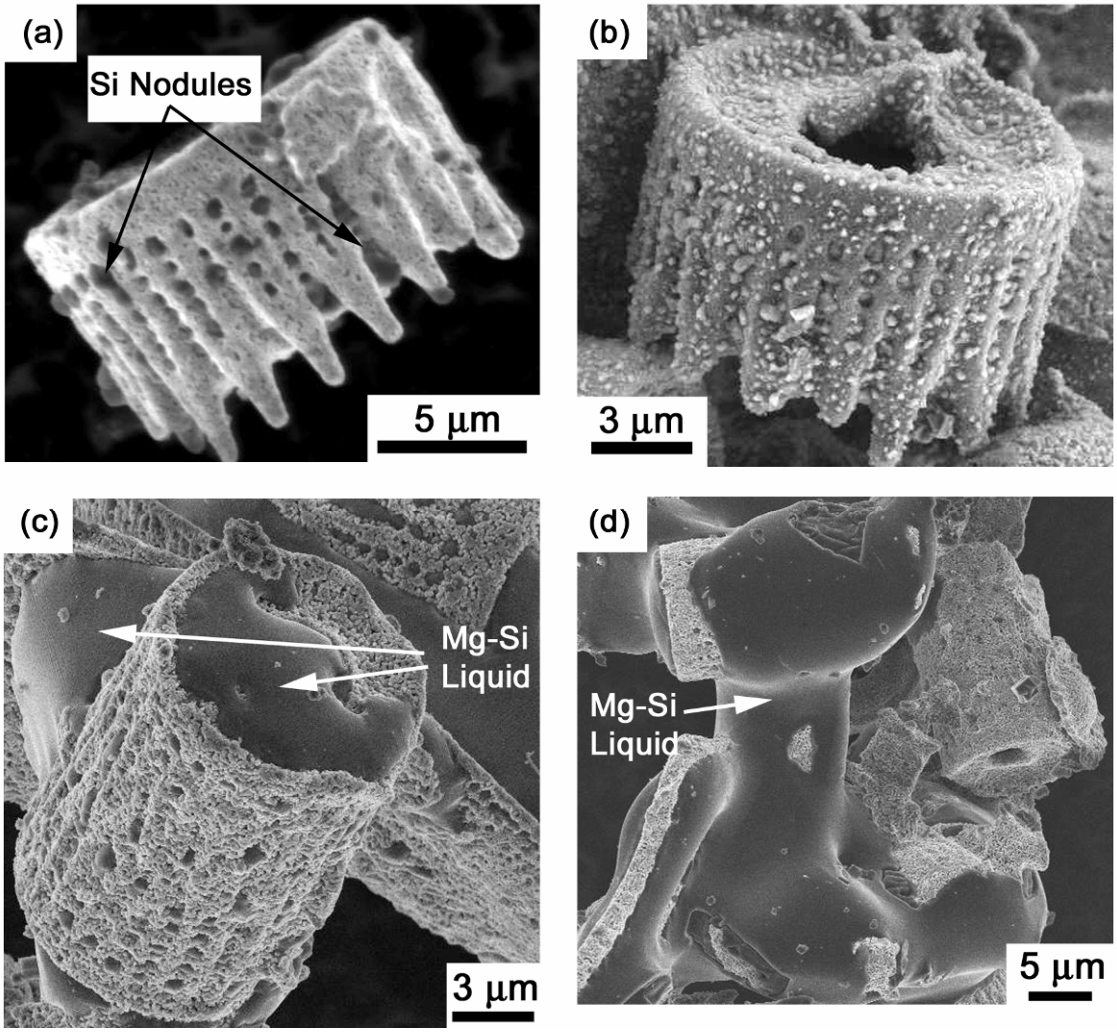

Figure 3.6: SE images of the MgO/Si composite *Aulacoseira* diatom frustules after reaction inside of sealed metal tubes at 900°C for 1.5 h with $Mg:SiO_2$ ratios of (a) 2.3:1, (b) 2.5:1, (c) 3.1:1, and (d) 3.7:1.

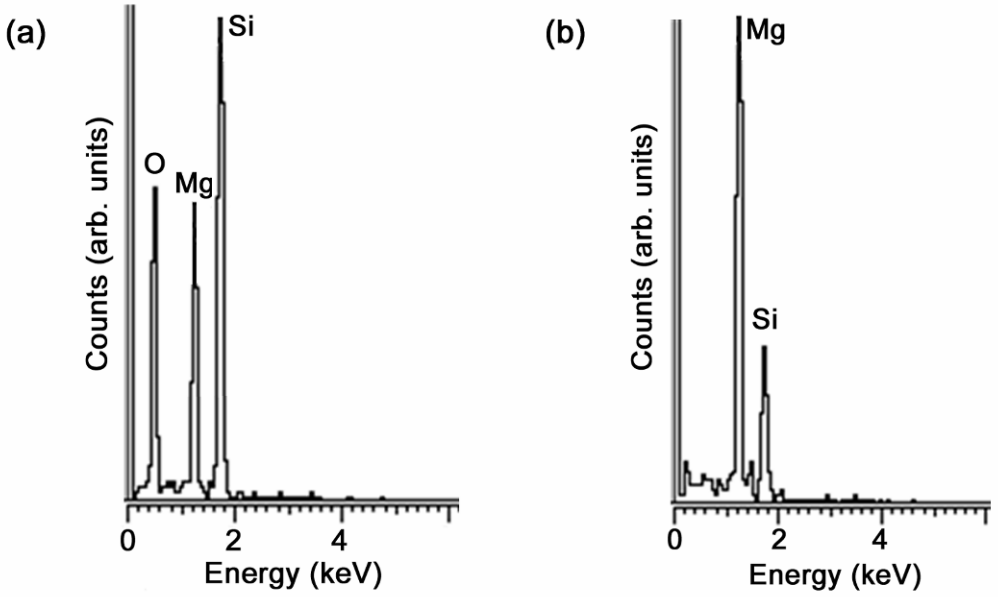

Figure 3.7: Energy dispersive spectroscopy conducted on: (a) the nodules shown in Figure 3.4(a-b) showing a Si rich phase and (b) the region labeled Mg-Si liquid in Figure 3.4(c-d) which shows that the liquid is a product of only Mg and Si phases with no oxide phases present. Note: there is an oxide phase present in (a) because the Si nodules are too small to be analyzed independently due to the interaction volume of ~ 1 μm of the electron beam.

O peaks are a result of analyzing the small Si nodules (~ 300 nm) with the electron beam which has an interaction volume of ~ 1 μm.

When the molar ratio of the volatile reaction species in reaction (3.1) was increased from the stoichiometric ratio by 9 and 12%, agglomerates of MgO frustules encased in a liquid like substance were observed as shown in Figures 3.6(c-d). EDS analyses (Figure 3.7b) performed on the liquid phases shown in Figures 3.6(c-d) revealed peaks for Mg and Si with no oxygen peaks. Under the given reaction conditions, the excess Mg(g) continued to react with the Si product phase after all of the oxygen from the SiO_2 reactant had been consumed, thus forming the Mg-Si liquid as predicted by the Mg-Si phase diagram (Figure 3.5). This liquid phase poured out of the frustules causing agglomeration of the product bed. It has been shown by Sandhage, et al. that such reaction conditions could be beneficial in producing MgO-rich frusutles inside of steel tubes, since the Mg-Si liquid will wet the steel tube and be drawn away from the frustule [29]. However, such reaction conditions are not desirable when converting large batches of frustules as complete Mg-Si liquid removal may be difficult to accomplish.

With the above results and discussion in mind, we will now analyze the thermodynamics of reactions (3.1) and (3.2) in the temperature range between 650-900^{o}C. The value for the Gibbs free energy change for reaction (3.1) is about 4.6 times more negative than reaction (3.2) [*]. This simple calculation reveals that magnesium would much rather form an oxide than a silicide at these temperatures. Thus, under the right reaction conditions, the Mg(g) should all be consumed via reaction with the oxide

[*] ΔG^{o}_{f} for reaction (3.1): at 650^{o}C is -324.49 kJ/mol and at 900^{o}C is -314.74 kJ/mol
ΔG^{o}_{f} for reaction (3.2): at 650^{o}C is -70.73 kJ/mol and at 900^{o}C is -64.47 kJ/mol

reactant and the formation of the Mg-Si liquid phase should be avoided. However, a reaction that occurs between a solid and a gas progresses through a sequence of steps. The first step involves the diffusion of the gaseous reactant through a gaseous film that surrounds the surface of the solid. The gas must then diffuse through the product layer which may be either porous or relatively dense. Once the gas diffuses through the product layer it can then react with the solid at the reaction interface. The last step usually involves the diffusion of the gaseous products back through the solid product and gaseous film layers [31]. However, when reaction (3.1) occurs, there are no gaseous products produced. Also, complete consumption of the SiO_2 reactant by Mg(g) to form 2 moles of MgO and 1 mole of Si requires an increase of 34.5% in the molar volume[†]. As a result, the last step in this reaction sequence may involve the transport of a Mg-Si liquid back through the product layer, or, some other type of accommodation of the internal stresses that arise due to the necessary volume increase for the reaction to occur.

The reduction of the internal stress may be accommodated by the transport of the Si product. The schematic shown in Figure 3.8 may be used to illustrate the region where the stress is expected to be localized and how this stress will be relieved via transport of the Si product through the pores to the surface of the frustules. If we assume that the reaction of a silica sphere (or frustule) proceeds by a shrinking core mechanism, such that a product layer of MgO and Si forms around the unreacted SiO_2 core, then each time a Mg atom reacts with an O atom the Si is displaced and an incremental volume increase occurs as stated previously. Thus, the product volume between X_R (reaction interface)

[†] $V_m[SiO_2] = 25.8\ cm^3/mol$; $V_m[MgO] = 11.3\ cm^3/mol$; $V_m[Si] = 12.1\ cm^3/mol$
(JCPDS Cards: #39-1425 for cristobalite SiO_2, #45-0946 for periclase MgO, #27-1402 for Si)

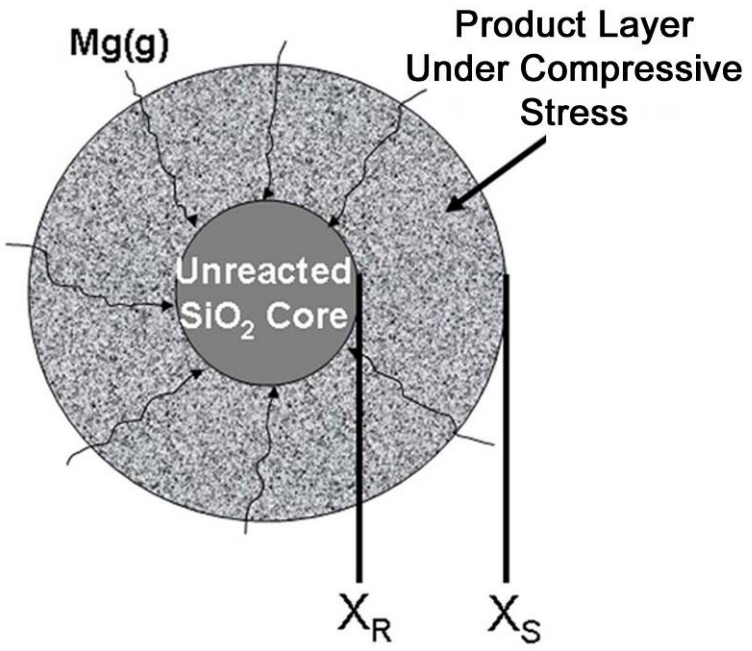

Figure 3.8: Schematic illustration of the product region formed around an unreacted SiO_2 core. A compressive stress may arise in the product region due to the volume increase (34.5%) associated with reaction (3.1). Consequently, the Si product may be forced to migrate along grain boundaries, dislocations, or pores in the product and deposit at free surfaces to relieve the internal stress.

and X_S (surface of the product layer) will be in a state of compression. In order to relieve the compressive stress in this product layer, the Si products may along paths of least resistance (i.e., along grain boundaries, dislocations, or pores) and deposit at free surfaces. This phenomenon (stress-induced migration of metallic reaction products) has also been observed in other reaction systems [32-34]. It has also been shown that the volume of the metallic nodules that appear on the surface is comparable to the difference in the volume increase that is necessitated by the reaction [34].

Although the formation of MgO in reaction (3.1) is thermodynamically more favored than the formation of Mg_2Si in reaction (3.2), the proximity of the reactant relative to the magnesium source also has a direct impact on Mg_2Si formation. For

example, Figure 3.9(a) shows a digital photo of a typical multicolored DE reaction product bed after conversion with Mg(g) ($Mg:SiO_2$ = 2.3:1) at 900^oC inside of the sealed steel tube reaction vessels. Over the course of the reaction, the frustules located closer to the reactant source were exposed to more of the Mg vapor than the frustules located near the end of the sealed tube. Consequently, the DE powder bed was not uniformly converted as demonstrated in Figure 3.9(a). This image shows four distinct colored regions which could be separated with a spatula and collected for XRD analyses.

XRD analysis performed on the blue region of the powder bed revealed diffraction peaks consistent with Mg_2Si, Si, and MgO, while the black region of the powder bed yielded peaks consistent with MgO and Si (Figure 3.9(b)). The brown regions consisted primarily of Mg_2SiO_4 and SiO_2 with smaller amounts of MgO and Si. It is important to note that the magnesium source would have been positioned in the lower right hand corner of Figure 3.9(a). The continued flux of Mg(g) past the Si product will convert the Si to the Mg_2Si intermetallic phase according to reaction (3.2) which also requires a volume increase of 218.84%. The formation of the Mg_2Si(s) product is usually accompanied with the Mg-Si liquid as pictured in Figure 3.6(c-d) which requires an excess (at least 69 atomic%) of Mg(g) to form both phases as predicted by the Mg-Si phase diagram (Figure 3.5).

Regardless of the reactant ratio, whether it is as low as 2.3:1 ($Mg:SiO_2$) or as high as 3.7:1 ($Mg:SiO_2$), it was observed that the reactant oxide powder bed was non-uniformly converted as shown in Figure 3.9(a). However, the desired product phase may be obtained by collecting the powder from the appropriate regions in the powder bed. Performing the reactions with higher Mg/SiO_2 reaction ratios simply produced more of

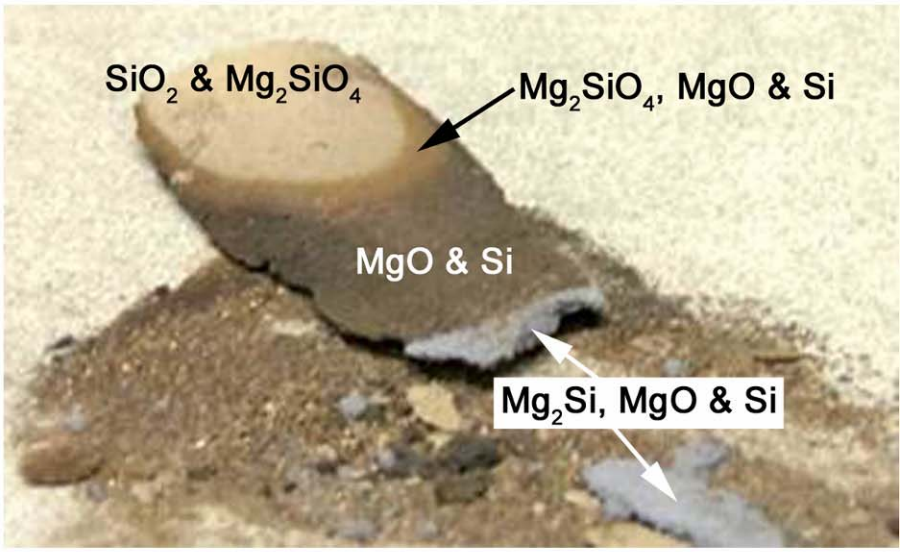

(a)

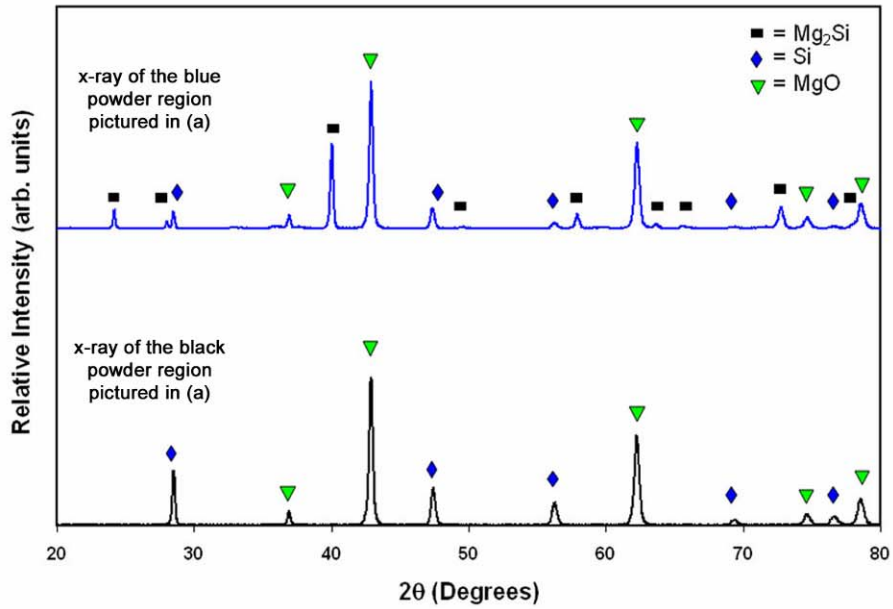

(b)

Figure 3.9: (a) A photograph displaying four distinct reaction zones of a diatom powder bed after conversion with Mg(g) (Mg:SiO_2 2.3:1) at 900°C for 1.5 h. (b) XRD analyses performed on the blue and black powder regions pictured in (a). The blue powder consists of Mg_2Si, Si, and MgO while the black powder region consists solely of MgO and Si.

the Mg_2Si(s) and Mg-Si(l) phases under the same heat treatment conditions and reaction times, as for reactions carried out under lower Mg/SiO_2 ratios. For the coating work presented in the following sections, the black powder regions containing the MgO/Si phases in the powder bed were always collected.

3.3.3 Sol-Gel Barium Titanate Coatings on Magnesia/Silicon Diatom Frustules

The black powder regions of the converted DE powder beds containing the MgO/Si composite frustules converted using $Mg:SiO_2$ reactant ratios ranging from 2.3-3.7:1 were utilized as scaffolds onto which $BaTiO_3$ coatings were applied using the refluxing/evaporation sol-gel technique. Barium titanium ethylhexano-isopropoxide was utilized as the sol-gel precursor because it is known that this alkoxide produces stoichiometric $BaTiO_3$ upon firing. The coating experiments were conducted by fixing the concentration of the alkoxide precursor while the frustule loading was varied.

The surface area of the diatom frustules was measured using BET (Brunauer-Emmet-Teller) nitrogen absorption analysis, conducted by Dr. Ben Church (Georgia Institute of Technology). The surface area of the as-received DE was measured to be 1.6 m^2/g. After reacting the DE frustules with Mg(g) at 900^oC for 1.5 h, the surface area increased slightly to 2.2 m^2/g (Figure 3.10(f)). In the following coating experiments, 0.1 g, 0.2 g, 0.3 g, and 0.4 g of the MgO/Si frustules were added to a solution with a fixed barium titanium ethylhexano-isopropoxide concentration.

The fixed concentration of the $BaTiO_3$ alkoxide precursor which was used in all of the coating experiments consisted of a solution of barium titanium ethylhexano-isopropoxide dissolved in absolute ethanol, along with smaller amounts of concentrated (29%) ammonium hydroxide, and deionised water. The molar ratio of

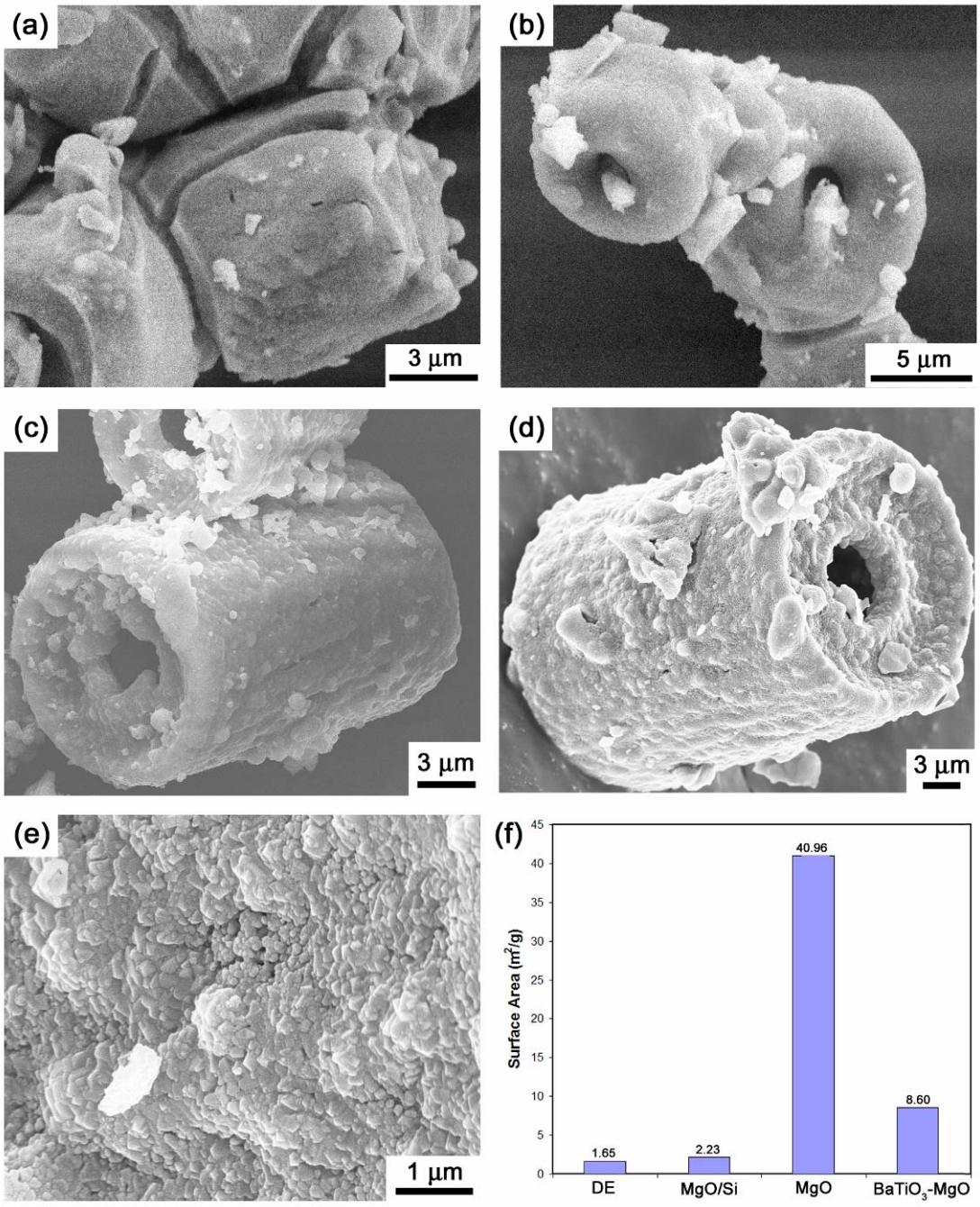

Figure 3.10: SE images of crystallized $BaTiO_3$ coatings after adding (a) 0.1 g, (b) 0.2 g, (c) 0.3 g, and (d-e) 0.4 g of the converted MgO/Si frustules to the barium titanium ethylhexano-isopropoxide solution (crystallization of the coating was performed at 700°C for 1.5 h). (f) BET analysis of the DE frustules in the as received state (DE), after converting with Mg(g) at 900°C for 1.5 h (MgO/Si), after selective dissolution of the Si using 0.49 M NaOH (MgO), after coating the Si free MgO frustules with Eu-doped $BaTiO_3$ ($BaTiO_3$-MgO).

$BaTi(OOC_8H_{15})(OC_3H_7)_5$: NH_4OH : H_2O : EtOH in the solution was 1.0 : 0.15 : 0.77 : 110. It is important to note that the water and ammonium hydroxide were first added to the ethanol in a 100 ml round bottom flask, after which the barium titanate precursor was added dropwise while the solution was stirred with a magnetic stirring bar to prevent precipitation of the precursor in the solution.

Typical reflux/evaporation coating experiments were performed by adding the MgO/Si frustules to the solution while stirring and refluxing at 70°C for 3 h. Controlled evaporation of 5 ml of the solution was then performed at 56°C. The refluxing treatment was then repeated for 1 more hour, after which 5 more ml of the solution were removed by evaporation. After refluxing for a final hour, the remaining volatile solution was allowed to evaporate at 56°C. In all cases, the coated frustules were then placed within a magnesia crucible and heated at 3°C/min in ambient air to 700°C and held for 1.5 h.

Figures 3.10(a-d) show typical SE images of the $BaTiO_3$-based coatings produced using 0.1g, 0.2g, 0.3g, and 0.4g of the MgO/Si powder after annealing at 700°C for 1.5 h. In each instance, continuous coatings were observed. However, thicker and mud-cracked coatings were observed in the coating system possessing a lower total template surface area (Figure 3.10(a)). This result was expected because the precursor will continue to polymerize with the previously adsorbed alkoxide layers on the diatom frustules over the course of the reflux and evaporation cycles. The hydrolysis and condensation reactions were activated on the MgO/Si frustules due to the presence of native OH groups on the MgO. After each of the evaporation steps, the solution became more viscous and gel-like which indicated further polymerization of the alkoxide. Consequently, a thicker gel-like network was obtained on the available surfaces where the reaction was initiated. One of

the adverse effects of thicker sol-gel coatings was that more solvent could be entrapped within the gel network. Upon heat treatment the trapped solvent evaporates from the gel-like network and mud-cracks formed due to the reduction in the volume of the original wet gel as shown in Figure 3.10(a).

The deposition experiments employing more total template surface area (accomplished by adding more MgO/Si templates) in the sol-gel coating system were more successful at replicating the microscale features of the frustules (Figure 3.10(d)). However, this coating approach was still unsuccessful in preserving the finer pore structure of the frustules due to over coating. Also, remaining $BaTiO_3$ particles in the form of globules were found to populate the surface of the coated frustules as well as surrounding areas (Figure 3.10(a-d)). Such globules may have formed as a result of the last evaporation step when all of the solvent was evaporated from the system. During this step, the remaining precursor condensed on all exposed surfaces including the round bottom flask. After the coating cycles were completed the coated frustules had to be scrapped from the sides of the flask with a spatula which invariably resulted in the removal of alkoxide which condensed on the flask as well. During the annealing process, the coated frustules were in intimate contact with the condensed "free alkoxide globules" which resulted in cross-linking and crystallization between the "globules" and the coated frustules. In hind site, vacuum filtration followed by thorough rinsing with ethanol, instead of complete evaporation of the solvent as the last step in the coating process, may have prevented the formation of such globules on the coated frustules.

XRD analyses were performed at each stage of this conversion process (Figure 3.11(a-1) to (a-4)). XRD analysis of the starting DE powder (Figure 3.11(a-1)) revealed

only SiO_2 (cristobalite) diffraction peaks. After reacting the frustules with Mg(g) at 900°C for 1.5 h (2.5:1 Mg:SiO_2), the cristobalite peaks were replaced with peaks corresponding to MgO, Si, and a small peak for Mg_2Si (Figure 3.11(a-2)) (Note: the Mg_2Si peak is a result of insufficiently separating the converted frustule powder bed). A SE image of such converted frustules was previously shown in Figure 3.6(b). Diffraction peaks corresponding to the $BaTiO_3$ phase were observed after annealing the $BaTiO_3$-based sol-gel coating which was applied to the converted MgO/Si frustules at 700°C for 1.5 h (Figure 3.11(a-3)). The relative intensities of the MgO and Si diffraction peaks in Figure 3.11(a-3) were similar to those for the uncoated MgO/Si composites. Other titanate (besides $BaTiO_3$) or silicate phases were not detected in the XRD patterns. These latter observations indicated that the barium titanate coating underwent negligible reaction with the underlying scaffold. Measurement of peak broadening in the XRD pattern and use of the Scherrer equation yielded an average $BaTiO_3$ crystallite size of 20 nm.

A transmission electron image, taken by Dr. Ye Cai (Georgia Institute of Technology), of a cross-section of a coated frustule is shown in Figure 3.11(b). A continuous, 150 nm thick coating was detected on the frustule surface. Selected area electron diffraction (SAED) analyses performed on the $BaTiO_3$-based coating (Figure 3.11(d)) were indexed for the (222), (202), (111), (101), (311), (110), (002), (211), and (301) planes of the tetragonal $BaTiO_3$ phase. SAED analyses performed on the underlying MgO/Si composite structure (Figure 3.11(c)) confirmed the presence of MgO, Si, and Mg_2Si as detected by XRD analysis. The $BaTiO_3$ grains were measured to be 10

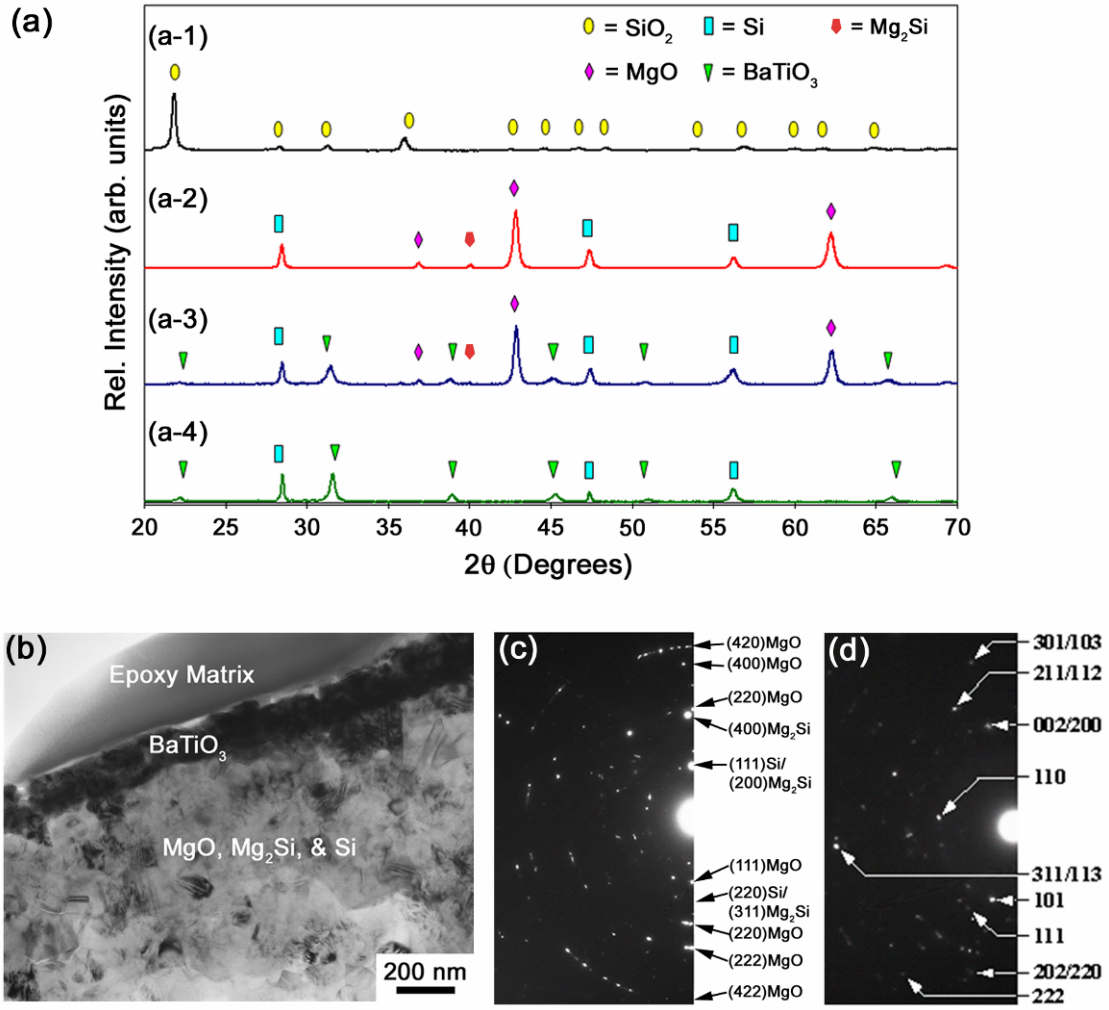

Figure 3.11: (a) XRD analyses performed on the as received DE (a-1), after reacting the DE with Mg(g) at 900°C for 1.5 h (2.5:1 Mg:SiO_2) (a-2), after coating 0.4 g of the MgO/Si frustules with a 0.1 M barium titanium ethylhexano-isopropoxide solution and annealing at 700°C for 1.5 h (a-3), after dissolving the underlying MgO scaffold in a 0.7 M HCl solution (a-4). (b) Transmission electron (TE) image, taken by Dr. Ye Cai (Georgia Institute of Technology), of a cross-section of an MgO/Si based frustule bearing a 150 nm thick $BaTiO_3$ coating. (c-d) Selected area electron diffraction (SAED) analysis confirming the presence of MgO, Si, and Mg_2Si in the underlying scaffold (c) and the tetragonal $BaTiO_3$ phase of the coating (d).

to 40 nm in size, which is consistent with the Scherrer analysis and the higher magnification SE image shown in Figure 3.10(e).

3.3.4 Dissolution of the Underlying Magnesia Template Using Hydrochloric Acid

The $BaTiO_3$-coated MgO-bearing frustules were magnetically stirred in a 0.7 M HCl solution at 60^{o}C for 1 h to selectively dissolve the underlying MgO scaffold in order to assess the conformal and continuous nature of the $BaTiO_3$ coating. After the acid treatment, the frustules were collected via vacuum filtration after rinsing with copious amounts of water. SE images of half frustules obtained after the HCl treatment are shown in Figures 3.12(a-c). Corresponding XRD and EDX analyses are shown in Figures 3.11(a-4) and 3.12(d), respectively. The absence of MgO diffraction peaks in the XRD pattern, and the absence of the Mg peak at 1.25 eV in the EDX pattern confirmed that the magnesia template was completely dissolved during this acid treatment (Note: Figure 3.10(d) is the EDS pattern obtained from a $BaTiO_3$-coated MgO-bearing template before the HCl treatment). Figure 3.12(b) shows a higher magnification SE image of the chipped region shown in Figure 3.12(a) which reveals the thin $BaTiO_3$ coating and the hollow inner structure of the coated template after dissolution of the MgO with HCl. Figure 3.12(c), which shows the backside of the frustule shown in Figure 3.12(a), reveals that the coating was continuous over the entire surface of the frustule. It should be noted that this particular frustule was not representative of the entire sample analyzed. The vast majority of the other frustules analyzed had similar morphologies as those shown in Figure 3.10(d) (i.e., the fine porous structure was filled in as a result of the coating). However, this is an isolated instance which demonstrates that it is possible to obtain thin conformal coatings on frustules using the refluxing/evaporation coating method. In any

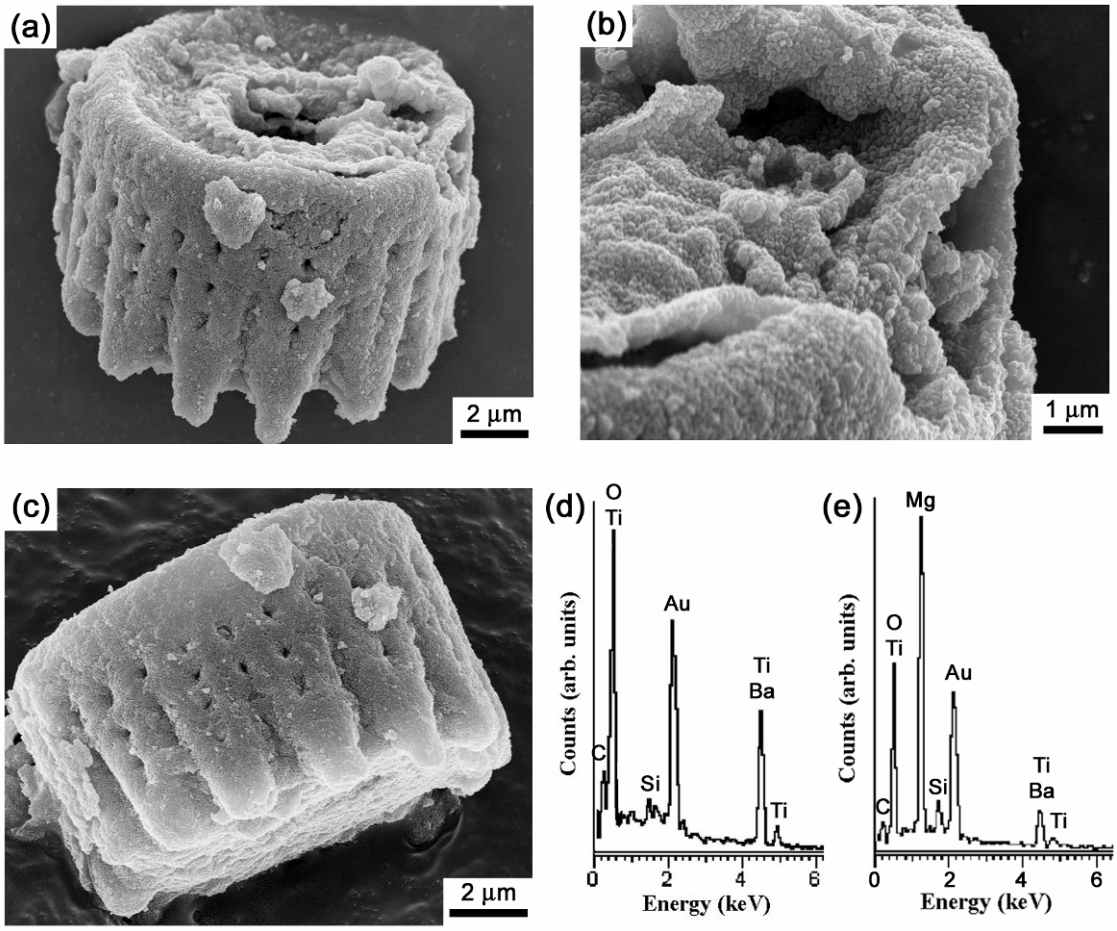

Figure 3.12: (a-c) SE images taken of a $BaTiO_3$-coated frustule after selective dissolution of the underlying MgO template using 0.7 M HCl at 60^{o}C for 1 h. The higher magnification image shown in (b) is of the chipped region shown in (a) which reveals the hollow inner structure of the coated frustule. Figure (c) shows the backside of the frustule shown in (a) which demonstrates that the coating was continuous over the entire surface of the frustule. Figures (d-e) are EDS spectra obtained after selective dissolution of the MgO scaffold with HCl (representative of the surfaces shown in a-c) (d) and a $BaTiO_3$ coating on an MgO-bearing frustule (e) for comparison sake.

event, after removal of the MgO, this $BaTiO_3$-bearing replica retained the cylindrical shape and fine features (fingerlike extensions, rows of fine pores) of the starting *Aulacoseira* frustule. Such shape and feature preservation is a clear indication that the sol-gel-derived $BaTiO_3$ coating was continuous and had conformed well to the underlying MgO template.

The silicon present in the magnesia/silicon composite frustule replicas may have been present as isolated silicon particles that had either migrated to the frustule surface (as shown in Figure 3.6(a-b)) or were entrained in the magnesia matrix. Thus, upon dissolution of the magnesia scaffold with HCl, the silicon nanoparticles may have simply fallen away from the $BaTiO_3$ coated structures. Another possibility was that the silicon could have also been entrained in the $BaTiO_3$ coating, at the coating/magnesia interface, prior to dissolution of the underlying magnesia template. The relative intensity of the Si diffraction peak did not decrease upon dissolution of the magnesia scaffold as demonstrated in Figure 3.11(a-4). In a group meeting of the coating team in Professor Ken Sandhage's group at the Georgia Institute of Technology (comprised of Phillip Graham, Zihao Bao, Dr. Ben Church, Dr. Ye Cai, and myself) it was hypothesized that the Si phase was possibly more interconnected than was previously thought and that such interconnected Si was contributing to the structural integrity of the coating. This hypothesis resulted in further investigation of the MgO/Si composite product phase. Z. Bao discovered that elemental Si diatom replicas could be obtained by dissolving the MgO with HCl. Further investigation demonstrated that the elemental Si diatom replicas could be produced by conducting reaction (3.1) at temperatures as low as 650^{o}C. Previous methods used to reduce silica to silicon (e.g., carbothermal reduction of silica)

required much higher (>2,000°C) temperatures [36]. This significant finding was published by Bao *et al.* in Nature [37].

3.3.5 Europium-Doped Barium Titanate Coatings on Magnesia Diatom Frustules

Phosphor microparticles with controlled 3-D shapes were fabricated using MgO-bearing diatom frustules as templates. The conversion of the SiO_2 *Aulacoseira* diatom frustules into MgO-based replicas was conducted using a Mg:SiO_2 molar ratio of 2.5:1 as described in Section 3.3.2. Because porous nanosized Si particles are known to possess photoluminescent properties [38], the Si product phase was dissolved from the MgO/Si composite frustule replicas so that it would not interfere with the luminescent properties of the applied Eu-doped $BaTiO_3$ coating. To dissolve the Si phase, the MgO/Si composite frustules were immersed in an aqueous 0.49 M NaOH solution for 3 h at 60°C in an ultrasonic bath. Figure 3.13(a) shows a SE image of an MgO frustule after the Si phase had been selectively dissolved with NaOH. The surface of the etched frustules is much smoother and no longer possesses the Si nodules observed in Figure 3.6(b). XRD analyses performed on the etched frustules reveal diffraction peaks which correspond solely for the MgO phase as shown in Figure 3.14(a-1). After this dissolution process, the surface area of the Si free MgO frustules increased to 41 m^2/g, as shown in Figure 3.10(f).

The reflux/evaporation coating technique was again utilized to apply a Eu-doped $BaTiO_3$ coating to the MgO-converted frustules. An ethanol-based precursor solution containing barium titanium ethylhexano-isopropoxide, europium (III) nitrate (Alfa Aesar), ammonium hydroxide, and deionized water was prepared with a molar $BaTi(OOC_8H_{15})(OC_3H_7)_5$: $Eu(NO_3)_3 \cdot 6H_2O$: NH_4OH : H_2O : EtOH ratio of 1.0 : 0.01 :

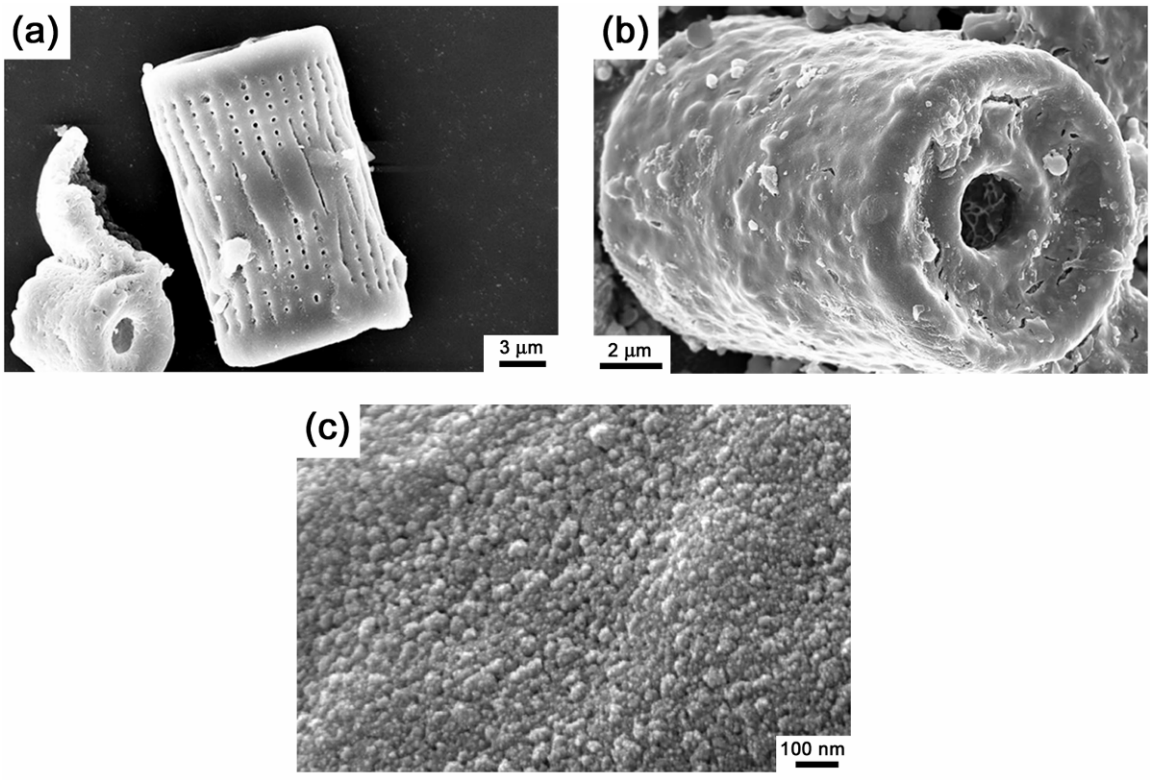

Figure 3.13: SE images of *Aulacoseira* diatom frustules (a) after dissolution of the residual Si-bearing phases in 0.49 M NaOH, and (b-c) are after coating the MgO frustule replicas with a Eu-doped $BaTiO_3$ layer and heat-treating for 1 h at 600^{o}C (c). Figure (c) is a higher magnification image of the Eu-doped $BaTiO_3$ grains on the surface of the specimen in (b).

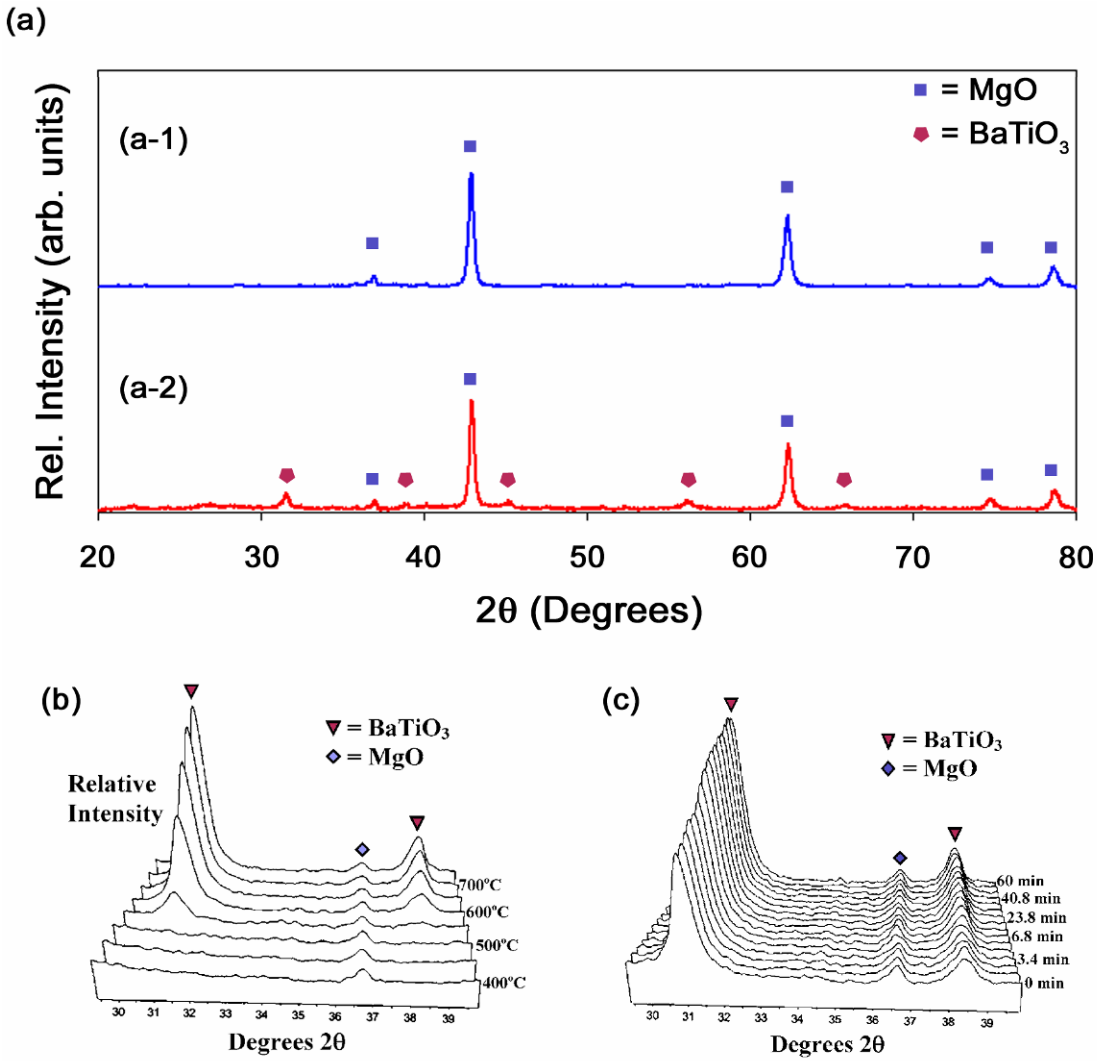

Figure 3.14: X-ray diffraction analyses of: (a-1) MgO frustule replicas after dissolution of the Si-bearing phases in 0.49 M NaOH at 60°C for 3 h, and (a-2) MgO frustule replicas coated with a Eu-doped $BaTiO_3$ layer (after heat treatment at 600°C). High temperature X-ray diffraction analyses of the sol-gel coated MgO replicas: (b) during heating (at 3°C/min) to 750°C and (c) for various times at 600°C.

1.5 : 1.4 : 110. A 0.4 g batch of the magnesia-converted frustules was immersed in 20 mL of this precursor solution. The mixture was stirred and refluxed at 100°C for 3 h, after which 8 mL of the solution was allowed to slowly evaporate at 56°C. The refluxing treatment was repeated for another 1.5 h at 100°C, after which 5 mL more of the solution was allowed to evaporate. After a final 1.5 h refluxing step, the remaining volatile solution was allowed to evaporate at 56°C. After drying for 1 h at 100°C, the coated frustules were heat treated in air at 600°C for 1 h (ramp = 3°C/min).

The heat treatment temperature was carefully chosen because previous studies have shown that annealing temperature and Eu doping concentrations of $BaTiO_3$ have dramatic affects on the photoluminescent (PL) intensity of the resulting material. Hreniak *et al*. have reported that increasing the annealing temperature from 750°C up to 1100°C will directly affect the intensity of the $^5D_0 \rightarrow {}^7F_1$ (magnetic) transition while the intensity of the $^5D_0 \rightarrow {}^7F_2$ (electric-dipole) transition is unaffected due to an increased number of Eu^{3+} inversion symmetry sites [39]. Li and Kuwabara have reported that the intensity of the $^5D_0 \rightarrow {}^7F_2$ transition is significantly increased up to a sintering temperature of 600°C but drastically declines at heat treatments >600°C [15]. They concluded that such behavior suggests that a reduction of the europium from a valence state of 3+ to 2+ occurs at temperatures higher than 600°C which yields rapid quenching of the Eu^{3+} emission [15].

Figures 3.13(b-c) reveal SE images of MgO frustule replicas coated with Eu-doped $BaTiO_3$ and heat treated at 600°C for 1 h. A continuous granular coating (Figure 3.13(c)) with minor mud cracks was observed on the surface. Residual alkoxide globules were also present on the frustule surfaces. Such globules were also present for the non-

doped $BaTiO_3$ coatings and could be the result of completely evaporating the volatile solvent as discussed in Section 3.3.3.

The temperature at which $BaTiO_3$ formation commenced on the coated MgO replicas during heating was evaluated with high-temperature X-ray diffraction (HTXRD) analyses. A series of diffraction patterns obtained during heating from 400°C up to 750°C at a rate of 3°C/min are shown in Figure 3.14(b). These patterns revealed that the formation of crystalline $BaTiO_3$ started between 500 and 550°C. HTXRD analyses were then conducted for various times at a constant temperature of 600°C, as shown in Figure 3.14(c). There was little change in the relative intensities of the $BaTiO_3$ diffraction peaks between 30 and 60 min at 600°C, which indicated that $BaTiO_3$ formation was completed well within the 1 h treatment at this temperature. A room temperature XRD pattern obtained over a wider range of 2θ values after the 600°C/1h treatment is shown in Figure 3.14(a-2). Only diffraction peaks associated with MgO and $BaTiO_3$ were detected.

Transmission electron images, taken by Dr. Ye Cai (Georgia Institute of Technology), of cross-sections of the coated MgO frustule replicas are shown in Figure 3.15(a-c). The lower magnification image shown in Figure 3.15(a) revealed that the coating was continuous around the perimeter of the MgO frustule replica. The measured coating thickness ranged from 110 nm to 280 nm. Although there was a significant local variation in the thickness of the coating, it was still continuous and submicrometer in thickness. A higher-resolution TE image in Figure 3.15(b) shows that the coating was comprised of 10-50 nm crystallites. A high resolution TE image showing the lattice fringes (Figure 3.15(c)) and electron-diffraction analysis (Figure 3.15(d)) confirmed that these fine crystallites were comprised of the tetragonal barium titanate phase. Strek et al.

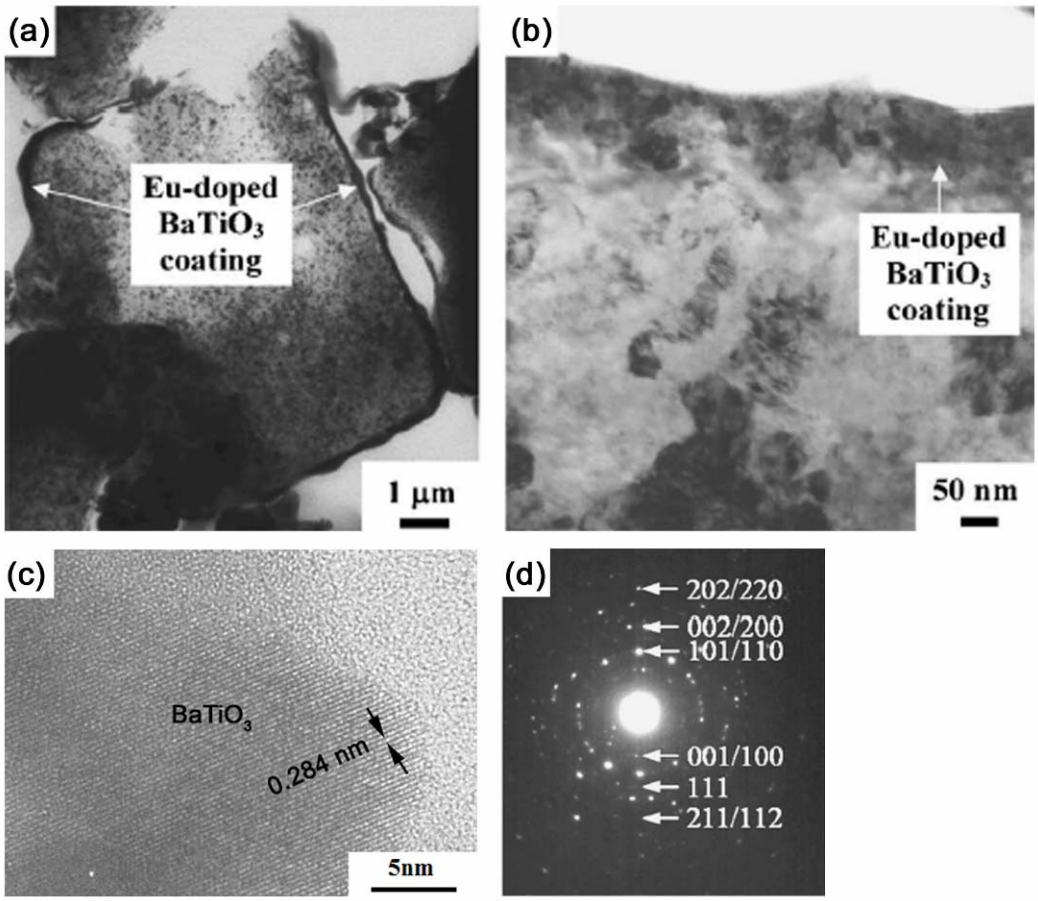

Figure 3.15: Transmission electron microscopy images of cross-sections of Eu-doped $BaTiO_3$ coatings on converted MgO frustules after heat treatment at 600°C for 1 h: (a) low magnification TE image of a cross section of a complete MgO frustule replica bearing a submicrometer thick Eu-doped $BaTiO_3$ coating, (b) higher magnification TE image revealing 10 – 50 nm diameter Eu-doped $BaTiO_3$ crystallites, (c) high magnification TE image revealing the lattice spacing of a $BaTiO_3$ crystallite consistent with tetragonal $BaTiO_3$, and (d) SAED of the coating area in (b) which also confirmed the presence of the $BaTiO_3$ tetragonal phase.

have also reported that the tetragonal $BaTiO_3$ crystal structure is stabilized by doping with Eu^{3+} ions [40].

The room-temperature photoluminescence (PL) spectrum obtained from the Eu-doped $BaTiO_3$-coated MgO frustule replicas after stimulation with 337 nm (UV) light is shown in Figure 3.16(a). Six emission bands characteristic of intra-4*f*-shell transitions from Eu^{3+} ($^5D_0 \rightarrow {}^7F_j$ with j = 0, 1, 2, 3, 4, 5) were detected at 580, 593, 613, 653, 694, and 704 nm [15]. As observed by Li and Kuwabara for Eu-doped $BaTiO_3$, the $^5D_0 \rightarrow {}^7F_2$ transition yielded the most intense (bright red) emission band [15]. Figure 3.16(b) shows a digital photograph of the observed red emission that was taken during the PL experiments. Bright red emission was also observed from single frustules observed under a fluorescence microscope (Figure 3.16(c)). The width of the $^5D_0 \rightarrow {}^7F_2$ emission peak at half of the maximum intensity (18 nm, Figure 3.16(a)) was also similar to that observed by Li and Kuwabara (16 nm) for sol-gel-derived Eu-doped $BaTiO_3$. These authors reported that the intensity of the $^5D_0 \rightarrow {}^7F_2$ transition increased as the heat-treatment temperature of Eu-doped $BaTiO_3$ was increased up to 600°C [15]. However, a further increase in temperature up to 700°C resulted in a significant reduction in the intensity of this emission, which was attributed to partial reduction of the Eu valence state (from 3+ to 2+) [15]. Hence, the relatively bright red emission observed in the present work was a direct result of the ability to synthesize continuous coatings of Eu-doped $BaTiO_3$ on compatible MgO frustule replicas with a modest 600°C/1 h heat treatment.

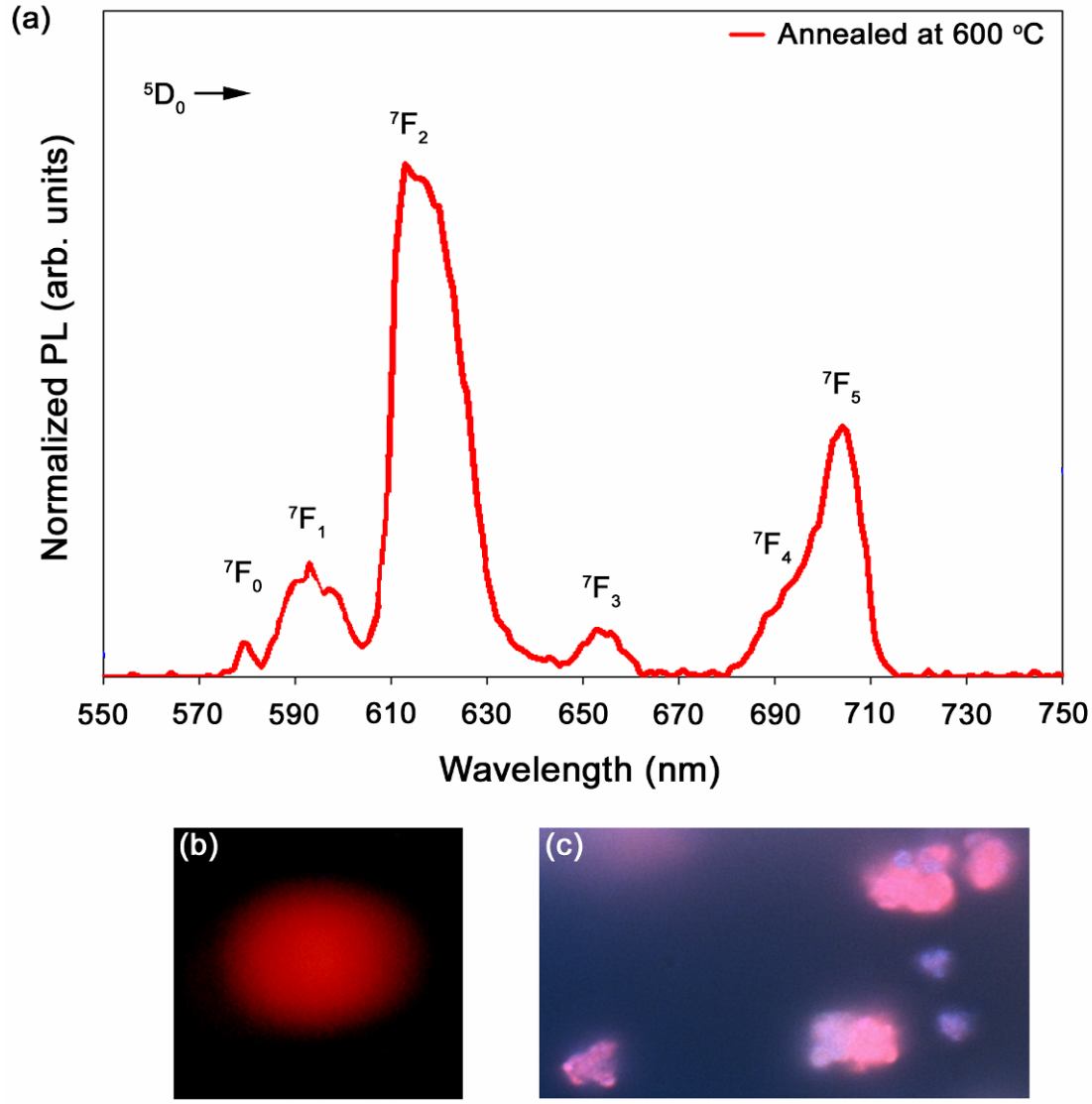

Figure 3.16: (a) Room temperature PL spectra obtained by exciting the Eu-doped $BaTiO_3$ coated MgO frustules with a 337 nm (UV) source. The bright red emission resulting from the $^5D_0 \rightarrow {}^7F_2$ transition is observed in (b). A fluorescence microscope in (c) reveals the bright red emission from single diatoms.

3.4 Summary and Outlook

This work has demonstrated a multi-step process for applying thin barium titanate-based coatings on diatom frustules. The silica based chemistries of diatom frustules are not chemically compatible with barium titanate so the silica frustules were first converted to magnesia to circumvent such incompatibility. Sol-gel based coatings were applied to the magnesia-based templates using a reflux/evaporation deposition technique. The underlying magnesia could then be dissolved with hydrochloric acid so as to yield barium titanate replicas of the diatom frustules. Europium activator ions were successfully incorporated into the barium titanate lattice to endow the coated frustules with bright red photoluminescence. Such coatings applied on diatom frustules provide enhanced control over the phosphor particle size and shape which could ultimately yield higher quality particle-based phosphor coatings.

The work presented in this Chapter demonstrates that the reflux/evaporation coating technique is capable of coating nano-patterned 3-D microparticles with complex alkoxide-derived chemistries. This coating technique appears to be sufficient for applying relatively uniform coatings on 3-D substrates. However, this approach fails to provide strict control over the coating thickness. Also, the generation of excess inorganic particles on the frustule surface, as well as in surrounding areas, is a problem which needs to be overcome using this technique. Filtration of the precursor, as opposed to complete evaporation, may be a means of avoiding the formation of globular precipitates on the template surfaces. In any case, the lack of control over the thickness of the coating with this reflux/evaporation deposition technique led to the development of a more controlled, automated surface sol-gel deposition technique.

3.5 References

[1] M. F. Yan, T. C. D. Huo, H. C. Ling, *Journal of the Electrochemical Society*, **134**, 493 (1987).

[2] K. Ohno, T. Abe, *Journal of the Electrochemical Society*, **141**, 1252 (1994).

[3] S. Oshio, T. Matsuoka, S. Tanaka, H. Kobayashi, *Journal of the Electrochemical Society*, **145**, 3893 (1998).

[4] Y. C. Kang, H. S. Roh, S. B. Park, *Journal of the Electrochemical Society*, **147**, 1601 (2000).

[5] F. Duault, M. Junker, P. Grosseau, G. Guilhot, P. Iacconi, B. Moine, *Powder Technology*, **154**, 132 (2005).

[6] Y. C. Kang, E. J. Kim, D. Y. Lee, H. D. Park, *Journal of Alloys and Compounds*, **347**, 266 (2002).

[7] S. Oshio, K. Kitamura, T. Shigeta, S. Horii, T. Matsuoka, S. Tanaka, H. Kobayashi, *Journal of the Electrochemical Society*, **146**, 392 (1999).

[8] L. Ozawa, M. Itoh, *Chemical Reviews*, **103**, 3835 (2003).

[9] L. E. S. Rohwer, R. J. Walko, *Handbookof Luminescence, Display Materials, and Devices*, American Scientific Publishers, Stevenson Ranch, CA, 209 (2003).

[10] K. Y. Sasaki, J. B. Talbot, *Advanced Materials*, **11**, 91 (1999).

[11] S. Park, S. Kang, *Journal of Materials Science: Materials and Electronics*, **14**, 223 (2003).

[12] M. Anitha, P. Ramakrishnan, A. Chatterjee, G. Alexander, H. Singh, *Applied Physics A*, **74**, 153 (2002).

[13] F. E. Round, R. M. Crawford, D. G. Mann, *The Diatoms: Biology & Morphology of the Genera*, Cambridge University Press, Cambridge (1990).

[14] M. Hildebrand, R. Wetherbee, *Progress in Molecular and Subcellular Biology, Springer-Verlag, Berlin*, 11-57 (2003).

[15] J. Li, M. Kuwabara, *Science and Technology of Advanced Materials*, **4**, 143 (2003).

[16] C. Eylem, G. Saghi-Szabo, B. H. Chen, b. Eichhorn, J. L. Peng, R. Greene, L. Salaanca-Riba, S. Nahm, *Chemistry of Materials*, **4**, 1038 (1992).

[17] D. Kolar, *Materials Research Society Symposium Proceedings*, **453**, 425 (1997).

[18] H. Kishi, N. Kohzu, J. Sugino, H. Ohsato, Y. Iguchi, T. Okuda, *Journal of the European Ceramic Society*, **19**, 1043 (1999).

[19] D. E. Rase, R. Roy, *Journal of the American Ceramic Society*, **38**, 389-395 (1995).

[20] S. Kim, S. Hishita, *Thin Solid Films*, **281**, 449 (1996).

[21] J. G. Lisoni, M. Siegert, C. H. Lei, w. biegel, J. Schubert, W. Zander, Ch. Buchl, *Thin Solid Films*, **389**, 219 (2001).

[22] C. H. Lei, C. L Jia, M. Siegert, J. Schubert, Ch. Buhal, K. Urban, *Journal of Crystal Growth*, **204**, 137 (1999).

[23] X. Wei, Y. I, J. Zhu, Z. Liang, Y. Zhang, W. Huang, S. Jiang, *Applied Surface Science*, **252**, 1442 (2005).

[24] R. S. Roth, w. S. Brower, M. Austin, M. Koob, *Phase Diagrams for Ceramists*, The American Ceramic Society, Westerville, OH, 6, 264 (1987).

[25] G. Yang, W. Wang, L. Yan, H. Lu, G. Yang, Z. Chen, *Optics Communications*, **209**, 445 (2002).

[26] Y. Yoneda, H. Kasatani, H. Terauchi, Y. Yano. T. Terashima, Y Bando, *Journal of Crystal Growth*, **150**, 1090 (1995).

[27] T. Chen, X. M. Li, S. Zhang, *Solid State Communications*, **131**, 523 (2004).

[28] B. Jaffe, W. R. Cook, H. Jaffe, *Piezoelectric Ceramics*, Academic Press, Marietta, OH, 49-114 (1971).

[29] K. H. Sandhage, M. B. Dickerson, P. M. Huseman, M. A. Carana, J. D. Clifton, T. A. Bull, T. J. Heible, W. R. Overton, M. E. A. Schoenwaelder, *Advanced Materials*, **14**, 429 (2002).

[30] R. Gefken, E. Miller, *Transactions of the Metallurgical Society of AIME*, **242**, 1968-2323 (1968).

[31] F. Habashi, *Principles of Extractive Metallurgy*, Gordon & Breach, Science Publishers, New York (1969).

[32] S. Vilayanur, K. H. Sandhage, *Oxidation of Metals*, **55**, 87-103 (2001).

[33] J. R. J. Mackert, R. D. Tingle, C. W. Fairhurst, *Journal of Dental Research*, **62**, 1229-1235 (1983).

[34] S. Guruswamy, S. M. Park, J. P. Hirth, R. A. Rapp, *Oxidation of Metals*, **26**, 77-103 (1986).

[35] J. R. Wynnyckyj, D. B. Rao, *High Temperature Science*, **8**, 203-217 (1976).

[36] M. Nagamori, I. Malinsky, A. Claveau, *Metallurgical Transactions B*, **17**, 503-514 (1986).

[37] Z. Bao, M. R. Weatherspoon, S. Shian, Y. Cai, P. D. Graham, S. M. Allan, G. Ahmad, M. D. Dickerson, B. C. Church, Z. Kang, H. W. Abernathy III, C. J. Summers, M. Liu, K. H. Sandhage, *Nature*, **446,** 172-175 (2007).

[38] A. G. Cullis, L. T. Canham, *Nature*, **353**, 335-338 (1991).

[39] D. Hreniak, W. Strek, J. Amami, Y. Guyot, G. Boulon, C. Goutaudier, R. Pazik, *Journal of Alloys and Compounds*, **380**, 348-351 (2004).

[40] W. Strek, D. Hreniak, G. Boulon, T. Guyot, R. Pazik, *Optical Materials*, **24**, 15-22 (2003).

CHAPTER 4: CONFORMAL SURFACE SOL-GEL COATINGS ON 3-D NANOSTRUCTURED TEMPLATES VIA HYDROXYL AMPLIFICATION

The research presented in this chapter has been reported in the following publication:

iv) M. R. Weatherspoon, M. B. Dickerson, G. Wang, Y. Cai, S. Shian, S. C. Jones, S. R. Marder, K. H. Sandhage, *Angew. Chem. Int. Ed.*, **46**, 5724-727 (2007).

4.1 Introduction

In the last Chapter, a conventional sol-gel process was used for conformally coating nanostructured *Aulacoseira* diatom frustule templates with barium titanate and europium-doped barium titanate. After performing many experiments using this deposition method, it was apparent that it would be difficult to apply coatings which would retain all of the fine features of the majority of the frustules. Other reaction processes, such as gas-solid reactions [1, 2] and atomic layer deposition (ALD) [3], have successfully been utilized to alter the chemistries of such 3-D nanostructured templates. However, both these processes require volatile reactants or precursors. Also, reaction systems, such as ALD, are usually dedicated for processing a single chemical composition (e.g., TiO_2 or Al_2O_3) to avoid cross contamination between samples. On the other hand, sol-gel processing provides an alternate range and combination of chemistries which may be used to alter the frustules chemistry. However, controlled formation of conformal ultrathin sol-gel-based coatings on 3-D nanostructured templates remains a significant fabrication challenge.

A little over a decade ago, Kunitake and his co-workers developed a sol-gel process which they named, the surface sol-gel process [4]. In this process, stepwise

hydrolysis of chemisorbed metal alkoxide precursors with surface hydroxyl or carboxyl groups results in highly-controlled monolayer growth of metal oxide films [4-8]. This process is a wet chemical analog to ALD in that it is a surface limited reaction process as described earlier in Section 1.3.2. Control over the coating thickness is achieved by the number of deposition cycles performed [4, 10]. Partially condensed alkoxide solutions may also be used to controllably deposit thicker layers per adsorption cycle using this process [4]. This feature would be attractive for applications that call for submicron thick coatings but do not require atomic level control over the coating thickness. Also, because the surface sol-gel process breaks up the hydrolysis and condensation reactions into separate steps, more compact coatings can be obtained using this process as opposed to conventional sol-gel processing techniques [9].

Surfaces terminated with hydroxyl or carboxyl functionalities are a prerequisite for obtaining conformal and continuous coatings using the surface sol-gel process [4-8]. It has been shown that metal surfaces that do not possess hydroxyl groups can be functionalized with mercaptoethanol (for gold surfaces) [4, 10, 11], or exposure to aggressive oxidizing solutions such as RCA or Piranha (for Si of Ti surfaces) [9, 12]. However, little work has been performed to suitably functionalize oxide substrates for surface sol-gel processing. One of the drawbacks to utilizing diatomaceous earth (DE) as a nanostructured template is that mining companies will usually flame polish the DE before they sell it to a customer. Flame polishing converts the amorphous native silica phase of the diatom frustule to a crystalline (normally cristobalite) phase and in the process degrades the silanol (Si-OH) concentration on the frustules. In this dissertation Chapter, a dendritic amplification procedure was employed for amplifying hydroxyl

groups on surfaces possessing low hydroxyl concentrations. Such dendritic amplification of reactive functional groups was expected to enhance the surface sol-gel deposition of alkoxide precursors on the surface of the frustules.

In this study, tin oxide (SnO_2) was coated on diatom frustules because SnO_2 is a well known semiconductor material and has been utilized as a sensor for detecting poisonous and explosive gases such as NO_x, NO_2, CO, H_2 [13-20]. Therefore, electrochemical (gas-sensing) experiments could be employed as an alternate means of determining the continuity of the applied coating on the diatom frustule surface.

4.2 Experimental Procedure

4.2.1 Hydroxyl Group Amplification on *Aulacoseira* Diatom Frustules

The silica-based *Aulacoseira* diatom frustules were cleaned by the following treatment. A 25 g quantity of frustules was first exposed to a 200 ml solution of 50% concentrated HCl in methanol for 1 h at room temperature. After filtration from this solution, the frustules were rinsed with purified water (18.2 MΩ water from a NANOpure DIamond UV/UF system, Barnstead International, Dubuque, IA). The frustules were then exposed to an RCA-1 solution comprised of a 5:1:1 mixture of pure water, concentrated NH_4OH, and 30% H_2O_2 and magnetically stirred at 65°C for 0.5 h. After filtration, the frustules were rinsed again with pure water.

Glucosamine-functionalized diatom frustules were synthesized via the following treatment. The frustules were silanized via refluxing for 16 h in a solution comprised of 20 ml of (3-aminopropyl)triethoxysilane (98% purity, Fluka, Seelze, Germany), 7 ml of concentrated NH_4OH, and 173 ml of pure water. After removal from the solution by filtration, the silanized frustules were rinsed with pure water, and then heated to 105°C

for 0.5 h under vacuum. In order to increase the concentration of amines on the frustule surfaces, the silanized frustules were exposed, in an alternating fashion, to solutions containing dipentaerythritol penta-/hexa-acrylate (Sigma Aldrich, Milwaukee, WI) or tris(2-aminoethyl)amine (Fluka). The frustules (25 g) were first stirred for 1 h in 200 ml of a 20 wt% solution of dipentaerythritol penta-/hexa-acrylate in ethanol. After filtration and rinsing with 600 ml of ethanol, the frustules were then stirred for 1 h in 200 ml of a 20 wt% solution of tris(2-aminoethyl)amine in ethanol. This process of exposure to the dipentaerythritol penta-/hexa-acrylate solution, and then to the tris(2-aminoethyl)amine solution, was repeated twice. A final exposure to the dipentaerythritol penta-/hexa-acrylate solution was then conducted (i.e., for a total of 3 exposures to the dipentaerythritol penta-/hexa-acrylate solution and 2 exposures to the tris(2-aminoethyl)amine solution). The frustules were then immersed for 1 h in a solution comprised of 25 g of glucosamine (D-glucosamine HCl, 99% purity, Fluka) dissolved in 300 ml of an aqueous 50 mM sodium carbonate solution that was adjusted to pH 8 with 1 M NaOH. The glucosamine-functionalized frustules were filtered from the solution, rinsed with purified water, and then dried for 16 h at 50°C.

4.2.2 Surface Sol-Gel Depositions of Tin Oxide on *Aulacosiera* Frustules

Tin oxide coatings were applied to the glucosamine-functionalized diatom frustules using an automated surface sol-gel pumping system. The glucosamine-functionalized frustules (0.8 g) were placed on a fine-porosity glass frit in a 1-L microfiltration assembly (Kontes Ultraware Microfiltration Assembly, Fisher Scientific). The computer-controlled pumping system was then used to expose the frustules in an alternating fashion to a tin alkoxide solution, a propanol solution, and then an aqueous

ammonium hydroxide solution. A 15 ml volume of a 0.01 M solution of tin (IV) isopropoxide (10 % w/v, 98% metals basis, Alfa Aesar, Ward Hill, MA) dissolved in anhydrous 2-propanol (Chemat Technology, Northridge, CA) was pumped into the microfiltration assembly so as to immerse the functionalized frustules. The tin alkoxide was allowed to react with the hydroxyl groups of the glucosamine-functionalized frustules for 5 minutes, after which the alkoxide solution was removed by vacuum filtration. A 15 ml volume of 2-propanol was then pumped into the microfiltration assembly, and removed by vacuum filtration, so as to rinse physisorbed alkoxide from the frustules. The chemisorbed alkoxide coating on the frustules was then rehydrolyzed by pumping 15 ml of an aqueous 1 M NH_4OH solution into the microfiltration unit. After 1 min of exposure, the hydrolyzing solution was removed by vacuum filtration and the frustules were dried for 5 min under vacuum aspiration at room temperature. This sequential exposure of the frustules to the tin alkoxide solution, the 2-propanol solution, and then the ammonium hydroxide solution was repeated 15 times. After the final coating cycle, the frustules were dried in air at 100^{o}C for 12 h. The frustules were then heated in air at 2^{o}C/min to 700^{o}C for 2 h to allow for conversion of the coating into crystalline SnO_2.

4.3 Results and Discussion

Initial attempts in applying surface sol-gel derived coatings of SnO_2 on diatom frustules employed frustules which had been washed in an HCl-methanol 1:1 solution for 1 h at room temperature. The frustules were then exposed to 15 surface sol-gel depositions with a 0.01 M Sn (IV) isopropoxide solution as outlined in Section 4.2.2. The frustules were then heat treated in air at 700^{o}C for 2 h. There was no observable

deposition of SnO_2 on the surface of the frustules as shown in Figure 4.1(a) which was confirmed by analyzing the entire frustule with EDS (Figure 4.1(b)) (Note: this was a representative sample). The inability to obtain continuous coatings on the frustules was attributed to a low density of surface hydroxyl groups which are necessary to initiate the sol-gel reaction on the frustule surfaces. Therefore, in an effort to increase the hydroxyl concentration on the frustules, a new batch of frustules was exposed to an RCA-1 solution (after washing in the HCl:methanol solution) at 65^{o}C for 0.5 h. It was expected that the oxidizing nature of the RCA-1 solution would promote the formation of silanol groups as reported by [9, 12]. The as-treated frustules were again exposed to the same surface sol-gel deposition and heat treatment conditions as outlined above. Observation of the as treated frustules revealed patchy SnO_2 coverage on the surface of the frustules as shown in Figure 4.1(c). The corresponding EDS analysis (Figure 4.1(d)) confirmed that the patchy spots observed in (c) were enriched in Sn. Such observations indicated that the frustules possessed a very low concentration of hydroxyl groups even after exposure to the RCA-1 solution.

To amplify the concentration of hydroxyl groups, a dendritic growth process of adding polyfunctional amine and acrylate layers on the silica frustules was employed, as outlined in the schematic illustration shown in Figure 4.2 (Note: this was a collaborative research effort headed by Dr. Guojie Wang and Matthew Dickerson at Gerogia Tech). To build the dendritic film layer, the diatom frustules were first subjected to the oxidizing RCA-1 cleaning solution and then reacted with 3-amino propyltrithoxy silane resulting in frustules functionalized with a limited number of amine groups. The amine groups were then reacted in an alternating fashion with excess polyfunctional solution of

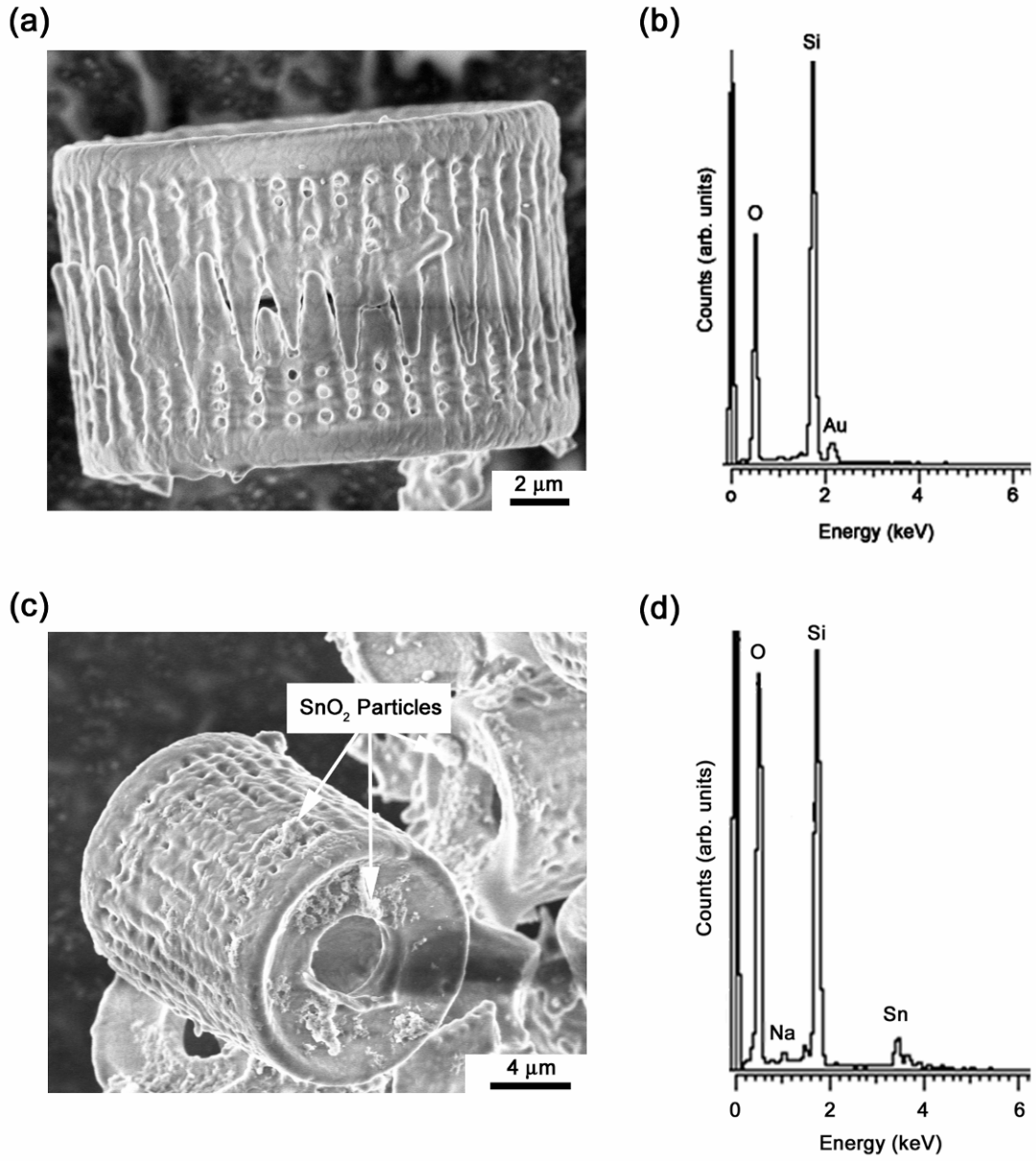

Figure 4.1: Surface sol-gel depositions on *Aulacoseira* frustules that were first treated with (a) 1:1 MeOH:HCl solution and (c) RCA-1 solution. EDS analysis revealed no Sn peaks for the frustules treated with the 1:1 MeOH:HCl solution (b) where as the nodules on the frustules in (c) were enriched in Sn. In both cases there was not enough OH groups on the surface to initiate film growth using the surface sol-gel process.

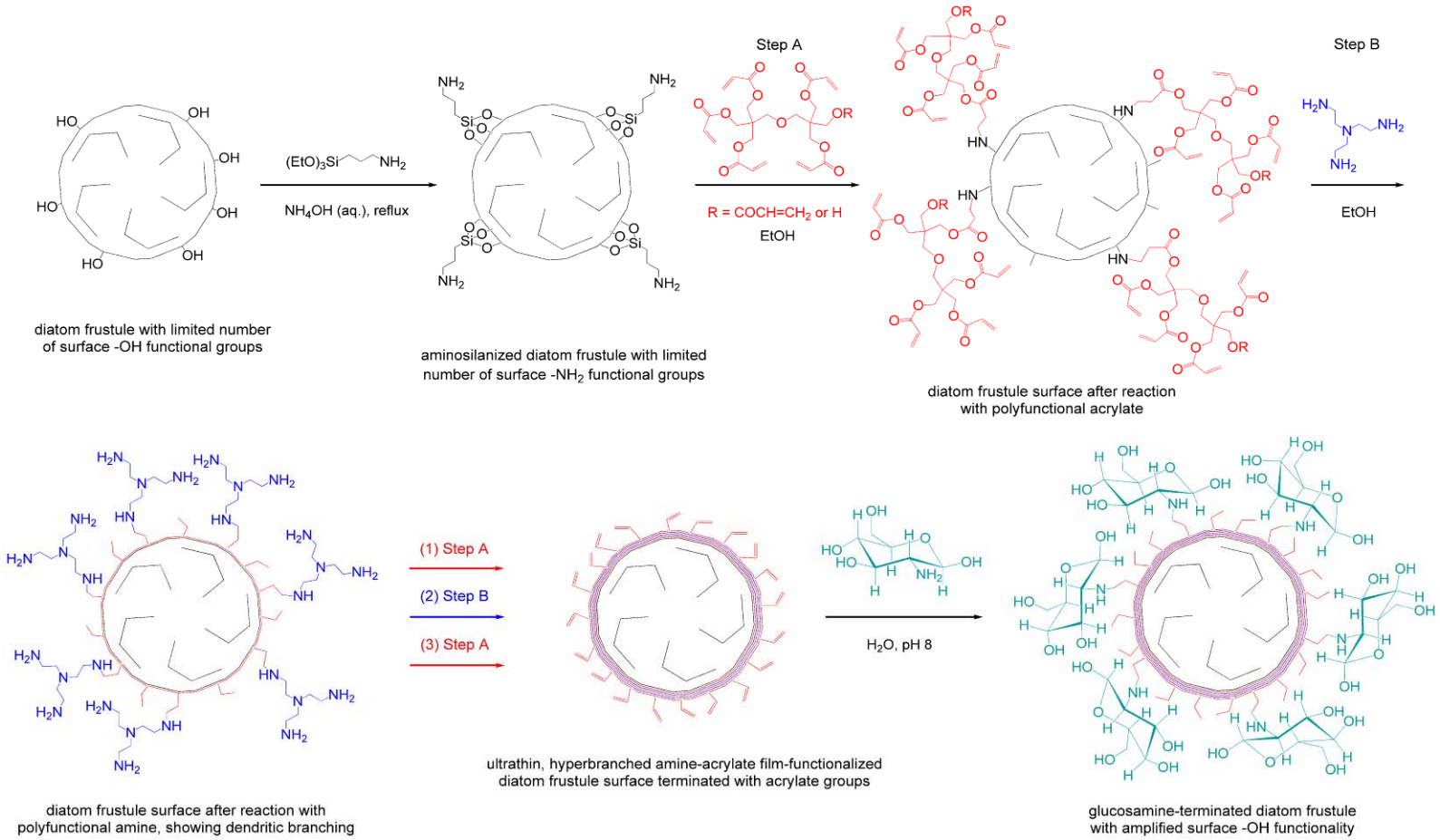

Figure 4.2: Schematic illustration of the growth of the hyperbranched amine-acrylate ultrathin film on diatom frustule surfaces followed by Michael addition of glucosamine to the third acrylate layer resulting in substantial amplification of the density of surface hydroxyl groups on the frustules.

dipentaerythritol penta-/hexa-acrylate and tris(2-aminoethyl)amine resulting in multi-amine-acrylate dendritic growth of an ultrathin organic layer which was covalently grafted to the frustule surface through Michael addition reaction. The frustules were subjected to a total of 3 exposures to the dipentaerythritol penta-/hexa-acrylate solution and 2 exposures to the tris(2-aminoethyl)amine solution which led to the rapid amplification of functional moieties. Final reaction of the acrylate-terminated film with glucosamine hydrochloride resulted in an amplification of the reactive hydroxyl groups on the frustules.

The density of the amines present after each layer was evaluated on glass slides using UV/Vis absorption spectroscopy by Dr. Guojie Wang (Georgia Institute of Technology). Fluorescein isothiocyanate (FITC) was utilized as a label for amine sites. Weak absorption was observed after reacting the amine sites with the acrylate monomer which indicated that the majority of the terminal amine functionalities were consumed by reaction with the monomer double bond. This analysis revealed that the functional groups reached a saturation level beyond the fourth acrylate layer.

The glucosamine-functionalized frustules were exposed to 15 surface sol-gel depositions with a 0.01 M Sn (IV) isopropoxide solution as outlined in Section 4.2.2. After the final coating cycle, the frustules were dried in air at 100^{o}C for 12 h. The frustules were then fired in air at 2^{o}C/min to 700^{o}C for 2 h to allow for conversion of the coating into crystalline SnO_2.

A secondary electron (SE) image of a starting silica-based *Aulacoseira* diatom frustule is shown in Figure 4.3(a). A SE image obtained from a functionalized and tin oxide-coated frustule (after the 2 h, 700^{o}C treatment) is shown in Figure 4.3(b). The

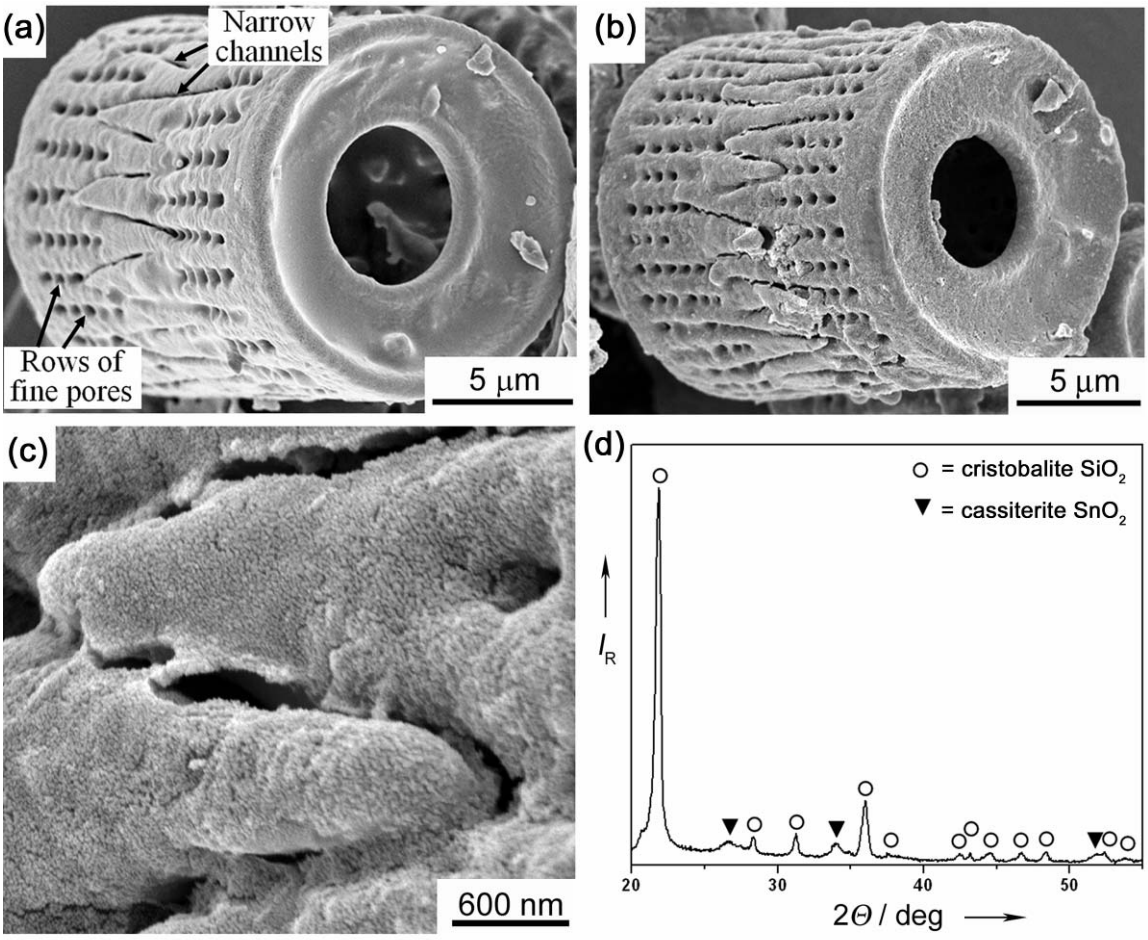

Figure 4.3: (a) SE image of the starting silica-based *Aulacoseira* diatom frustule. (b) SE image of the SnO_2-coated frustule after being subjected to the amine-acrylate dendritic buildup process and terminated with glucosamine followed by 15 surface sol-gel deposition cycles and heat treatment at 700°C for 2 h. (c) Higher-magnification SE image of the fingerlike region shown in (b). (d) XRD pattern of the SnO_2-coated frustules.

coated frustule retained the 3-D morphology and fine features (pores, channels) of the starting (uncoated) frustule. Higher magnification SE images (such as Figure 4.3(c)) revealed that the coated frustules possessed a more granular surface than for the starting frustules.

X-ray diffraction (XRD) analysis of the coated frustules (Figure 4.3(d)) yielded relatively intense diffraction peaks for the cristobalite polymorph of SiO_2, generated by the underlying frustule template, and modest peaks for SnO_2 (cassiterite), generated by the coating. Scherrer analysis (performed on the 100 % (110) peak) yielded an average SnO_2 crystallite size of 7.7 nm. The continuity and thickness of the tin oxide coating was analyzed by performing transmission electron microscopy on cross-sections of the coated frustules conducted by Dr. Ye Cai (Georgia Institute of Technology). Figure 4.4(a) reveals a continuous, thin, SnO_2 coating along the surface of the silica frustule. Higher magnification TEM images Figures 4.4(b) and (c) revealed that the coating was continuous, polycrystalline, and 50 nm thick. The size of the SnO_2 crystallites was measured to be ~ 8 nm in diameter from Figure 4.4(c). Selected area electron diffraction (SAED) analysis (Figure 4.4(d)) of the coating yielded diffraction patterns from the (110), (101), (211), and (112) planes of cassiterite SnO_2.

A microscale SnO_2 sensor (Figure 4.5(a)) was fabricated to further assess the continuity of the SnO_2 coating on the surface of the frustules. The sensor was made by sprinkling some of the SnO_2-coated frustules between two gold electrodes on a Si_3N_4 substrate. The rim on each end of the frustule was then welded to the Si_3N_4 substrate with Pt using a focused ion beam (FIB). The Pt electrodes were then deposited from the frustule to the gold electrodes to connect the conduction pathway. The as-prepared SnO_2-

coated frustule sensor was then tested for NO(g) sensing behavior at 350^{o}C. A bias voltage (0.5V DC) was applied across the electroded SnO_2 frustule replica, and the change in current was evaluated upon exposure to flowing NO(g) in an Ar(g) carrier stream (Figure 4.5(b)). Exposure to 3, 5, or 8 ppm NO(g) resulted in proportional increases in the current passing through the SnO_2-coatd frustule. The response (rise) and recovery (decay) times, defined as the time needed to reach 90% of the total signal change, was 12 s and 32 s respectively. These times are comparable to or faster than, those reported for other nanocrystalline SnO_2 sensors [13, 17].

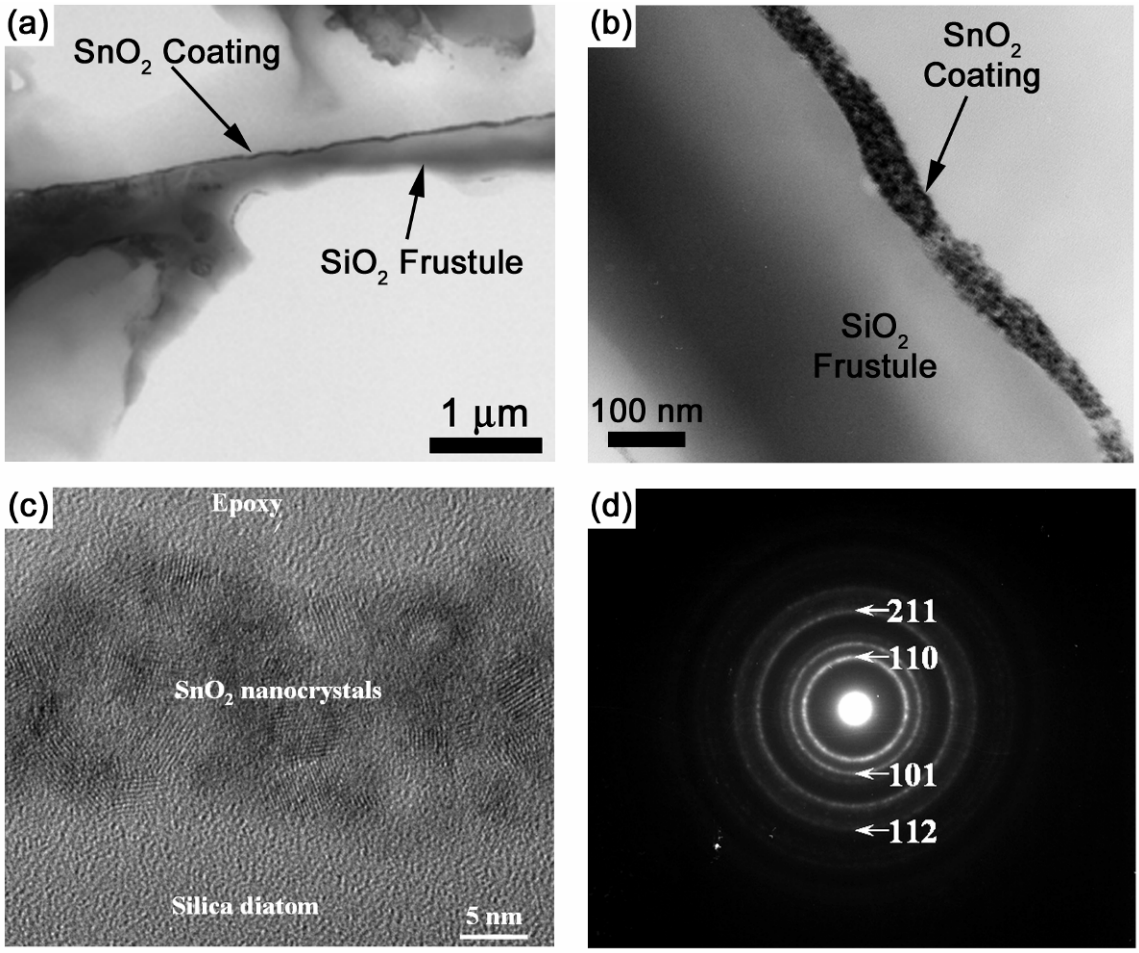

Figure 4.4: (a) and (b) are low and high magnification TEM images of a cross-section of a frustule possessing a thin (50 nm) SnO_2 coating. (c) High resolution TE image of the polycrystalline SnO_2 coating on the silica frustule. (d) SAED pattern of the SnO_2 coating on the frustule shown in (b).

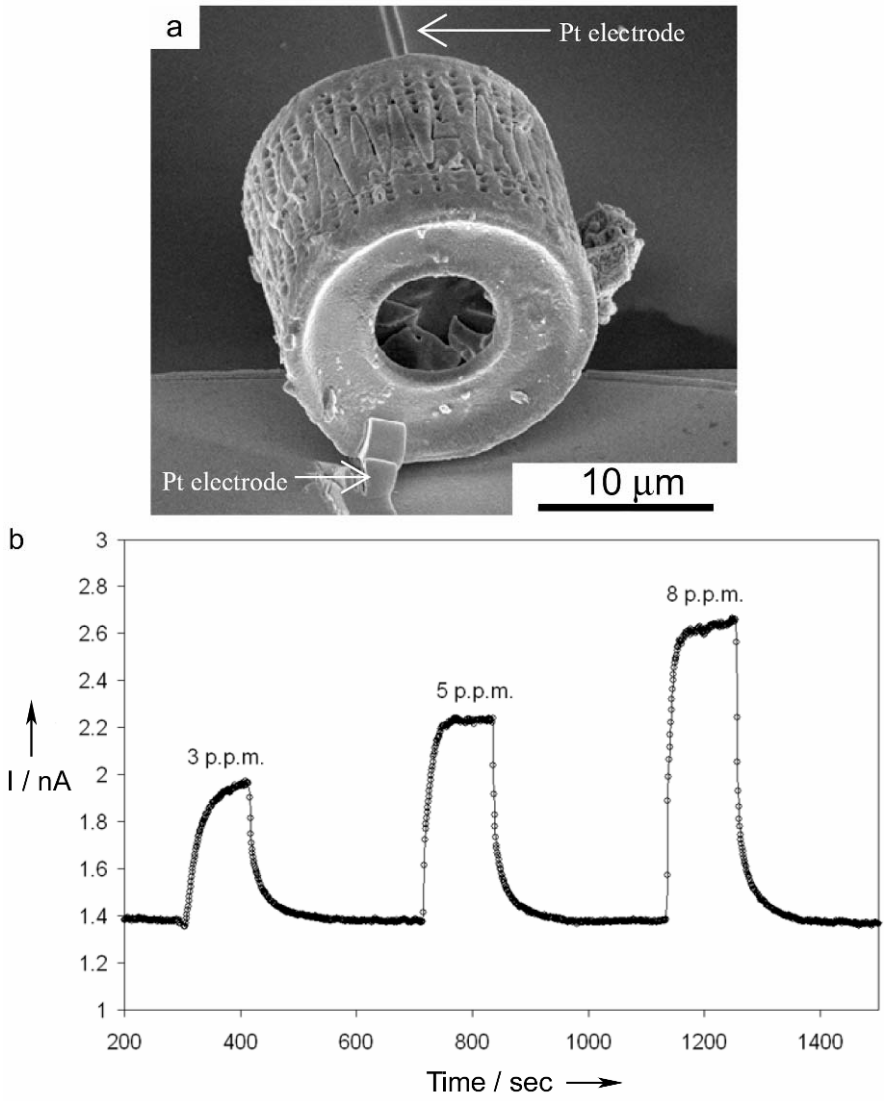

Figure 4.5: Utilization of a SnO_2-coated frustule as a NO(g) sensor. (a) SE image of the SnO_2-coated frustule attached to two platinum electrodes and (b) the observed response from the coated frustule upon exposure to NO(g).

4.4 Summary and Outlook

The work presented in this Chapter demonstrates a rather facile approach for functionalizing surfaces with reactive hydroxyl groups for surface sol-gel processing. An organic hyperbranched amine-acrylate coating was developed which built off of the limited number of native silica OH groups to amplify the hydroxyl concentration (by terminating the acrylate layer with glucosamine) on the surface of the frustules. It was shown that surface sol-gel reactions were initiated on the frustules that possessed an amplified concentration of hydroxyl groups provided by this hyperbranched method. On the other hand, coatings were not initiated on the native silica frustules and frustules that were treated with an oxidizing RCA-1 solution. The continuity of the coating that was obtained on the hydroxyl rich frustules was assessed with transmission electron microscopy and electrochemical (gas-sensing) analyses.

The work presented in this Chapter provides an effective approach for obtaining reactive functionalities on the surface of nanostructured templates. It should be noted that other nucleophilic alcohols such as, mercaptoethanol or tris-(hydroxymethyl)-aminomethane could also react with the actylate monomer, however, the glucosamine provides more OH groups per reaction with the acrylate.

4.5 References

[1] Z. Bao, M. R. Weatherspoon, S. Shian, Y. Cai, P. D. Graham, S. M. Allan, G. Ahmad, M. D. Dickerson, B. C. Church, Z. Kang, H. W. Abernathy III, C. J. Summers, M. Liu, K. H. Sandhage, *Nature*, **446,** 172-175 (2007).

[2] K. H. Sandhage, M. B. Dickerson, P. M. Huseman, M. A. Carana, J. D. Clifton, T. A. Bull, T. J. Heible, W. R. Overton, M. E. A. Schoenwaelder, *Advanced Materials*, **14**, 429 (2002).

[3] D. Losic, G. Triani, P. J. Evans, A.Antanacio, J. G. Mitchell, N. H. Voelcker, *Journal of Materials Chemistry*, **16**, 4028-4034 (2006).

[4] I. Ichinose, H. Senzu, T. Kunitake, *Chemistry Letters*, 831-832 (1996).

[5] S. Fujikawa, T. Kunitake, *International Journal of Nanoscience*, **1**, 617-620 (2002).

[6] S. Fujikawa, T. Kunitake, *Langmir*, **19**, 6545-6552 (2003).

[7] J. Huang, T. Kunitake, *Journal of the American Chemical Society*, **125**, 11834-11835 (2003).

[8] J. Huang, T. Kunitake, S. Onoue, *Chemmical Communications*, 1008-1009 (2004).

[9] Y. Aoki, T. Kunitake, A. Nakao, *Chemistry of Materials*, **17**, 450-458 (2005).

[10] I. Ichinose, H. Senzu, T. Kunitake, *Chemistry of Materials*, **9**, 1296-1298 (1997).

[11] I. Ichinose, T. Kawakami, T. Kunitake, *Advanced Materials*, **10**, 535-539 (1998).

[12] Y. Aoki, T. Kunitake, *Advanced Materials*, **16**, 118-122 (2004).

[13] G. Sberveglieri, S. Groppelli, P. Nelli, *Sensors and Actuators B*, **4**, 457-461 (1991).

[14] Y. Shimizu, N. Nakashima, T. Hyodo, M. Egashira, *Journal of Electroceramics*, **6**, 209-217 (2001).

[15] A. T.-Silver, A. S-Juárez, *Materials Science and Engineering B*, **110**, 268-271 (2004).

[16] M. Law, H. Kind, B. Messer, F. Kim, P. Yang, *Angewandte Chemie International Edition*, **41**, 2405-2408 (2002).

[17] T. Hyodo, K.Sasahara, Y. Shimizu, M. Egashira, *Sensors and Actuators B*, **106**, 580-590 (2005).

[18] I. Sayago, J. Gutiérrez, L. Arés, J. I. Robla, M. C. Horrillo, J. Getino, J. Rino, J. A. Agapito, *Sensors and Actuators B*, **26-27**, 19-23 (1995).

[19] Y. Liu, E. Koep, M. Liu, *Chemistry of Materials*, **17**, 3997-4000 (2005).

[20] R. W. J. Scott, S. M. Yang, G. Chabanis, N. Coombs, D. E. Williams, G. A. Ozin, *Advanced Materials*, **13**, 1468-1472 (2001).

CHAPTER 5: SURFACE SOL-GEL SYNTHESIS OF RUTILE TITANIA COATINGS ON *MORPHO* BUTTERFLY WING SCALES

5.1 Introduction

Up to this point in this thesis, the issues of applying alkoxide-derived coatings on Nature's nanostructured inorganic ceramic templates have been discussed. Two methods for applying these coatings have been demonstrated with the automated surface sol-gel process proving to be the superior deposition technique for controlled film formation. In this Chapter, the possibility of utilizing the automated surface sol-gel system as a tool for depositing high refractive index materials (i.e., rutile TiO_2) on nanoengineered natural 3-D organic templates (i.e., butterfly wings) is explained.

Nature, provides spectacular examples of periodic organic substrates which possess the ability to manipulate the flow of light. These structures are often fabricated using chitin, which is a polysaccharide that is structurally similar to cellulose (e.g., both possess many OH groups). Chitin forms the structural exoskeletons of many insects and crustaceans, such as butterflies, beetles, lobsters, crabs, and shrimp. Although Yablonovich [1] and John [2] are credited for conceptualizing and demonstrating the idea of obtaining a photonic band gap using periodic dielectric composites (photonic crystals) some two decades ago, Nature has exploited this idea for millions of decades [3]. For example, the wing scales of *Lepidoptera* butterflies and the scales of some weevils exhibit highly ordered three-dimensional photonic crystal structures which result in brilliant reflectance due to Bragg diffraction [3-4]. This phenomenon (coloration due to Bragg diffraction) is strictly a result of the periodic arrangement of alternating layers of high (chitin) and low (air) refractive index material and is therefore termed "structural

color" [5-7]. One of the advantages of structural versus pigmentary coloration is that structural colors are more intense. In fact, it has been reported that male *Morpho* butterflies can be observed from up to a quarter mile away [3]. Thus, Nature has magnificently nanoengineered and endowed some biological structures with periodic nanopore structures that may be good candidate template materials for enhancing catalysis, gas sensing, or photonic crystal applications.

In 2001, Yablonovitch acknowledged several examples in Nature (e.g., opal, butterfly, sea mouse) which possessed photonic band gap structures [8]. However, he speculated that such structures do not possess a full bandgap "perhaps because it requires too much refractive-index contrast" [8]. In the recent past, researchers have sought to replicate the periodic structure of butterfly wing scales with inorganic coatings using atomic layer deposition (ALD), chemical vapor deposition (CVD), sol-gel, and immersion in salt solutions [9-11]. However, the coatings which have been applied possess similar refractive indices to that of chitin (n = 1.58 for chitin) [12]. For example, Huang *et al*. controllably applied 10, 20, 30, and 40 nm thick coatings of Al_2O_3 (n = 1.76) [13] on *Morpho* butterfly scales using ALD. They reported a red shift in the diffracted peak due to a change in the periodicity of the nanopore structure as a result of the deposited coating and a subsequent blue shift after inversion (i.e., pyrolysis of the chitin template) [9]. Cook *et al*. applied a 100 - 150 nm thick SiO_2 (n = 1.48) [14] coating on *Peacock* butterfly wing scales using CVD processing [10]. They also tried dip coating the butterfly wings into a sol-gel precursor and reported that nonohomogeneous coatings were obtained due to dewetting between the wing and the inorganic coating which catastrophically cracked during the annealing process [10]. Zhang *et al.* submersed the

wings of a *Thaumantis diores* butterfly into an ethanolic solution of $Zn(NO_3)_2$ for 12 h to obtain ZnO (n = 2.01) [15] replicas after calcination at 500°C for 2 h [11].

Many researchers have cited rutile titania (TiO_2) as the gold standard for coating periodic photonic crystal structures to achieve enhanced photonic band gap properties in the visible light region [16]. Besides the periodic orientation of the photonic crystal structure, another critical requirement for obtaining photonic band gap properties is that the refractive index ratio between the solid structure and the air in the pores should be high, while the optical absorption of the structure should be as low as possible [17]. Rutile TiO_2 is a transparent metal oxide which possesses a high refractive index (n = 2.90 at λ = 400 nm) [18] and an optical absorption loss which is much lower than that of silicon [16]. However, TiO_2 consists of two common metastable polymorphs (anatase and brookite) and one stable polymorph (rutile). Complete transformation of anatase and brookite to rutile usually occurs at temperatures in excess of 900°C [19, 20]. Consequently, this transformation results in significant grain growth which has a detrimental affect on the periodicity and optical scattering of titania-based photonic crystals. Indeed, many researchers have reported a loss in the periodicity and band gap properties of titania-coated photonic crystal structures after annealing at 900°C to obtain rutile titania [17, 21-26]. The high crystallization temperature required to obtain rutile TiO_2 is also not well suited for coatings which are applied on biological or lithographically patterned polymeric photonic crystal structures.

A review of the literature has revealed several chemical/structural methods for obtaining rutile TiO_2 at much lower annealing temperatures than the standard 900°C treatment [27-30]. These methods have also been shown to help control the final grain

size so as to yield nanosized rutile TiO_2 grains. One of the methods, which will be discussed in this Chapter, is to simply dope the TiO_2 with a structurally similar material which will act as heterogeneous nucleation cite for the low-temperature nucleation and growth of rutile TiO_2. Tin oxide has been shown by several authors to promote the nucleation and growth of rutile TiO_2 at temperatures as low as 40°C [27]. Tin oxide (cassiterite) forms only one stable phase, rutile [28]. The lattice parameters of rutile SnO_2 (a = 0.4738 nm and c = 0.3187 nm) are similar to the lattice parameters of rutile TiO_2 (a = 0.4593 nm and c = 0.2959 nm) and, hence, SnO_2 can provide an attractive surface for heterogeneous nucleation and growth of rutile TiO_2.

The TiO_2-SnO_2 binary phase diagram reveals that TiO_2 can be doped with as much as 10 mol% SnO_2 in a solid solution before phase separation via spinodal decomposition occurs [31]. However, Kumar *et al*. have reported that doping titanium isopropoxide with 19 mol% $SnCl_4$, followed by refluxing at 80°C for 12 – 16 h at a solution pH of 2, resulted in the formation of rutile titania without phase separation after drying the precipitates at 40°C for 8 h [27]. On the other hand, Nair *et al*. have demonstrated that coprecipitating aqueous sols of anatase titania (particle size = 10 nm) doped with 2.4 mol% of tin oxide (particle size = 3 nm) yields mixed anatase and rutile powder phases which require heat treatment at 800°C for 8 h to achieve complete conversion of the anatase to rutile [32]. In both studies, TiO_2 (anatase and rutile) were the only detectable phases present (i.e., cassiterite tin oxide was not detected) when the powders were analyzed using XRD. Therefore, there must be an optimal tin oxide doping concentration, that lies between 19 and 2.4 mol%, which will provide enough rutile nuclei to suppress the formation of anatase and thereby allow for complete

conversion to rutile TiO_2. Determination of this optimum doping concentration using alkoxide precursors is a portion of the study presented in this Chapter. Controlled doping is one of the advantages of using alkoxide precursors over other deposition techniques to obtain coatings with desired compositions. Furthermore, the coupling of surface sol-gel processing with controlled doping of alkoxide precursors (either within each layer or with sequential SnO_2 and TiO_2 layers) offers a facile layer-by-layer approach for controllably coating nanostructured templates.

In this Chapter, the wing scales of a blue *Morpho* butterfly are utilized as templates owing to their structure related optical properties. The goal is to faithfully replicate these structures with rutile TiO_2 coatings using the automated surface sol-gel system as a layer-by-layer deposition tool to couple the desirable periodic architectures provided by the scales with a higher refractive index material (i.e., rutile) to achieve enhanced photonic band gap properties.

5.2 Experimental Procedure

5.2.1 Materials

The Ti (IV) isopropoxide (99.995%, metals basis) precursor was obtained from Alfa Aesar (Ward Hill, MA) and the Sn (IV) isopropoxide (10% w/v, 98% metals) and anhydrous 2-propanol were purchased from Chemat Technology, Inc. (Northridge, CA). Pure DI water (resistivity of 18.2 MΩ·cm, from a NANOpure Diamond UV/UF system, Barnstead International) was used in all cases to hydrolyze the precursors. Fritted glass filtration funnels (Type E, 4-8 μm pore size) were purchased from Ace Glass (Vineland, NJ) and were used without chemical surface modification. The blue Morpho butterfly was obtained form Professor Mohan Srinivasarao (Georgia Institute of Technology).

5.2.2 Preparation and Hydrolyzation of the Titanium and Tin Alkoxide Precursors

Common Ti (IV) isopropoxide solutions doped with varying amounts of Sn (IV) isopropoxide were prepared inside of a controlled atmosphere dry nitrogen glove-box (discussed in Section 2.3 of this thesis). The molarity of the Ti (IV) isopropoxide was fixed at 0.1 M while the relative concentration of the Sn (IV) isopropoxide dopant varied incrementally (by 1 M increments) between 1 and 10 mol%. To obtain Sn (IV) isopropoxide-doped Ti (IV) isopropoxide common solutions, the Sn (IV) isopropoxide was first added to the anhydrous 2-propanol solvent, under magnetic stirring, followed by introduction of the Ti (IV) isopropoxide. The common solutions were clear and stable over long periods of time (i.e., the solutions do not become cloudy and are stable against self precipitation). Although the common solutions are stable, fresh solutions were prepared for each experiment due to a lack of storage space inside of the glove box.

Cohydrolysis of the common alkoxide precursor solutions was performed outside of the glove box under atmospheric conditions using plastic 15 mL conicle tubes. The common alkoxide solutions were hydrolyzed by adding 50 μL of DI water to a 10 mL volume of the alkoxide solution. White gelatinous precipitates instantaneously precipitated upon inoculation of the water. The solutions were allowed to sit on the bench top for 5 min resulting in the formation of a viscous gel like solution. The solutions were then centrifuged at 9000 rpm for 10 min to separate the supernatant from the gel. This process was repeated two more times (making a total of 3 hydrolyzation steps without removing the supernatant from the conicle tubes) to ensure complete hydrolysis of any remaining alkoxide species which may have been present in the supernatant. It was noted that addition of water after the first hydrolyzation step did not

result in the formation of a cloudy precipitate in the clear supernatant, which indicated that the alkoxide had completely hydrolyzed with the first hydrolyzation treatment. After the third hydrolyzation treatment, the supernatant was decanted from the 15 mL conicle and the remaining gel was dried inside a drying oven at 80^{o}C for two days to completely remove any remaining solvent. After drying, the gel layer turned a slightly yellowish color. The dried gel was ground with a mortar and pestle to prepare powder samples for the high temperature X-ray diffraction (HTXRD) studies.

Pure solutions of 0.1 M Ti (IV) isopropoxide and Sn (IV) isopropoxide were also prepared in anhydrous 2-propanol and hydrolyzed using the above method as control experiments.

5.2.3 Materials Characterization

5.2.3.1 HTXRD Analyses of the Titanium and Tin Alkoxide Precipitates

High temperature X-ray diffraction (HTXRD) analyses were performed on the precipitates produced from hydrolyzing the pure and doped tin/titanium isopropoxide solutions using an X-pert Pro MPD diffractometer (PANalytical Corp., Almelo, the Netherlands) with the use of an HTK2000 furnace (Anton-Paar, Gmbh, Graz, Austria). The diffractometer used a vertical theta-theta goniometer, 0.5^{o} divergence slits, and a solid-state detector (Xcelerator, PANalytical). The temperature of the furnace was calibrated using standard reference materials (SRM 759, NIST, Gaithersburg, MD). HTXRD analyses, performed with the help of Dr. Michael S. Haluska (Georgia Institute of Technology), were conducted in air with a constant heating rate of 10^{o}C/min. X-rays were collected at the start of the experiment (i.e., at 25^{o}C) and then in 50^{o}C temperature

increments starting at 300^{o}C up to 850^{o}C for the tin-doped titania and pure tin isopropoxide precipitates and up to 1000^{o}C for the pure Ti isopropoxide precipitates.

5.2.3.2 Morphological and Phase Analyses of the Blue Morpho Scales

The morphological and phase analyses were performed on the coated butterfly scales using scanning electron microscopy (SEM) and transmission electron microscopy (TEM). The morphology of the blue *Morpho* butterfly scales was evaluated with a field emission scanning electron microscope (1530 SEM, LEO/Zeiss Electron Microsopy, Gmbh, Thornwood, NY) equipped with energy-dispersive X-ray analysis capability. Transition electron microscopy and electron diffraction, performed by Dr. Ye Cai (Georgia Institute of Technology), was conducted using a JEOL 4000 EX (Japan Electron Optics Laboratory, Tachikawa, Tokyo) for evaluating the structure and phase content of the coatings applied on the coated scales.

5.2.4 Automated Surface Sol-gel Processing of the Titania-Based Coatings on the Blue *Morpho* Butterfly Wing Scales

Surface sol-gel depositions were performed on the blue *Morpho* butterfly wings using the automated surface sol-gel setup described in Section 2.3. A small portion of the butterfly wing was fastened to a glass slide using a brass alligator clip and positioned at a 60^{o} angle inside of a 20 mL filtration flask as shown in Figure 5.1. The Tygon tubing leading from the precursor, solvent, and water solutions was then positioned so that the solution would drip down and flow over the wing specimen.

Depositions were performed by pumping 5 mL of precursor solution into the filtration flask which completely immersed the wing sample. After a predetermined chemisorption reaction time (10 min), the solution was then evacuated under vacuum

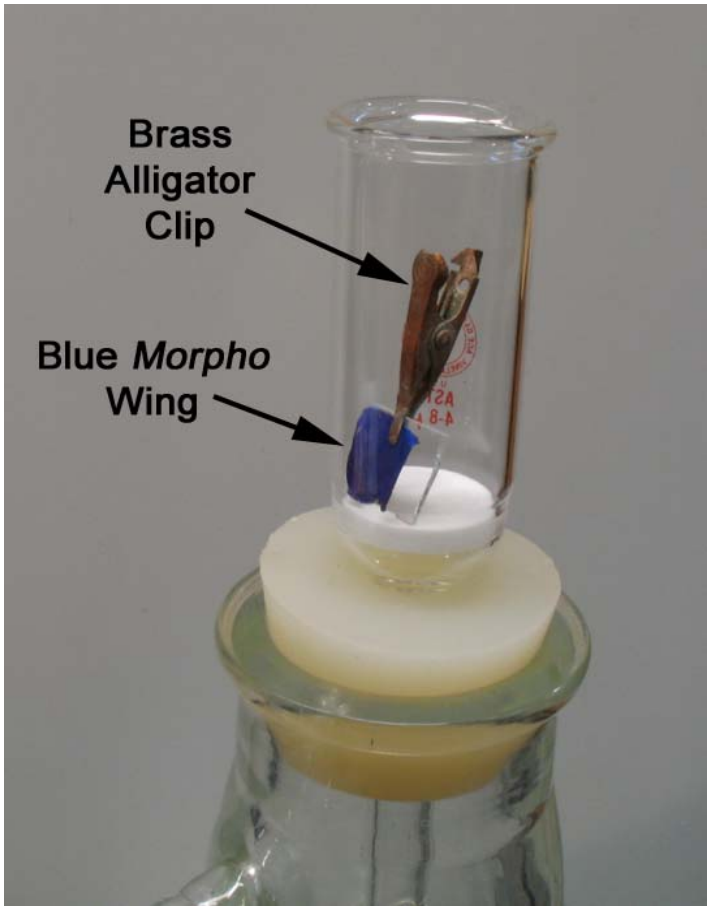

Figure 5.1: Photograph revealing a blue Morpho butterfly wing specimen immobilized on a glass slide using a brass alligator clip to prevent the specimen from floating around in the solution.

filtration. While still under vacuum, 5 mL of anhydrous 2-propanol was pumped into the flask (completely immersing the sample) three separate times to rinse away any physisorbed alkoxide. The vacuum pump was then turned off and 5 mL of water was pumped into the system which also completely immersed the sample. After a 1 min incubation time the water solution was removed via vacuum filtration. The wing specimen was again rinsed three more times with 2-propanol to help rinse away any remaining water. The samples were then dried by aspirating hot air from a blow dryer past the samples while the system was still under vacuum. Samples were collected for heat treatment after 20 and 40 deposition cycles.

After the depositions were completed, the tin-doped titania-coated butterfly wings were collected and heat treated at 450^{o}C for 4 h. The ramp rate of the furnace was set at 0.5^{o}C/min in an effort to minimize curling of the scales. The non-doped scales were heat treated at two different peak temperatures, one at 450^{o}C under the same conditions described above, and the other at 900^{o}C. The sample heat treated at 900^{o}C was first annealed at 450^{o}C for 4 h (ramp = 0.5^{o}C/min) and then the temperature was increased at 3^{o}C/min up to 900^{o}C and held for 1 h. The samples were heat treated inside of a magnesia crucible.

5.3 Results and Discussion

5.3.1 HTXRD Analyses of the Precipitates Obtained by Hydrolyzing the Pure and Doped Tin and Titanium Alkoxide Solutions

Uniform film growth using the surface sol-gel process requires nonaqueous hydrolysis upon neucleophilic reaction between the surface OH groups and the precursor. Thus, doping with an aqueous solution of $SnCl_4$ is not an option, as this would result in

the formation of oligomers in the precursor stock solution. Therefore, Sn (IV) isopropoxide was selected as the rutile facilitating dopant. To determine the optimum doping concentration of the Sn (IV) isopropoxide, solutions of 0.1 M Ti (IV) isopropoxide doped with 1 - 10 mol% Sn (IV) isopropoxide were prepared and precipitated as discussed in Section 5.2.2. Pure solutions of 0.1 M Ti (IV) and Sn (IV) isopropoxide were also prepared as controls for comparison.

A series of high-temperature X-ray diffraction patterns obtained during heating the precipitates obtained from the 0.1 M Ti (IV) isopropoxide solution from 400^{o}C to 1000^{o}C at a rate of 10^{o}C/min in air is shown in Figure 5.2. The thermal energy provided was sufficient to nucleate anatase at 400^{o}C which is consistent with other reports in the literature [33]. All of the preceding diffraction patterns (i.e., diffraction patterns obtained at room temperature at the beginning of the experiment and then from 300^{o}C up to 400^{o}C) yielded amorphous diffraction humps. At 650^{o}C, rutile TiO_2 nucleated and continued to grow at the expense of the anatase phase as demonstrated by the increasing intensity of the (110) rutile peak (at $2\theta = 27.45^{o}$) and decreasing (101) anatase peak (at $2\theta = 25.28^{o}$). At 900^{o}C, all of the anatase was fully converted into rutile TiO_2. The average crystallite size, evaluated from XRD peak broadening of the (101) 100% rutile titania peak, using the Scherrer equation, was 113 nm [34].

Figure 5.3 shows the series of HTXRD patterns obtained from heating the precipitates of the 0.1 M Sn (IV) isopropoxide solution (heating rate = 10^{o}C/min). All of the peaks correspond with rutile SnO_2 (cassiterite). The cassiterite phase forms at 300^{o}C which is 100^{o}C below that of the titanium precipitates. The nucleation of cassiterite at lower temperatures should therefore provide stable rutile nucleation sites, in the tin

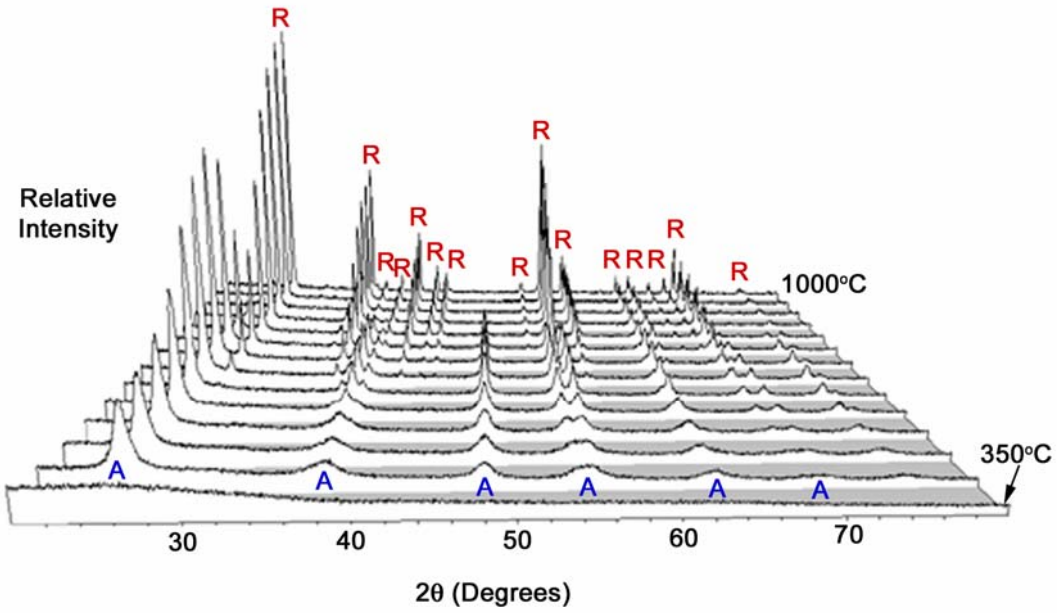

Figure 5.2: HTXRD analyses performed in air at a constant heating rate of 10°C/min on the powder precipitates obtained by hydrolyzing 10 ml of a 0.1 M Ti (IV) isopropoxide solution with 150 µL of water. (R = rutile TiO_2 and A = anatase TiO_2)

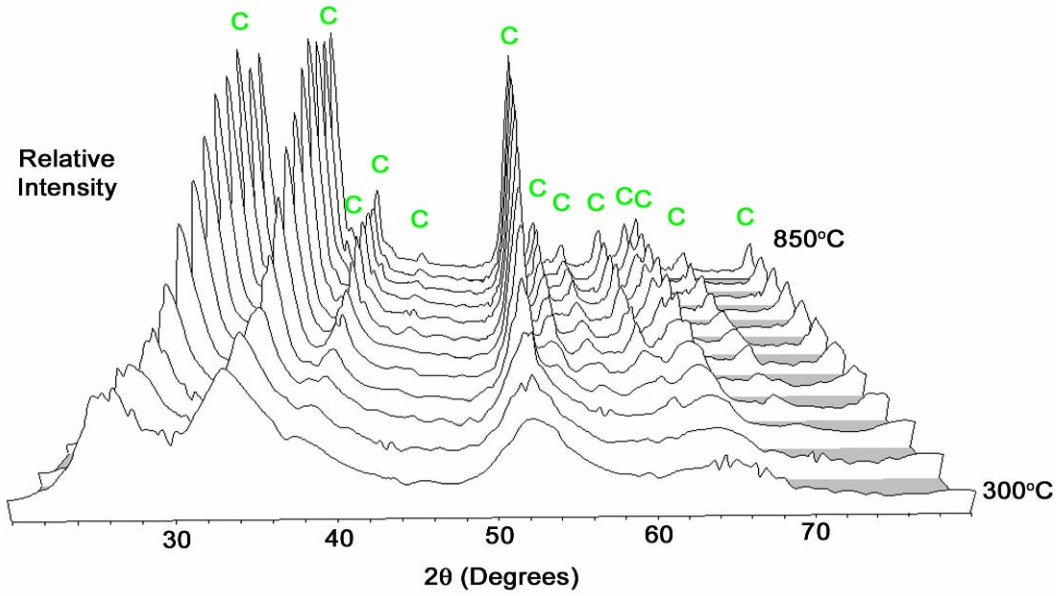

Figure 5.3: HTXRD analyses performed in air at a constant heating rate of 10°C/min on the powder precipitates obtained by hydrolyzing 10 ml of a 0.1 M Sn (IV) isopropoxide solution with 150 µL of water. (C = cassiterite SnO_2)

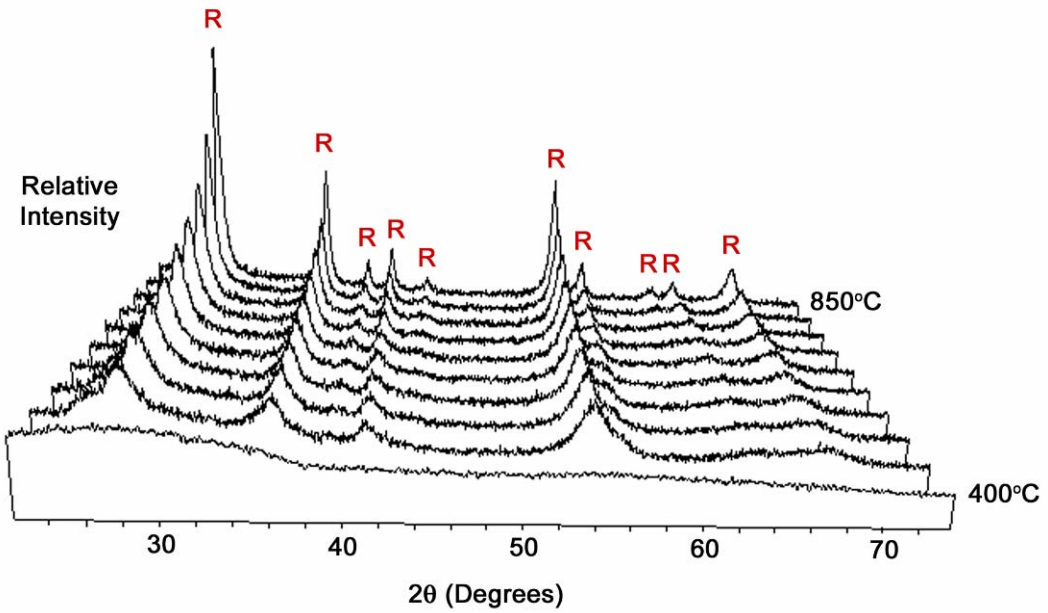

Figure 5.4: HTXRD analyses performed in air at a constant heating rate of 10°C/min on the powder precipitates obtained by hydrolyzing 10 ml of a 0.1 M Ti (IV) isopropoxide solution doped with 10 mol% Sn (IV) isopropoxide with 150 μL of water. (R = rutile TiO_2)

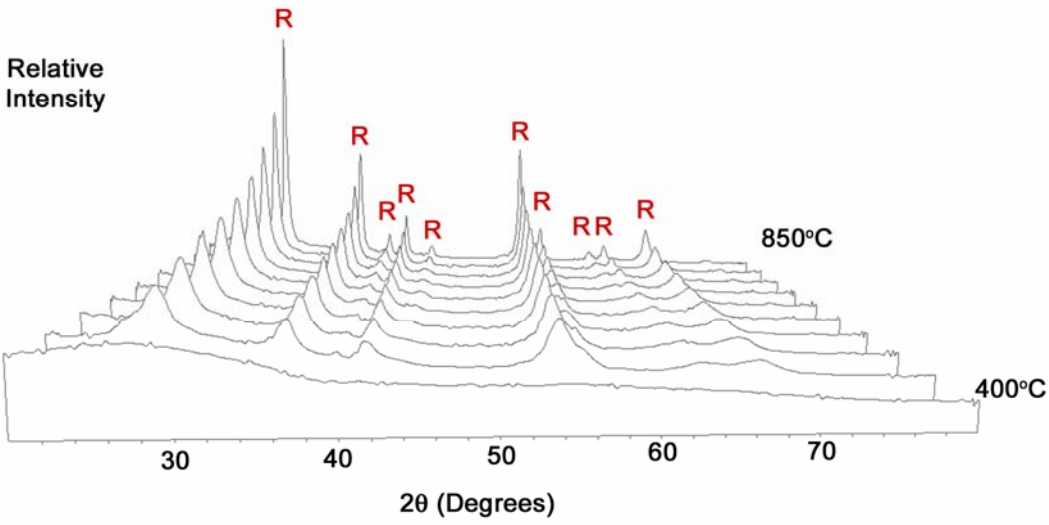

Figure 5.5: HTXRD analyses performed in air at a constant heating rate of 10°C/min on the powder precipitates obtained by hydrolyzing 10 ml of a 0.1 M Ti (IV) isopropoxide solution doped with 7 mol% Sn (IV) isopropoxide with 150 μL of water. (R = rutile TiO_2)

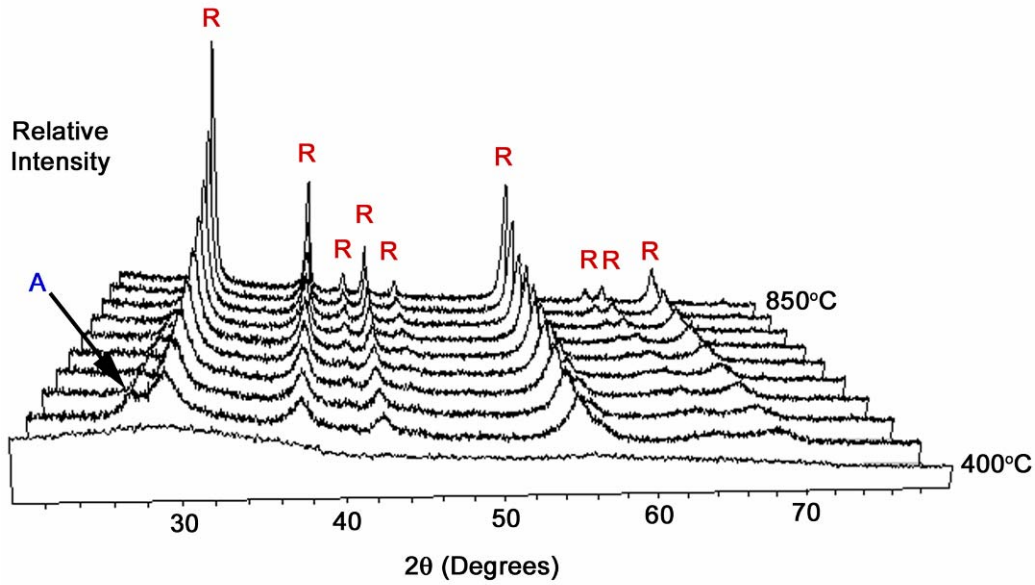

Figure 5.6: HTXRD analyses performed in air at a constant heating rate of 10°C/min on the powder precipitates obtained by hydrolyzing 10 ml of a 0.1 M Ti (IV) isopropoxide solution doped with 6 mol% Sn (IV) isopropoxide with 150 μL of water. (R = rutile TiO_2 and A = anatase TiO_2)

oxide-doped titania system, for the heterogeneous nucleation and epitaxial growth of rutile titania.

Figures 5.4 and 5.5 show the series of HTXRD patterns obtained from heating the precipitates of the 0.1 M Ti (IV) isopropoxide solutions doped with 10 and 7 mol% Sn (IV) isopropoxide respectively. Complete conversion of rutile TiO_2 was observed at 450°C for solutions doped with 10 mol% SnO_2 (Figure 5.4). This transformation required slightly more thermal activation than what was required to nucleate anatase TiO_2 (compare with Figure 5.2). Scherrer analysis revealed an average crystallite size of 15 nm for the rutile grains obtained at 450°C and 33 nm after the 850°C treatment. Complete conversion to rutile was also observed at 450°C for solutions doped with as

little as 7 mol% SnO_2 (Figure 5.5). However, solutions doped with less than 7 mol% SnO_2 yields mixed powders of both anatase and rutile phases as shown in Figure 5.6 which corresponds to a SnO_2 doping concentration of 6 mol%. Complete conversion to rutile titania did not occur until 750^oC for this system.

5.3.2 Scale Architecture of the Blue *Morpho* Butterfly

A photograph of the blue *Morpho* butterfly used in this work is shown in Figure 5.7(a). The iridescent nature of the wings can be observed by rotating the butterfly, thus changing the incident angle of the light source on the wings, which allows the observer to see blue, green, and purple reflections off the scales. Figure 5.7(b) shows a higher magnification optical microscope image taken from the blue side of the wing which reveals that the wing is decorated with tiny iridescent scales arranged like overlapping tiles on a roof. This image clearly demonstrates the uniform coloration of each of the scales which lie flat against the wing. One of the truly fascinating qualities of the blue *Morpho* is its ability to blend into its surroundings by simply closing its wings and thereby "morphing" into a dull brown color as shown in Figure 5.7(c). Figure 5.7(d) shows a higher magnification optical microscope image taken from the brown side of the Morpho wing. This image shows the same tile-like arrangement of tiny scales but these scales are pointed as opposed to the rounded scales on the blue side of the wing. These scales exhibited no apparent iridescence.

Figure 5.8(a-1) shows a low magnification SEM image of the blue round tipped scales. Each scale was 190 ± 10 μm long by 90 ± 8 μm wide. A higher magnification SEM image (Figure 5.8(a-2)) reveals that the scales were composed of thin parallel chitin laminae (~ 100 nm dia.) spaced ~600 nm apart. Each laminae is composed of several

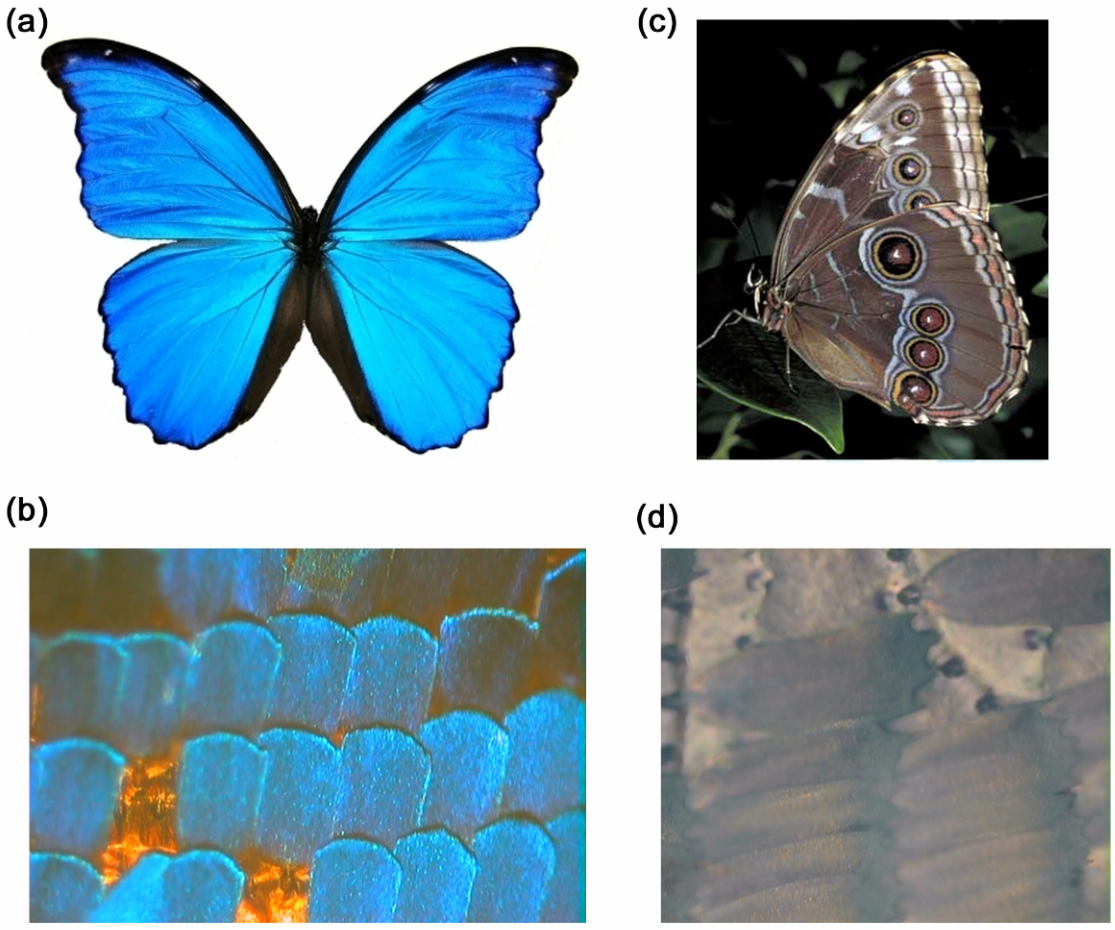

Figure 5.7: Photographs of a blue *Morpho* butterfly possessing blue iridescent properties on one side of the wings (a) (reproduced with permission) [35] comprised of tiny, round-tipped iridescent overlapping scales (b) and brown camouflage properties on the other side of the wings (c) (reproduced with permission, © Larry Kimball & Barbara Magnuson) [36] comprised of overlapping scales possessing pointed tips (d).

cylindrical rib-like structures which are spaced 100 nm apart by box-like (100 nm x 118 nm) supports which connect a lower rib to an upper rib as shown in Figure 5.8(a-3).

Figure 5.8(b-1) is a low magnification SEM image of the pointed scales from the brown side of the *Morpho* butterfly wing. Each scale is 200 ± 24 μm long by 70 ± 13 μm wide. Figure 5.8(b-2) reveals the porous architecture of the brown scales. These scales also possess parallel chitin laminae, spaced 2.2 μm apart. This porous framework is elevated about 900 nm off of a wavy underlying supportive structure by chitin trusses. For a 3-D schematic illustration of this structure see reference [5]. Each laminae are finely decorated with rows of cylindrical ridges (47 nm dia.) which are spaced 150 nm apart as shown in Figure 5.8(b-3). The chemical structure of chitin within the scales is pictured in Figure 5.8(c). Chitin is an attractive template material for surface sol-gel processing owing to available OH groups for reaction.

Thermogravimetric analyses (TGA) performed on chitin in a nitrogen atmosphere by Wanjun *et al.* revealed that only 10% of the chitin mass is lost at 287^{o}C while roughly 80% is degraded at 430^{o}C (continuous ramp rate = 5^{o}C/min) [37]. Zhang *et al.* reported a complete pyrolyzation temperature of 365^{o}C from TGA analyses performed on the wing scales of a *Thaumantis diores* butterfly in the presence of air [11]. Thus, to preserve the fine details of the scales, the applied coating must rigidify through crosslinking mechanisms prior to the onset of considerable degradation of the chitin template.

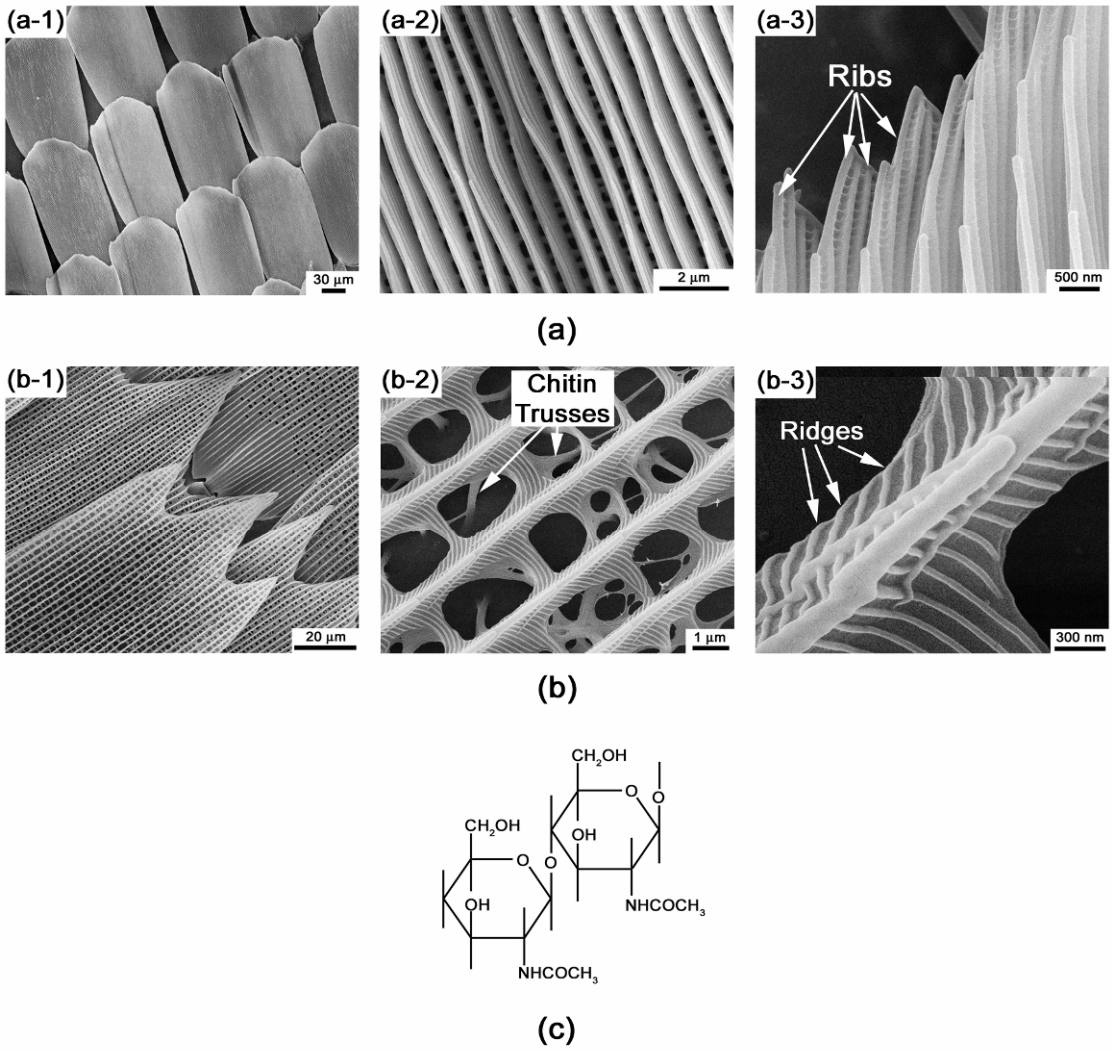

Figure 5.8: SEM images revealing the structural architecture of the blue *Morpho* scales observed on (a) the blue side and (b) the brown side of the wing. The chemical structure of the chitin polysaccharide, which is utilized as the fundamental building block for constructing the scales in (a-b), is shown in (c).

5.3.3 Surface Sol-Gel Synthesis of Titania-Based Coatings on the *Morpho* Wings

Two surface sol-gel-based deposition protocols were utilized to coat the blue Morpho butterfly scales and obtain rutile titania replicas after calcination. The first approach was to directly coat the scales with the pure Ti (IV) isopropoxide precursor and then anneal the coated structures at 900^{o}C to convert the coating to rutile. The second approach was to perform the surface sol-gel process with a tin-doped titania precursor. In Section 5.3.1, it was demonstrated that doping the solution with as little as 7 mol% SnO_2 would result in complete conversion to the rutile titania phase at temperatures as low as 450^{o}C. This alternative also resulted in a much smaller average rutile crystallite size.

The automated surface sol-gel system was used to deposit 20 layers of a 0.01 M Ti (IV) isopropoxide solution on one wing sample. A second wing sample was coated with 20 layers of a 0.01 M Ti (IV) isopropoxide solution doped with 15 mol% Sn (IV) isopropoxide. A doping concentration of 15 mol% was chosen to ensure that enough SnO_2 nuclei were incorporated into the gel network to allow for complete conversion of the titania phase to rutile upon thermal treatment. The surface sol-gel deposition parameters for both samples were the same. The chemisorption of the alkoxide precursor was performed for 10 min while all of the other deposition parameters were carried out as described in Section 5.2.4. The wing specimen possessing the pure Ti (IV) isopropoxide coating was cut in half and subjected to two different thermal treatments. One half was heat treated at 450^{o}C for 4 h, while the other half was heat treated at 900^{o}C for 1 h (heating rates described in Section 5.2.4). The wing specimen possessing the tin oxide-doped titania coating was also heat treated at 450^{o}C for 4 h.

Figures 5.9(a-b) provide a sequence of SEM images, showing higher magnification images moving from left to right, which were obtained after coating and firing the blue *Morpho* butterfly wing scales on the brown side with pure 0.01 M Ti (IV) isopropoxide. Figures 5.9(a-b) were obtained after annealing the coated scales at 450^{o}C (Figure 5.9(a)) and at 900^{o}C (Figure 5.9(b)). The tile-like arrangement of the scales was preserved (Figure 5.9(a)) through this heat-treatment process. From the higher magnification images it is clearly observed that the coatings annealed at 450^{o}C replicated the fine nanoridges which traverse each laminae with very fine nanoparticles. The waviness of the laminae is a result of a thin titania coating which could not bear its own weight after the chitin had been pyrolyzed.

The overall structure of the coated scales annealed at 900^{o}C (Figure 5.9(b)) was also preserved. However, the nanostructure of the scales annealed at 900^{o}C was not well preserved as shown in the higher magnification images presented in Figure 5.9(b) due to coarsening of the titania grains. The far right image in Figure 5.9(b) shows a faceted (600nm x 430nm) titania grain which demonstrates the severity of coarsening during this heat treatment. Each of the faceted grains elongated in the same general direction of the laminae which may have been the result of an Ostwald ripening process occurring on each ridge of the laminae.

The structure and phase analysis of the coated templates presented in Figure 5.8(a-b) were further evaluated using transmission electron microscopy (TEM) conducted by Dr. Ye Cai (Georgia Institute of Technology). Figure 5.10 presents the TEM analyses of the coated structures shown in Figure 5.9(a) which were heat treated at 450^{o}C for 4 h. Figures 5.10(a) and (b) are low and higher magnification TEM images which

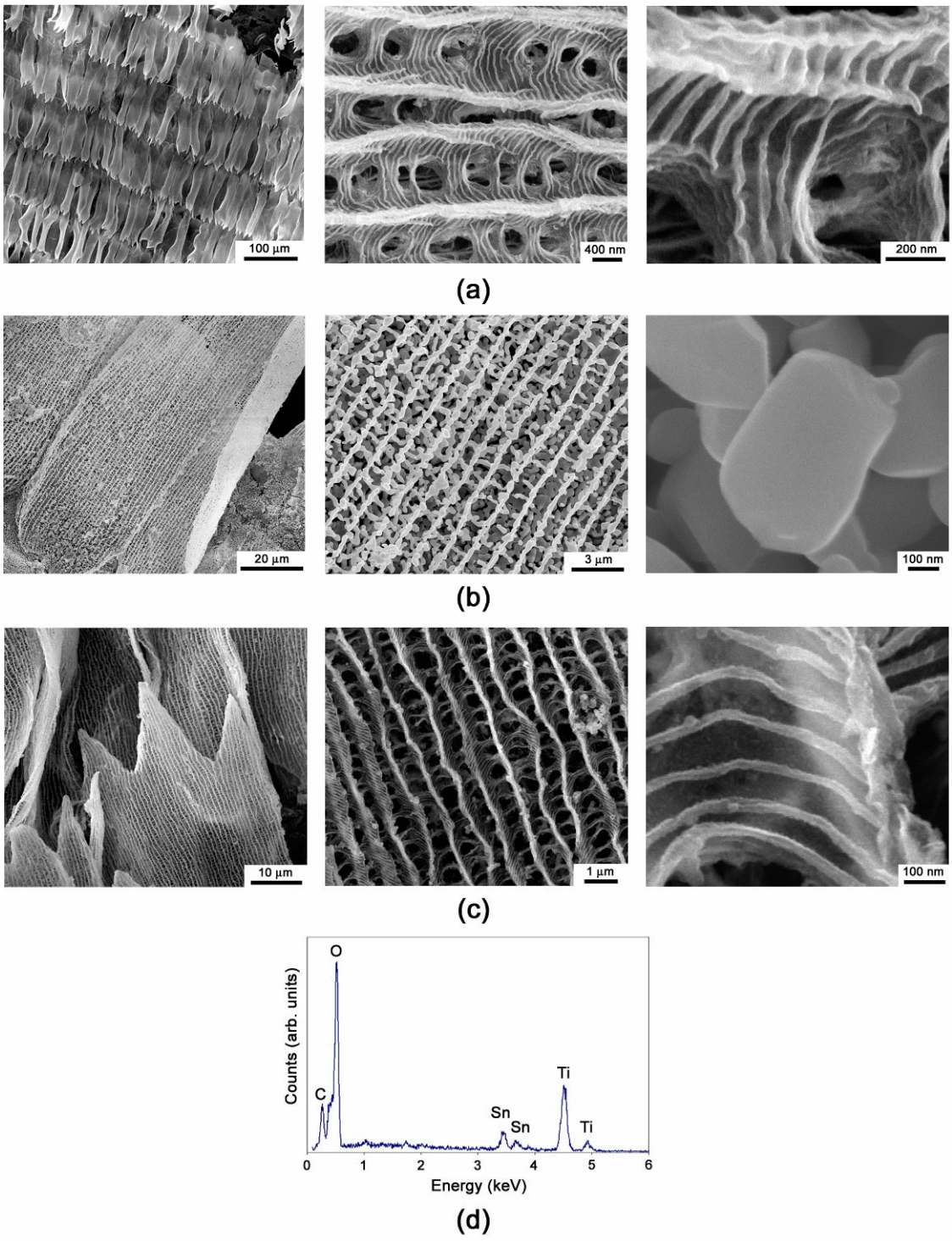

Figure 5.9: SEM images of the coated scales from the brown side of a blue *Morpho* butterfly wing which were obtained: (a-b) after 20 surface sol-gel depositions with a 0.01 M Ti (IV) isopropoxide solution and subsequent annealing at (a) 450^{o}C for 4 h and (b) 900^{o}C for 1 h, and (c) after 20 surface sol-gel depositions with a 0.01 M Ti (IV) isopropoxide solution doped with 15 mol% Sn (IV) isopropoxide followed by annealing at 450^{o}C for 4 h. (d) EDS analyses of the scales shown in (c).

demonstrated that the coatings were sufficiently thin as to be electron transparent. Figure 5.10(c) is a high resolution TEM image, obtained from the boxed region in Figure 5.10(b), which reveals that the grains were around 20 nm in diameter. The crystal structure of the grains was determined from the SAED pattern shown in Figure 5.10(d). The observed diffraction rings were indexed to diffraction from the (101), (103), (200), (105), (213), (116), and (215) planes of anatase titania.

Figure 5.11 presents the TEM analyses performed on the coated structures shown in Figure 5.9(b) which were heat treated at 900^{o}C for 1 h. Figure 5.11(a) confirms that the depositions performed using the surface sol-gel process produced conformal and continuous coatings with a high titania loading concentration on the scales. Faceted particles formed along the ridges of the laminae and are clearly observed in Figure 5.11(b). The average faceted particle size was measured from 20 different particles and was found to be ~139 nm x ~98 nm. The SAED pattern shown in Figure 5.11(c) was, surprisingly, consistent with anatase titania. From the HTXRD data presented in Section 5.3.1 it was expected that all of the anatase should have been converted to rutile at 900^{o}C. It may be possible that the diffraction pattern was obtained from a smaller anatase crystal which was more electron transparent. Regardless, this evidence provides further confirmation that it would be impossible to obtain pure rutile titania replicas which retain the nanostructured periodic features of the chitin-based scales from pure titanium alkoxide-derived coatings fired up to 900^{o}C.

The SEM images presented in Figure 5.9(c) were obtained after 20 surface sol-gel deposition cycles were performed on the *Morpho* wing scales using a 0.01 M Ti (IV) isopropoxide solution that was doped with 15 mol% Sn (IV) isopropoxide followed by

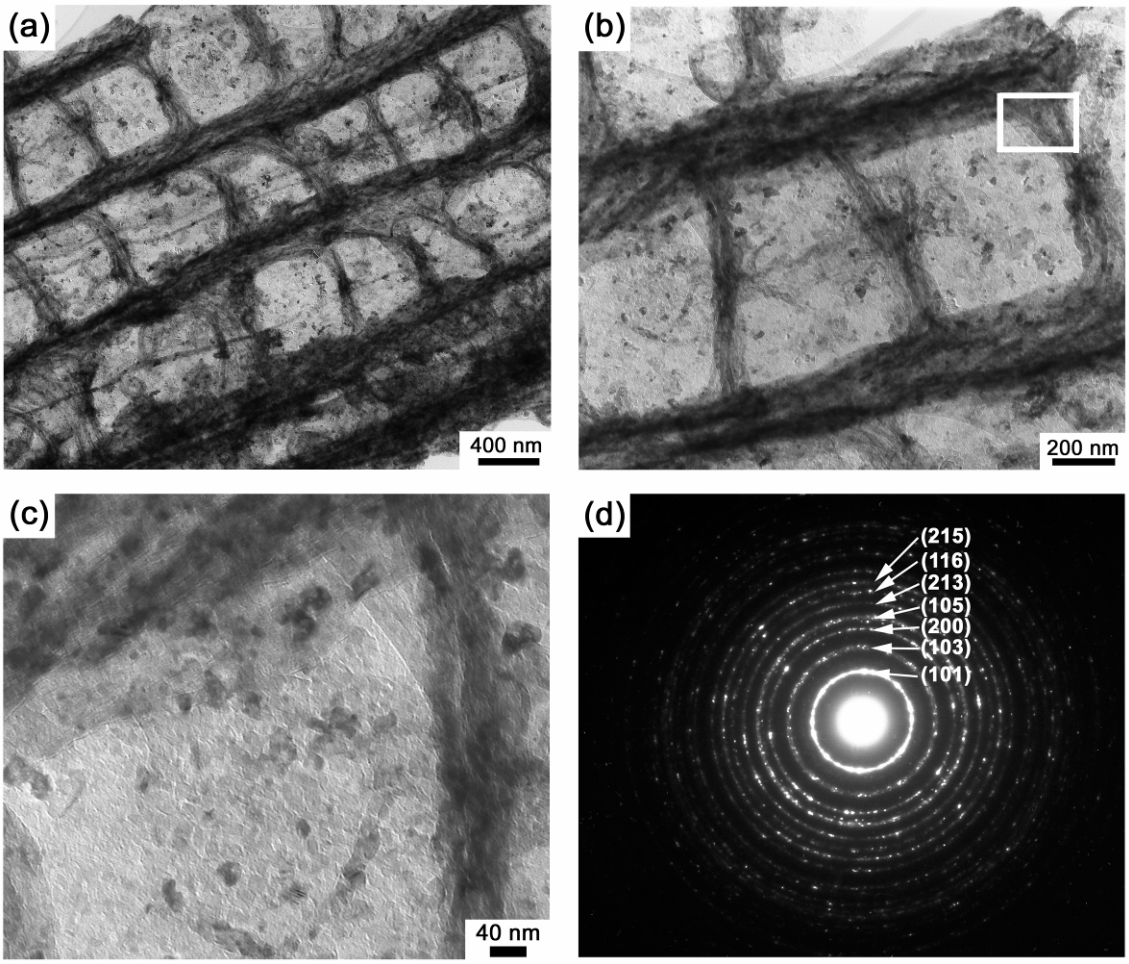

Figure 5.10: TEM characterization, conducted by Dr. Ye Cai (Georgia Institute of Technology), of the blue *Morpho* scales on the brown side subjected to 20 surface sol-gel depositions with a 0.01 M Ti (IV) isopropoxide solution followed by annealing at 450^{o}C for 4 h. The overall macrostructure of the scales (a-b) was preserved with a thin continuous polycrystalline coating of titania consisting of 20 nm crystallites (c). The calculated d-spacing's obtained from the SAED pattern in (d) were consistent with the anatase titania phase (JCPDS PDF #21-1272).

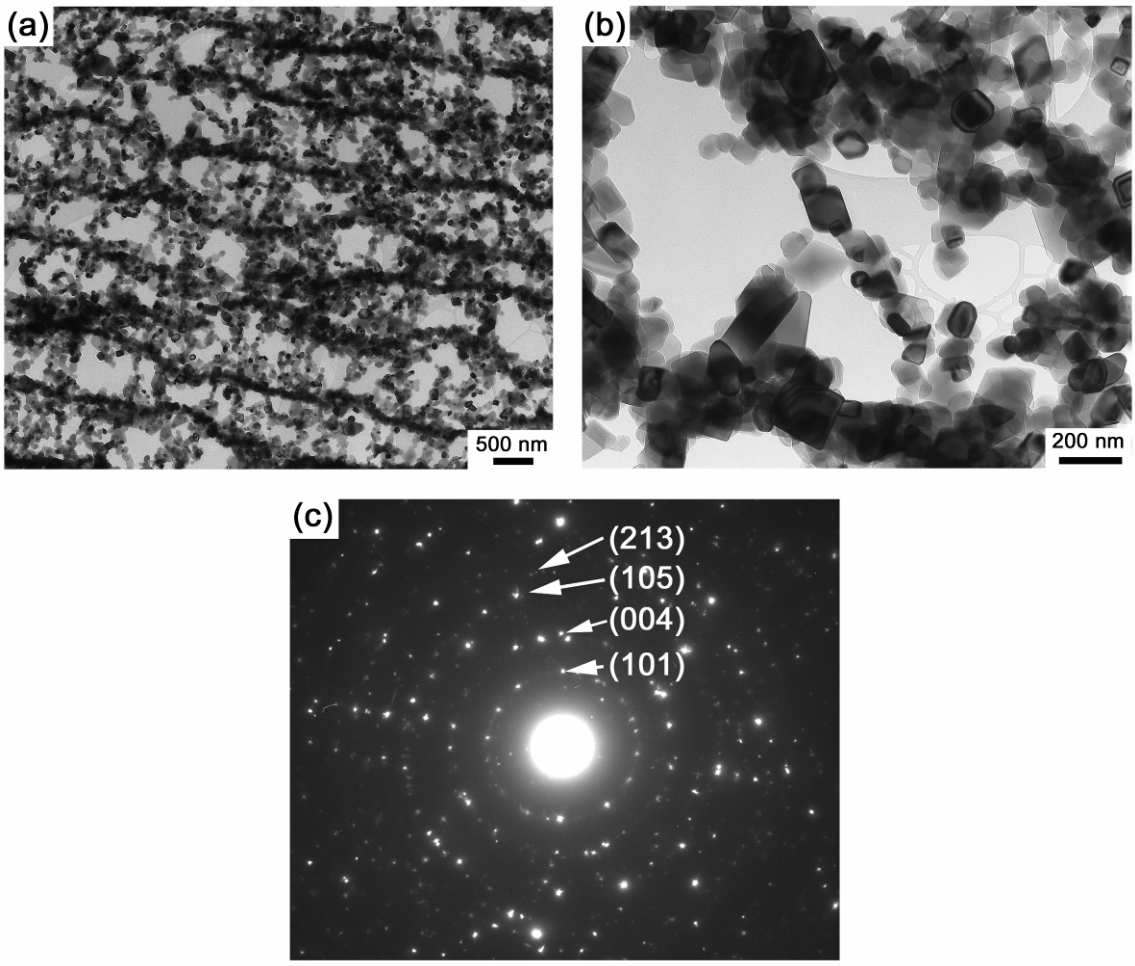

Figure 5.11: TEM characterization, conducted by Dr. Ye Cai (Georgia Institute of Technology), of the blue *Morpho* scales on the brown side of the wing subjected to 20 surface sol-gel depositions with a 0.01 M Ti (IV) isopropoxide solution followed by annealing at 900^{o}C for 1 h. The preservation of the scale macrostructure shown in (a) is indication of a conformal and continuous coating with a high initial titania loading concentration. The higher resolution image in (b) displays particles with varying grain sizes (average grain size of 20 crystals = 139x98 nm) which elongated along the ridges of the chitin template via an Ostwald ripening mechanism. The SAED pattern in (c) was consistent with the anatase TiO_2 phase (JCPDS PDF #21-1272).

annealing at 450°C for 4 h. The fine preservation of the chitin nanostructure is similar to that observed for the non-doped coatings applied to the scales shown in Figure 5.9(a). The fine structure and continuity of the coating were observed in the far right image. The waviness of the laminae was also attributed to the relatively thin coating. EDS elemental analysis (Figure 5.9(d)) of the coated structures revealed peaks which corresponded with O, Sn, Ti, and C. The presence of the C peak can be attributed to remaining chitin structure which had not completely ashed, as well as the carbon sticky tape on which the structures were placed for SEM analysis. EDS analysis performed on 10 different scale specimens yielded an average atomic Sn:Ti ratio of 3.2:20.6 (roughly corresponding to a doping concentration of 15.6 mol% SnO_2). This indicated that the tin isopropoxide was successfully incorporated into the titania gel network as a result of cohydrolysis in the surface sol-gel process.

To decrease the waviness of the laminae, a thicker coating was applied to a separate wing specimen by doubling the number of surface sol-gel coating cycles (i.e, 40 depositions at the same alkoxide concentration). Figure 5.12 reveals SEM images of the wing scales on the brown side of the wing that were coated with 40 surface sol-gel deposition cycles using the 0.01 M Ti (IV) isopropoxide solution doped with 15 mol% Sn (IV) isopropoxide. These specimens were also heat treated at 450°C for 4 h. With such extra deposition cycles more precise replication of the nanostructured features of the original scales was achieved. Figures 5.12(d) and (e) reveal cross-sections of a fractured scale. The truss-like structures elevating the porous laminae framework above the rippled underlying support can be clearly seen. These higher magnification images demonstrate that the coating was continuous and conformal. EDS analyses were also

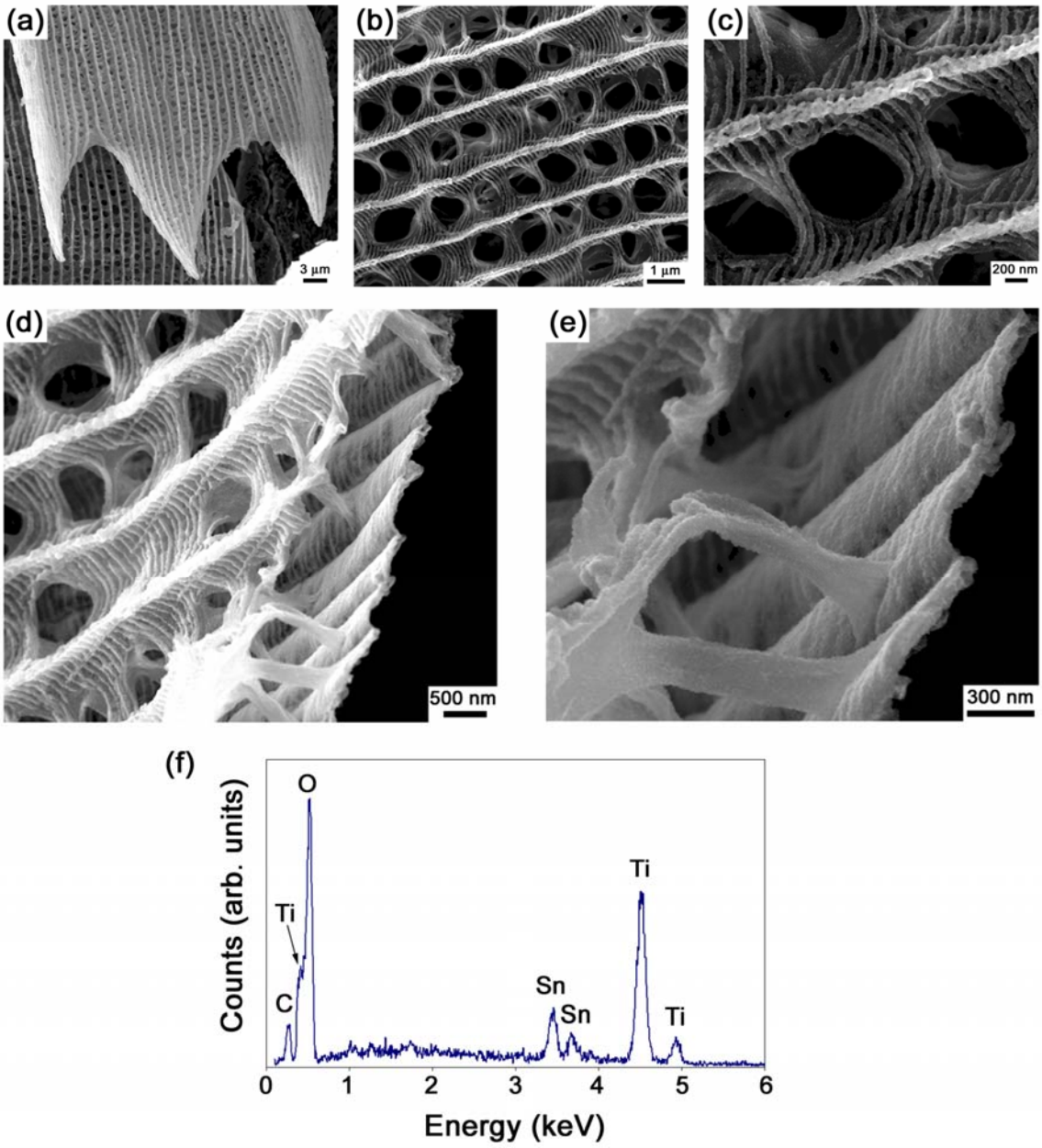

Figure 5.12: (a-e) SEM images of the scales from the brown side of a blue *Morpho* butterfly wing which were obtained after 40 surface sol-gel depositions with a 0.01 M Ti (IV) isopropoxide solution doped with 15 mol% Sn (IV) isopropoxide followed by annealing at 450^{o}C for 4 h. (f) Representative EDS spectra obtained from the coated scale pictured in (a).

performed on these coated structures (Figure 5.12(f)) and were comparable to the results reported earlier in Figure 5.9(d).

The TEM analyses performed on the structures coated with 40 deposition cycles clearly revealed a uniform coating over the ridges and valleys of the scales as shown in Figures 5.13(a) and (b). The continuous, nanocrystalline, nature of the coating was revealed clearly in Figure 5.13(c). The average crystallite size (obtained by measuring 20 crystallites) was found to be 15 nm. The well-defined sharp rings that are present in the electron diffraction pattern (Figure 5.13(d)) are also a good indication of the nanocrystalline nature of the coating. The rings in this pattern were indexed for diffraction from the (110), (101), (111), and (211) planes of the rutile titania phase. No other phases (e.g., anatase, brookite, or cassiterite) were detected. Thus, uniform coatings consisting of nanosized rutile particles could be realized which preserve the nanoarchitecture of the scale by doping the titanium alkoxide solution with a modest amount of a rutile nucleation agent (i.e., 15 mol% tin oxide). Such coatings were unattainable when pure titanium alkoxide solutions were deposited on the scales.

Figure 5.14 shows the coatings which were obtained on the blue scales during the same experimental run as the structures shown in Figure 5.12. The coatings on the scale shown in Figure 5.14(a) appear to be of the same high quality (e.g., even the nano box-like structures between the ribs of the laminae have been preserved) as those presented for the brown scales in Figure 5.12. However, the laminae structure tends to be wavier and the scales tend to curl more than for the coatings applied on the brown scales. This may be the result of the added mass of the coating being too heavy for the supportive trusses to bear. A simple remedy may be to increase the number of deposition cycles in

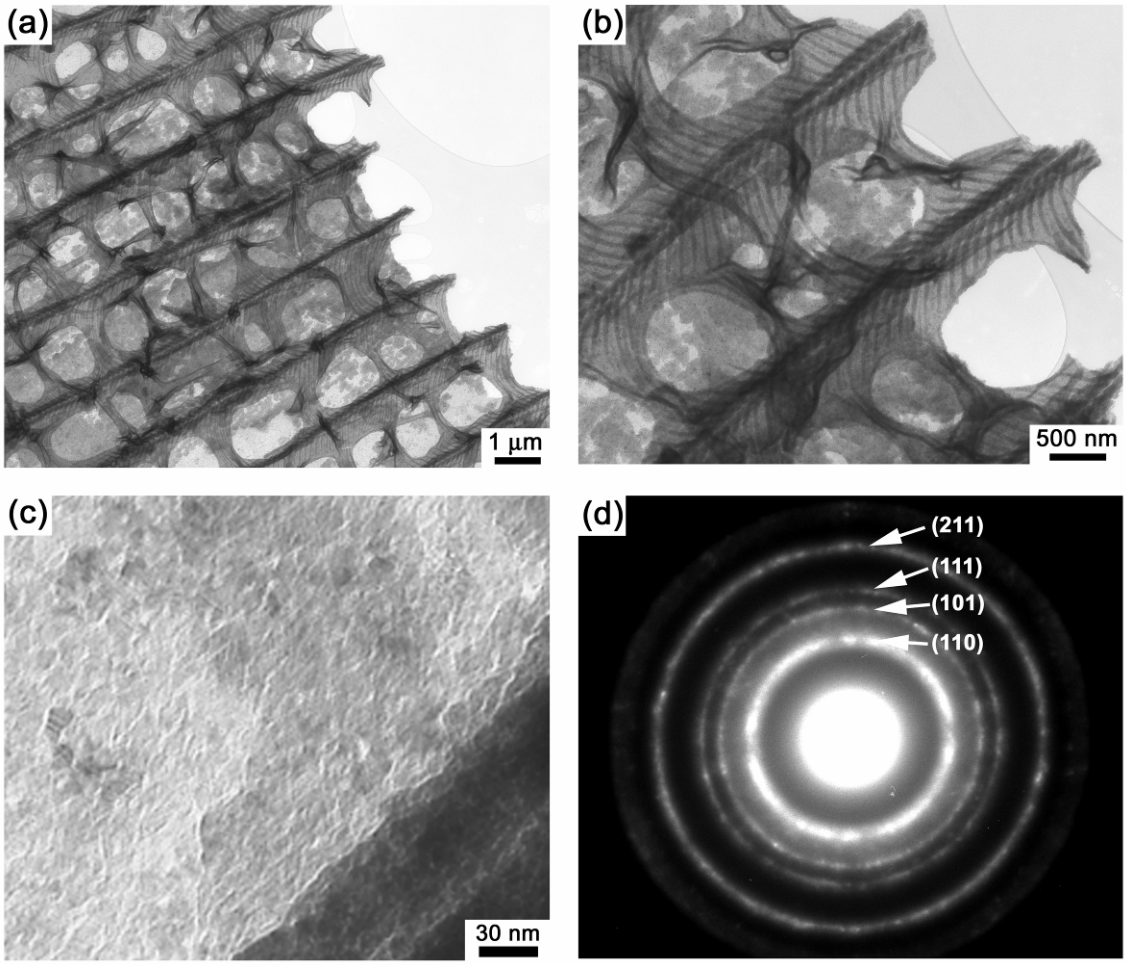

Figure 5.13: TEM characterization, conducted by Dr. Ye Cai (Georgia Institute of Technology), of the blue *Morpho* scales subjected to 40 surface sol-gel depositions with a 0.01 M Ti (IV) isopropoxide solution doped with 15 mol% Sn (IV) isopropoxide followed by annealing at 450°C for 4 h. The structural integrity of the scales was increased due to an increase in the number of deposition cycles which resulted in a thicker coating (a-b). The average particle size was measured to be 15 nm. The SAED pattern (d) was consistent with the rutile TiO_2 phase (JCPDS PDF #21-1276).

an effort to increase the coating thickness of the truss members and further rigidify the structure.

One of the other problems frequently observed with the coatings on the blue scales was excessive coating which covered over the spacing's between adjacent laminae as shown in Figure 5.14(b). This may be the result of insufficient drying after hydrolyzing the chemisorbed alkoxide layer with water to regenerate reactive OH groups. It is possible that residual water molecules may be trapped by capillary forces inside of the pores between the laminae. The porous structure in the brown scales is on a much larger scale which allows for better drying properties. Thus, longer drying times coupled with more solvent rinsing cycles may be required after the water has been evacuated to help dry the blue scales more efficiently.

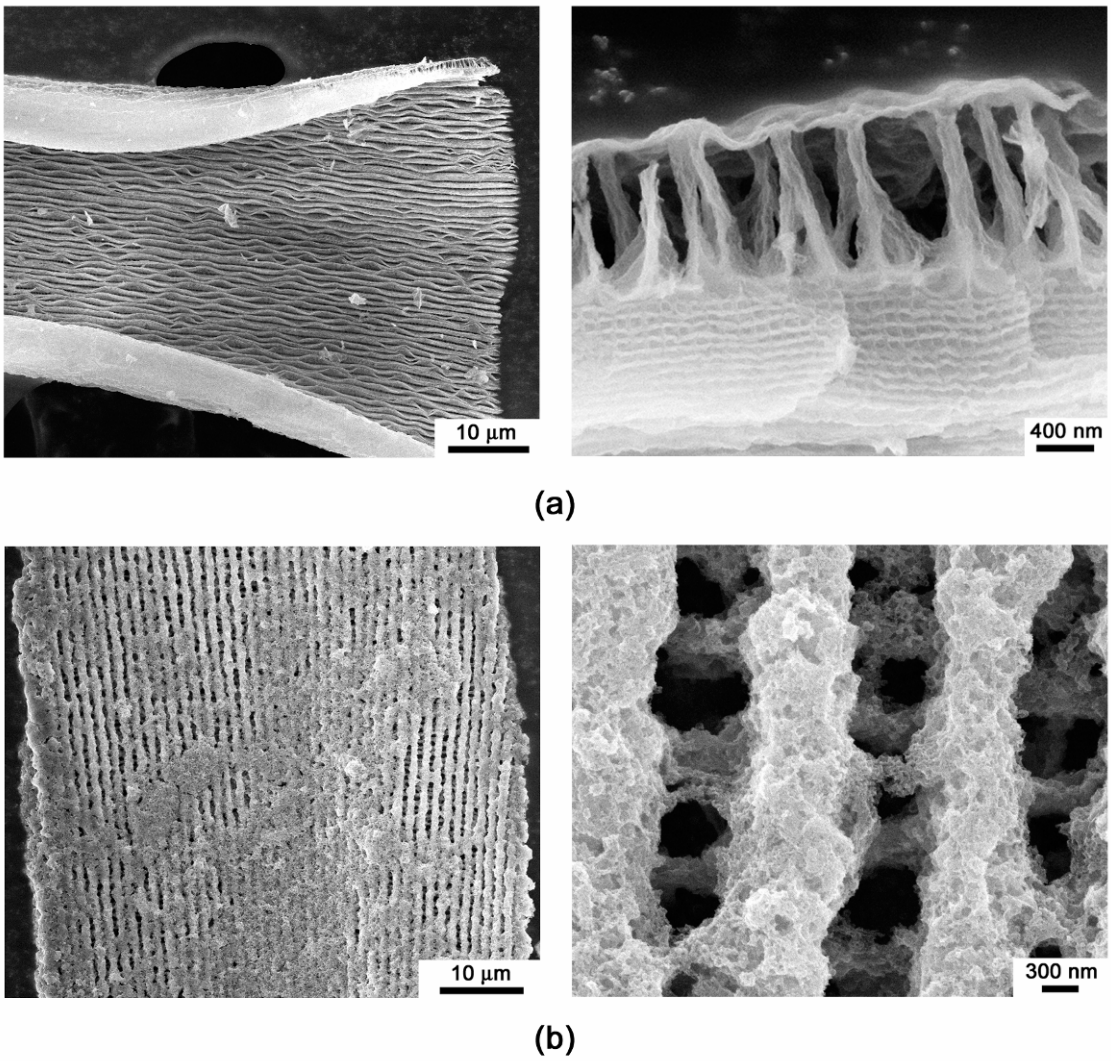

Figure 5.14: SEM images of the scales from the blue side of a blue *Morpho* butterfly wings which were obtained after 40 surface sol-gel depositions with a 0.01 M Ti (IV) isopropoxide solution doped with 15 mol% Sn (IV) isopropoxide followed by annealing at 450^{o}C for 4 h. The scales tend to curl more during the heat treatment process possibly due to the trusses inability to support the mass of the coated lamella as shown in (a). Excessive coating was also observed which may be the result of capillary forces trapping the water molecules inside of the nanoporous network as demonstrated in (b).

5.4 Summary and Outlook

This work provides the first demonstration of the use of a sol-gel based deposition technique to controllably apply conformal and continuous nanocrystalline rutile TiO_2 coatings on the scales of a blue Morpho butterfly wing. Controlled layer-by-layer film growth was achieved using an automated surface sol-gel pumping system to sequentially expose the wing specimens to a tin-doped (15 mol% SnO_2) titanium isopropoxide solution followed by rinsing with an anhydrous solvent and subsequent hydroxyl reactivation. The thickness and structural integrity of the coating on the scales was dependent upon the number of deposition cycles performed. Rutile titania replicas of the scales were obtained after a modest heat treatment at 450^{o}C for 4 h in air. Control experiments, performed by coating the scales with non-doped titania precursors, demonstrate the need for utilizing doped precursors to obtain rutile TiO_2 coatings with nanocrystalline grains which thereby preserve the intricate nanoarchitectural framework of the scales. Precipitation trials revealed that the anatase to rutile titania phase transformation can be completely avoided by doping the titanium (IV) isopropoxide solution with as little as 7 mol% tin (IV) isopropoxide.

5.5 References

[1] E. Yablonovitch, *Physical Review Letters*, **58**, 2059-2062 (1987).

[2] S. John, *Physical Review Letters*, **58**, 2486-2489 (1987).

[3] P. Vakusic, *Physics Today*, October, 82-82 (2006).

[4] A. R. Parker, H. E. Townley, *Nature Nanotechnology*, **2**, 347-353 (2007).

[5] M. Srinivasarao, *Chemistry Reviews*, **99**, 1935-1961 (1999).

[6] P. Vakusic, J. R. Sambles, C. R. Lawrence, *Nature*, **404**, 457 (2000).

[7] S. Yoshioka, S. Kinoshita, *Journal of the Optical Society of America A*, **23**, 134-141 (2006).

[8] E. Yablonovitch, *Scientific American*, **285**, 47-55 (2001).

[9] J. Huang, X. Wang, Z. L. Wang, *Nano Letters*, **6**, 2325-2331 (2006).

[10] G. Cook, P. L. Timms, C. Göltner-Spickermann, *Angewandte Chemie International Ed.*, **42**, 557-559 (2003).

[11] W. Zhang, D. Zhang, T. Fan, J. Ding, Q. Guo, H. Ogawa, *Microporous and Mesoporous Materials*, **92**, 227-223 (2006).

[12] H. Tada, S. E. Mann, I. N. Miaulis, P. Y. Wong, *Optics Express*, **5**, 87-92 (1998).

[13] D. R. Lide, CRC Handbook of Chemistry and Physics 77th Ed. (CRC Press Inc., Boca Raton, FL) p. **4**-132 (1996).

[14] D. R. Lide, CRC Handbook of Chemistry and Physics 77th Ed. (CRC Press Inc., Boca Raton, FL) p. **4**-132 (1996).

[15] D. R. Lide, CRC Handbook of Chemistry and Physics 77th Ed. (CRC Press Inc., Boca Raton, FL) p. **4**-136 (1996).

[16] X. Wang, M. Fujimaki, K. Awazu, *Optics Express*, **13**, 1486-1497 (2005).

[17] J. E. G. J. Wijnhoven, L. Bechger, W. L. Vos, *Chemistry Materials*, **13**, 4486-4499 (2001).

[18] E. D. Palik, ed., *Handbook of Optical Constants of Solids*, (Academic Press, San Diego, CA, 1985).

[19] D. J. Reidy, J. D. Holmes, M. A. Morris, *Journal of the European Ceramic Society*, **26**, 1527-1534 (2006).

[20] J. Nair, P. Nair, F. Mizukami, Y. Oosawa, T. Okubo, *Materials Research Bulletin*, **34**, 1275-1290 (1999).

[21] J. S. King, C. W. Neff, D. L. Heineman, E. D. Graugnard, C. J. Summers, *Materials Research Society Symposium Proceedings*, **797**, 75-80 (2004).

[22] H. Koyama, M. Fujimoto, T. Ohno, H. Suzuki, J. Tanaka, *Journal of the American Ceramic Society*, **89**, 3536-3540 (2006).

[23] X. Jiang, T. Herricks, Y. Xia, *Advanced Materials*, **15**, 1205-1209 (2003).

[24] H. Xu, W. Wei, C. Zhang, S. Ding, X. Qu, J. Liu, Y. Lu, Z. Yang, *Chemistry and Asian Journal*, **2**, 828-836 (2007).

[25] D. Heineman, Optimization of ALD grown titania thin films for the infiltration of silica photonic crystals. 2004, Georgia Institute of Technology.

[26] J. King, E. Graugnard, O. M. Roche, D. N. Sharp, J. Scrimgeour, R. G. Denning, A. J. Tuberfield, C. J. Summers, Advanced Materials, 18, 1561-1565 (2006).

[27] K-N. P. Kumar, K. Keizer, A. J. Burggraaf, T. Okubo, H. Nagamoto, Journal of Materials Chemistry, 3, 923-929 (1993).

[28] K-N. P. Kumar, K. Keizer, A. J. Burggraaf, *Journal of Materials Science Letters*, **13**, 59-61 (1994).

[29] Z. Yanqing, S. Erwei, C. Zhizhan, L. Wenjun, H. Xingfang, *Journal of Materials Chemistry*, **11**, 1547-1551 (2001).

[30] Y. Li, N-H. Lee, D-S. Hwang, J. S. Song, E. G. Lee, S-J. Kim, *Langmuir*, **20**, 10838-10844 (2004).

[31] H. P. Naidu, A. V. Virkar, *Journal of the American Ceramic Society*, **81**, 2176-2180 (1998).

[32] P. K. Nair, F. Mizukami, J. Nair, M. Salou, Y. Oosawa, H. Izutsu, K. Maeda, T. Okubo, *Materials Research Bulletin*, **33**, 1495-1502 (1998).

[33] A. A. Gibb, J. F. Banfield, *American Mineralogist*, **82**, 717-728 (1997).

[34] B. D. Cullity, *Elements of X-Ray Diffraction*, Addison-Wesley, Reading, MA (1978).

[35] www.butterflyutopia.com/blue_morpho.html (Accessed November 2, 2007).

[36] www.earthsbirthday.org/explore/kids/photosbluemorpho.htm--© Larry Kimball & Barbara Magnuson, (Accessed November 2, 2007).

[37] T. Wanjun, W. Cunxin, C. Donghua, *Polymer Degradation and Stability*, **87**, 389-394 (2005).

CHAPTER 6: THE SURFACE SOL-GEL PROCESSING OF RUTILE TITANIA PHOTONIC CRYSTALS

6.1 Introduction

Photonic crystals are two-dimensional (2-D) or three-dimensional (3-D) periodic structures with repeating units of high and low refractive index materials which are designed to manipulate the flow of light through Bragg diffraction [1]. When a ray of light (photons) enters into a periodic dielectric structure (photonic crystal), the rays are scattered by Bragg diffraction from the planes possessing the higher refractive index [2]. In a well-designed 3-D dielectric photonic crystal structure, Bragg diffraction will prevent certain wavelengths from propagating through the crystal in certain directions which leads to a photonic band gap (PBG) [3]. This implies that light can be localized or trapped within the structures and spontaneous emission of the light would be forbidden, as proposed by Yablonovitch and John in 1987 [4-5]. Major technological innovations may be realized in the fields of quantum computing, optical communications, solar cells, and even sensors with properly designed photonic crystal structures [6-10].

Much of the PC research has focused on fabricating 3-D periodic dielectric structures, due to the possibility of inhibiting and confining light in all 3 dimensions. Multi-beam interference lithography (or holography) provides one of the most promising fabrication methods for producing templates for PC fabrication. With this technique, all five 2-D and all fourteen 3-D Bravais lattices may be formed using three or four coherent laser beams to transfer a holographically-defined image to a photosensitive epoxy [11]. The regions of the epoxy exposed to the focused laser are polymerized, while the unexposed areas remain unpolymerized and can be dissolved in an organic solvent [12].

However, the resulting polymeric PC structures are limited in that the refractive index difference between the polymer and air is not sufficiently high as to provide a complete 3-D PBG [11].

Campbell and his coworkers provided the first demonstration of utilizing this holographic technique to pattern a diamond-like FCC lattice of pores (inverse opal) in a 10 μm thick SU-8 photoresist [12]. Earlier calculations performed for a FCC lattice of pores reveals that the index of refraction of the solid phase must be ~ 2.8 for the material to possess a complete 3-D PBG [13, 14]. As discussed in Chapter 5, rutile titania is the desired coating material due to its high refractive index (n=2.9 at λ = 400 nm) [15], low optical absorption [16], and good thermal stability [17]. Accordingly, Campbell *et al.* tried backfilling the pores of the polymer template with titanium (IV) ethoxide followed by a heat treatment of 575^{o}C to crystallize the titania coating and burn out the polymer. They observed a 30% shrinkage in the structure which they partially attributed to the change in density of the titanium tetra-ethoxide and the anatase titania phase. As a result, they observed extensive fracturing of the structure and a loss in the opalescent properties of the crystal due to strong scattering [12].

Recently, King, *et al.* infiltrated a similar holographically-defined PC structure with amorphous titania using atomic layer deposition (ALD) [18]. They experimentally observed a red shift in the stop band after infiltrating the structure with 50 nm of amorphous titania which matched very well with the theoretical calculations due to infiltration of the pores. This provided a demonstration of the possibility of tuning the PBG in the NIR region via layer-by-layer film growth. However, King, *et al.* also encountered unsatisfactory results when they tried to pyrolyze the SU-8 template at

400°C to crystallize the amorphous titania phase and maximize the refractive index contrast. They, therefore removed the SU-8 using an oxygen plasma treatment which did not harm the amorphous titania structure. After removing the SU-8, they observed a blue shift in the stop band and an increase in the reflectivity from 20% for the SU-8 template to 65% for the amorphous titania/air PC structure [18]. While King, *et al.* present compelling evidence that coupling holographic fabrication with layer-by-layer deposition could potentially yield visible optical PC's, they also demonstrate the need for obtaining a suitable experimental protocol for coating a high refractive index material (i.e., rutile titania) on the SU-8 template.

The purpose of this Chapter is to demonstrate a suitable experimental protocol for coating holographically-defined PC structures with rutile titania to achieve a suitable refractive index contrast for a complete PBG. In Chapter 5, uniform coatings of nanocrystalline rutile titania were applied in a layer-by-layer manner to the delicate architectures of butterfly wings using an automated surface sol-gel system. This was accomplished by doping the titania sol with a small amount of a rutile nucleating agent (i.e., 15 mol% tin oxide). However, crystallization of these coatings required a heat treatment of 450°C. The work of Campbell *et al.* and King *et al.* indicated that such thermal treatment is not the best method for removing the SU-8 template or crystallizing the coating. Another strategy has been pursued in this work which allows for rutile titania formation with a thermal treatment at only 80°C, on the SU-8 structures, after conformal coating with a tin-doped titania sol using an automated surface sol-gel system.

6.2 Experimental Procedure

6.2.1 Materials

The Ti (IV) isopropoxide (99.995%, metals basis) precursor and tris-(hydroxymethyl)-aminomethane (99%) were obtained from Alfa Aesar (Ward Hill, MA). The Sn (IV) isopropoxide (10% w/v) and anhydrous 2-propanol were purchased from Chemat Technology, Inc. (Northridge, CA). Pure DI water (resistivity of 18.2 MΩ·cm, from a NANOpure Diamond UV/UF system, Barnstead International) was used in all experiments for hydrolyzing the precursors. Fritted glass filtration funnels (15 mL, Type E, 4-8 μm pore size) were purchased from Ace Glass (Vineland, NJ) and were used without chemical surface modification. The 3-D holographically-patterned photonic crystal polymer templates were fabricated by Dr. Yongan Xu (University of Pennsylvania) and delivered to MRW as part of a collaborative Navy funded research project termed APEX (Advanced Processing-tools for Electromagnetic/acoustic Xtals).

6.2.2 Holographic Fabrication of the 3-D Diamond-Like Polymer Templates

The 3D polymer templates were fabricated by exposing the negative photoresist, SU8, to four umbrella-like visible laser beams split from one coherent laser source (λ=532nm, diode-pumped Nd:YVO_4 laser). The central beam was circularly polarized and oriented perpendicular to the photoresist film. The other three beams were polarized linearly in a plane formed by the wave vectors of the central beam and surrounding beam. The wave vector of each beam was $k_0=\pi/a[333]$, $k_1=\pi/a[511]$, $k_2=\pi/a[151]$, and $k_3=\pi/a[115]$ respectively. The polarization vectors of beams 1, 2, and 3 were e_1=[-0.272 0.680 0.680], e_2=[0.680 -0.272 0.680], and e_3=[0.680 0.680 -0.272], respectively. The

intensity ratio was 1.8:1:1:1. The circular polarization of the central beam distributed the intensity equally to the surrounding beams.

The photoresist was prepared by mixing Epon SU-8 pellets and 2.0 wt % Irgacure 261 (from Ciba Specialty Chemicals) as visible photoinitiators in γ-butyrolactone (GBL, Aldrich) to form a ~ 58 wt% solution. The photoresist solution was then spin-coated on a glass substrate at 2000 rpm for 30s, resulting in a film thickness of ~6 μm. The film was exposed to the superimposed interference beams (laser output of 1W) for 1-2 s. After post-exposure bake (PEB) at 65^{o}C and 95^{o}C, respectively, the exposed film was developed in propylene glycol monomethyl ether acetate (PGMEA, Aldrich) to remove unexposed or weakly exposed films, and thereby yielding 3D microporous structures. 3D samples were dried by using a supercritical CO_2 dryer (SAMDRI®-PVT-3D from Tousimis) after the development.

6.2.3 Hydroxyl Group Surface Modification of the SU-8 Template

As a result of the holographic patterning technique, there are a number of residual epoxy rings that have not been crosslinked in the final SU-8 structure. These unreacted groups can be used as nucleophilic reaction sites for amplifying the number of hydroxyl groups (for enhanced surface sol-gel processing) on the SU-8 with aminoalcohols (Note: thiolalcohols may also be used). To determine the optimum reaction conditions for generating the highest concentration of OH groups, a holographically-patterned SU-8 structure was immersed in an ethanol-based solution of 0.1 M tris(hydroxymethyl)aminomethane (TRIS) in 10 min increments (i.e., 10, 20, 30, 40, and 50 min) at 50^{o}C (Note: the TRIS has a limited solubility in ethanol and must be stored at 50^{o}C to prevent precipitation). The SU-8 template was removed from the solution after

each 10 min exposure to the TRIS and was rinsed with reagent grade ethanol for 1 min and dried under flowing nitrogen. Contact angle wetting measurements were performed by dripping DI water onto the patterned SU-8 photonic crystal template and measuring the contact angle within 2 seconds using a Cam 100 contact angle meter (KSV Instruments, Inc., Monroe, CT) located in Professor Vladimir Tsukruk's lab (Georgia Institute of Technology). Each measurement was performed three separate times and the average contact angle was recorded.

6.2.4 Application of Tin Oxide-Doped Titania Surface Sol-gel Coatings

A 150 mL common alkoxide solution of 0.1 M Ti (IV) isopropoxide doped with 10 mol% Sn (IV) isopropoxide was prepared by first inoculating (pipetting) Sn (IV) isopropoxide into anhydrous 2-propanol under magnetic stirring conditions. After the solution was homogenized for 10 min, the Ti (IV) isopropoxide was inoculated into the same solution and homogenized.

The glass slide bearing the SU-8 template sample was positioned inside of a 15 mL filtration funnel in the same fashion as the butterfly templates shown previously in Figure 5.1. Surface sol-gel depositions were performed by pumping 5 mL of precursor solution into the filtration flask to completely immerse the template. After a predetermined chemisorption reaction time (10 min), the solution was then evacuated for 18 seconds under vacuum filtration. While still under vacuum, 5 mL of anhydrous 2-propanol was pumped into the flask (immersing the template) three separate times to rinse away any physisorbed alkoxide. The vacuum pump was then turned off and 5 mL of water was pumped into the system. After a 1 min incubation time, the water solution was evacuated for 10 sec via vacuum filtration. The SU-8 crystal was again rinsed three

more times with 2-propanol to help rinse away any remaining water molecules. The sample was then dried by aspirating hot air from a blow dryer past the sample while the system was still under vacuum for 5 minutes.

6.2.5 Oxygen Plasma Treatment of the Coated SU-8 Templates

The coated SU-8 structures were exposed to a pure oxygen plasma using an expanded plasma cleaner (PDC-001, Harrick Scientific Products Inc., Pleasantville, NY) for 8 h at 29.6W (high setting) to decompose the polymer template.

6.2.6 Materials Characterization

The morphology of the coated SU-8 structures was characterized using a field emission scanning electron microscope (1530 SEM, LEO/Zeiss Electron Microsopy, Gmbh, Thornwood, NY). Microchemical analyses were performed using energy dispersive spectroscopy (EDS) over 20 different sections of the coated sample to ascertain the atomic ratio of Sn to Ti using an Oxford Inca EDS detector attached to the scanning electron microscope. FIB-SEM analysis was performed with a DBFIB FE-SEM equipped with a gallium ion FIB (FEI Company, Hillsboro, USA). Transmission electron microscopy was conducted with a JEOL 4000 EX instrument by Dr. Ye Cai (Georgia Institute of Technology). Fourier transform infrared spectroscopy (FTIR) was performed in Professor Joe Perry's lab (Georgia Institute of Technology).

6.3 Results and Discussion

The direct application of sol-gel derived coatings on an SU-8 substrate is complicated by the fact that SU-8 is inherently a hydrophobic polymer due to the

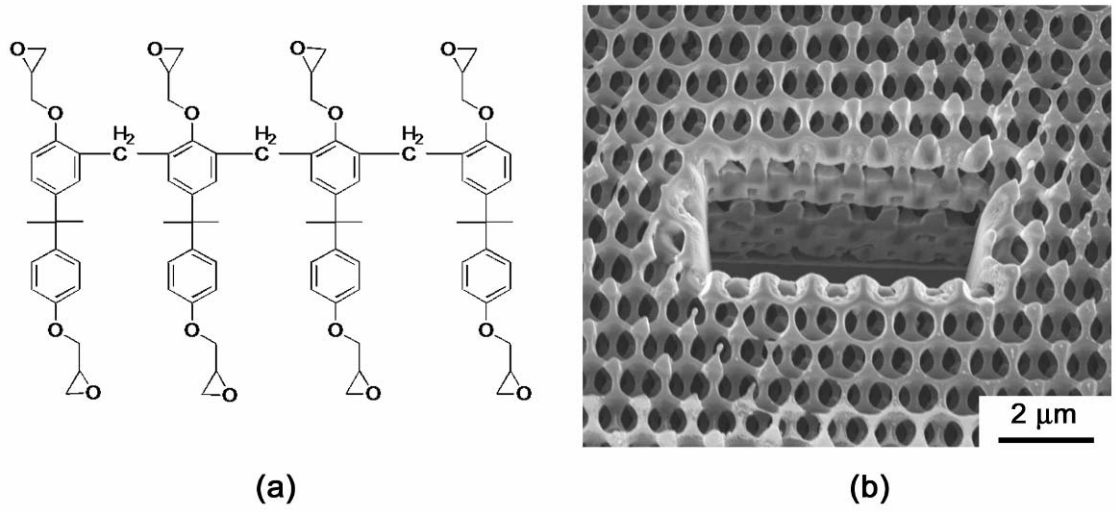

Figure 6.1: The chemical structure of the SU-8 photoresist (a) which is used to make the 3-D photonic crystal structures (b) which were used in this work. The thickness of the structure shown in (b) is ~ 6 µm. Note: the SU-8 structure contains 8 epoxy rings per SU-8 molecule along with hydrophobic methyl and aromatic groups.

presence of the aromatic and methyl groups that are present in its chemical structure Figure 6.1(a) [19]. Also, there are little (if any) hydroxyl functionalities that provide nucleophilic reaction sites for the alkoxide precursors. Consequently, it is expected that using the surface sol-gel process to deposit alkoxide derived coatings directly on the untreated SU-8 templates would result in patchy and or discontinuous coatings. Furthermore, infiltration of water into the bulk of the patterned SU-8 photonic crystal template (Figure 6.1(b)) would be hindered due to the hydrophobic nature of the polymer. Incomplete water penetration throughout the bulk of the crystal would result in incomplete hydrolysis of exposed alkoxide groups present in the internal SU-8 structure. Consequently, fewer sites would then be available for attachment of additional alkoxide molecules throughout the internal structure of the template. This would result in a reduction in the coating uniformity and a loss in the periodicity of the crystal structure

with distance from the external template surface. Therefore, the chemical structure of the SU-8 must first be modified to allow for, i) an amplified distribution of hydroxyl groups that act as nucleophilic reaction sites to bind the alkoxide precursor, and ii) a decrease in the hydrophobicity of the SU-8 structure.

Nordström *et al.* has previously demonstrated that the contact angle of water on SU-8 can be decreased via reacting ethanolamine with the epoxy groups that are left unreacted on the surface of the SU-8 after the cross-linking step in the developing process [19]. This reaction opens the epoxy ring and provides 2 OH groups per reaction. Tris-(hydroxymethyl)-aminomethane (here after referred to a Tris) was used in this work as an alternative aminoalcohol, as 4 OH groups are provided per reaction with an epoxy group. Nordström *et al.* also reported that capillary forces were not sufficient to transport a water droplet through a 100 μm microfluidic channel in hydrophobic SU-8 [19]. Given that the pore size of the SU-8 photonic crystal templates in this work are much smaller in diameter (~800 nm Figure 6.1(b)), contact angle measurements were conducted on the patterned and modified PC SU-8 templates. The intent of this investigation was to determine if the wetting properties of the SU-8 template could be enhanced by amplifying the number of OH groups via reaction of the residual epoxy groups in the SU-8 structure with Tris.

The same SU-8 PC template was immersed in an ethanolic 0.1 M Tris solution at 50^{o}C in 10 minute increments up to a total time of 50 min. A total of three contact angle measurements were performed after each immersion time. Pictures were immediately recorded (within 2 sec) for a contact angle measurement after the water was dripped onto the template. Figure 6.2(a) shows the results of the measured water contact angle (θ) on

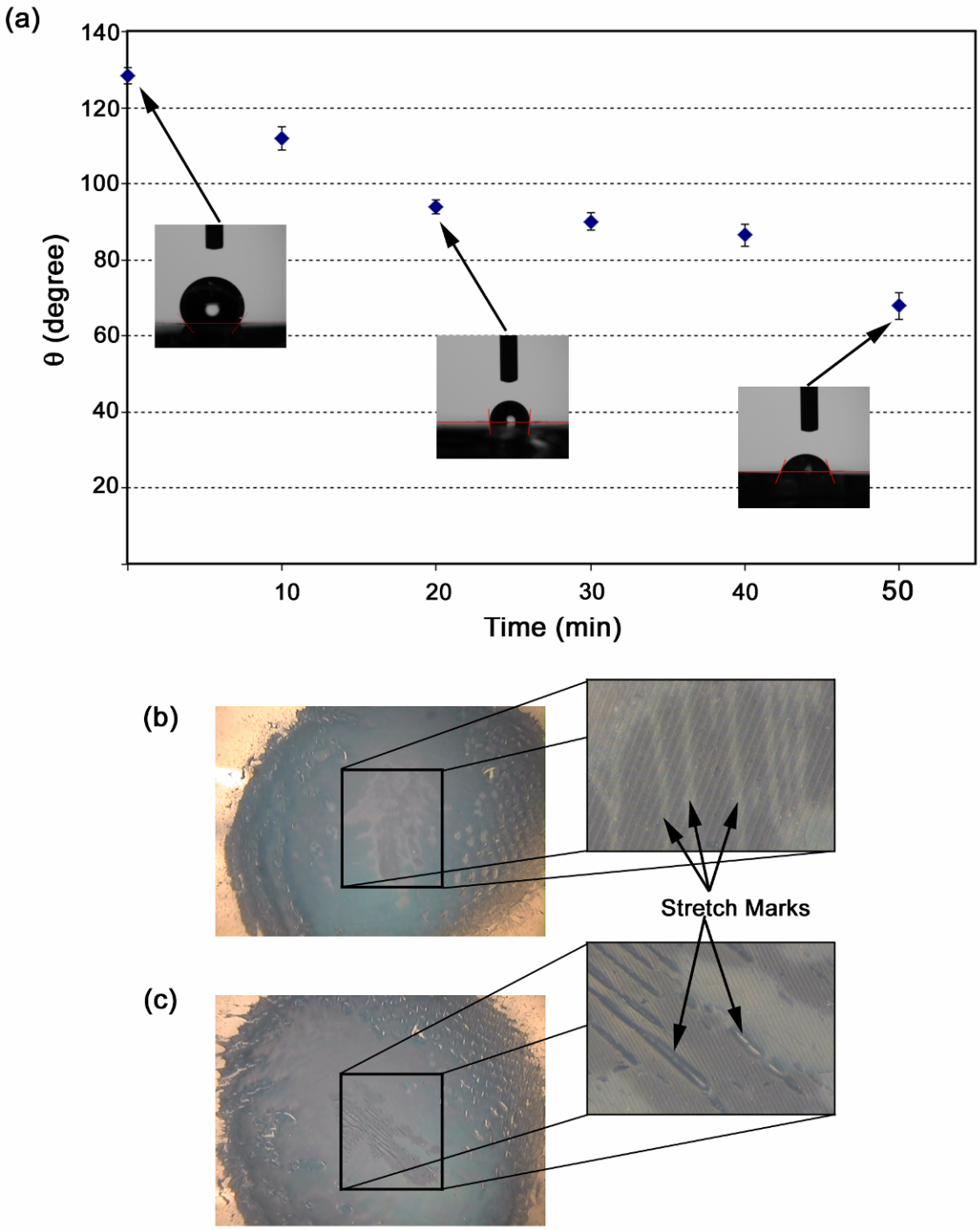

Figure 6.2: Water contact angle measurements obtained after soaking the patterned PC structures in an ethanolic 0.1 M Tris solution for 0, 10, 20, 30, 40, and 50 min (a). Optical microscope images of the as-received SU-8 structure (b) revealed imperfections (cracks, stretch marks, etc) which were greatly magnified after treating the crystal in the Tris solution for 50 min (c).

the SU-8 as a function of immersion time. Initially, the as-received (untreated) patterned SU-8 structure possessed a contact angle of 128^{o}. With increasing exposure to the TRIS solution, the contact angle decreased. However, prolonged exposure of the templates to the Tris solution deteriorated the structure of the crystal. Figures 6.2(b-c) reveal optical microscope images obtained of the as-received SU-8 PC and after soaking the PC for 50 min in the Tris solution. Figure 6(b) shows imperfections (striated stretch marks) that are present on the patterned polymer structures. Such imperfections arise as a result of stresses between the polymer and substrate interface due to shrinkage of the patterned SU-8 template during the curing process. It was observed that soaking the crystals for extended periods of time (over 20 min) in the Tris solution magnified such structural imperfections of the patterned SU-8 template. Thus, a 20 min exposure to the Tris solution was chosen to amplify the OH groups without severely deteriorating the structure of the patterned photonic crystal templates.

FTIR measurements were also used to verify the presence and amplification of OH groups on the patterned SU-8 structures. Figure 6.3 shows IR spectra obtained from the SU-8 PC structure after the separate processing steps. The as-received SU-8 sample exhibited strong absorption bands for C-H (3.3-3.5 μm) and weak absorption bands for O-H stretches (2.8-2.9 μm). However, after treating the sample with 0.1 M Tris both the O-H and C-H absorption bands were magnified due to the addition of both C-H and O-H functionalities provided by the Tris. This IR measurement was consistent with the results of the contact angle measurements and revealed that treating SU-8 with Tris effectively amplified OH groups, which increased the hydrophylicity of the SU-8 sample.

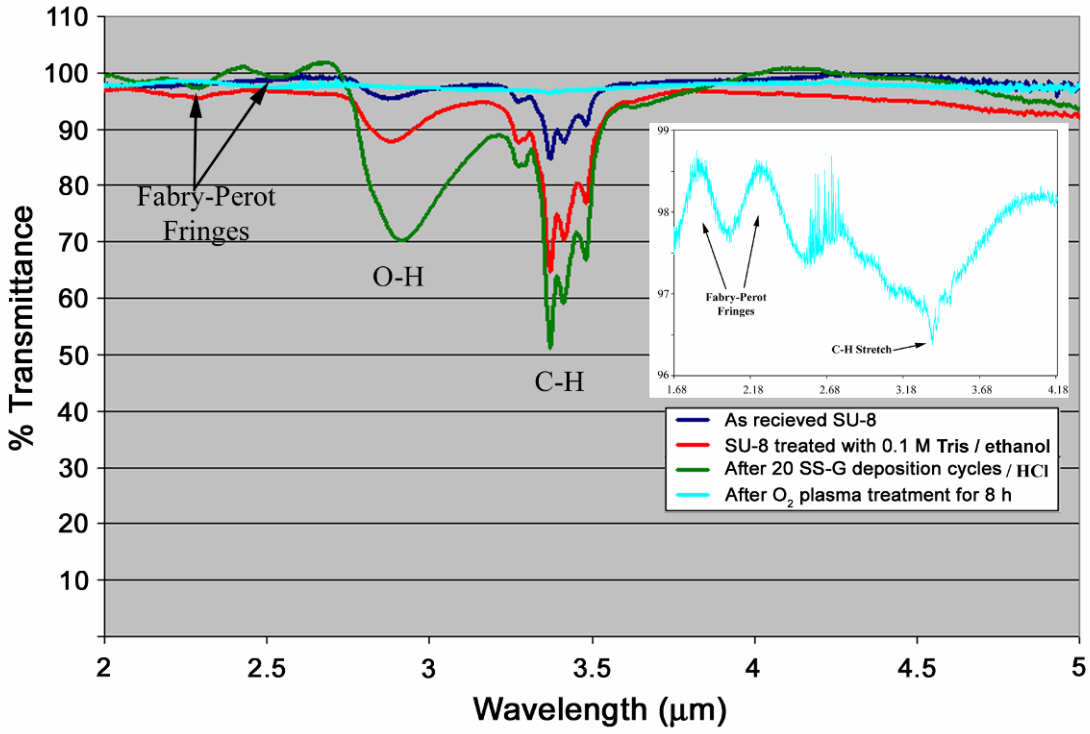

Figure 6.3: FTIR spectra obtained on the SU-8 PC after it was subjected to multiple processing steps. Note: the inset provides further clarity of the IR spectra obtained after plasma etching the coated PC structures.

After exposure for 20 min with Tris, the patterned SU-8 structures were coated with a 0.1 M Ti (IV) isopropoxide solution doped with 10 mol% Sn (IV) isopropoxide using an automated surface sol-gel pumping system. The depositions were performed as outlined in Section 6.2.3. After 20 deposition cycles, the samples were removed from the filtration flask and dried at 80^{o}C for 12 h. Figure 6.4 reveals SEM images of the as-coated structures along with a representative EDS spectrum which confirmed that both Ti and Sn were incorporated into the coating applied on the surface of the structures (Note: the C and Si peaks in the EDS spectrum were due to the underlying SU-8 polymer template and silica glass slide respectively). The images presented in Figure 6.4 were obtained at an operating voltage of 10 kV without coating the structures with gold which also provided a good indication that there was a significant loading of both Ti oxide and Sn oxide semiconducting phases on the polymer template which helped to dissipate the charge. The pore size within the SU-8 PC structure was not uniform due to the Gaussian distribution of the laser light intensity. Thus smaller pores in some regions of the crystal were more filled in with the coating than other regions, as shown in Figure 6.4.

Crystallization and transformation of the applied coating into rutile titania has required thermal treatment at 450^{o}C as demonstrated in Chapter 5. King, *et al.* reported that crystallizing a pure titania coating applied by ALD to a similar SU-8 template structure at temperatures in excess of 400^{o}C resulted in considerable damage to the photonic crystal structure [18]. The coated PC structures in the present work were also found to deteriorate after annealing at 450^{o}C. Upon thermal treatment, cracks present at the outer edges of the as-received patterned SU-8 templates were observed to propagate

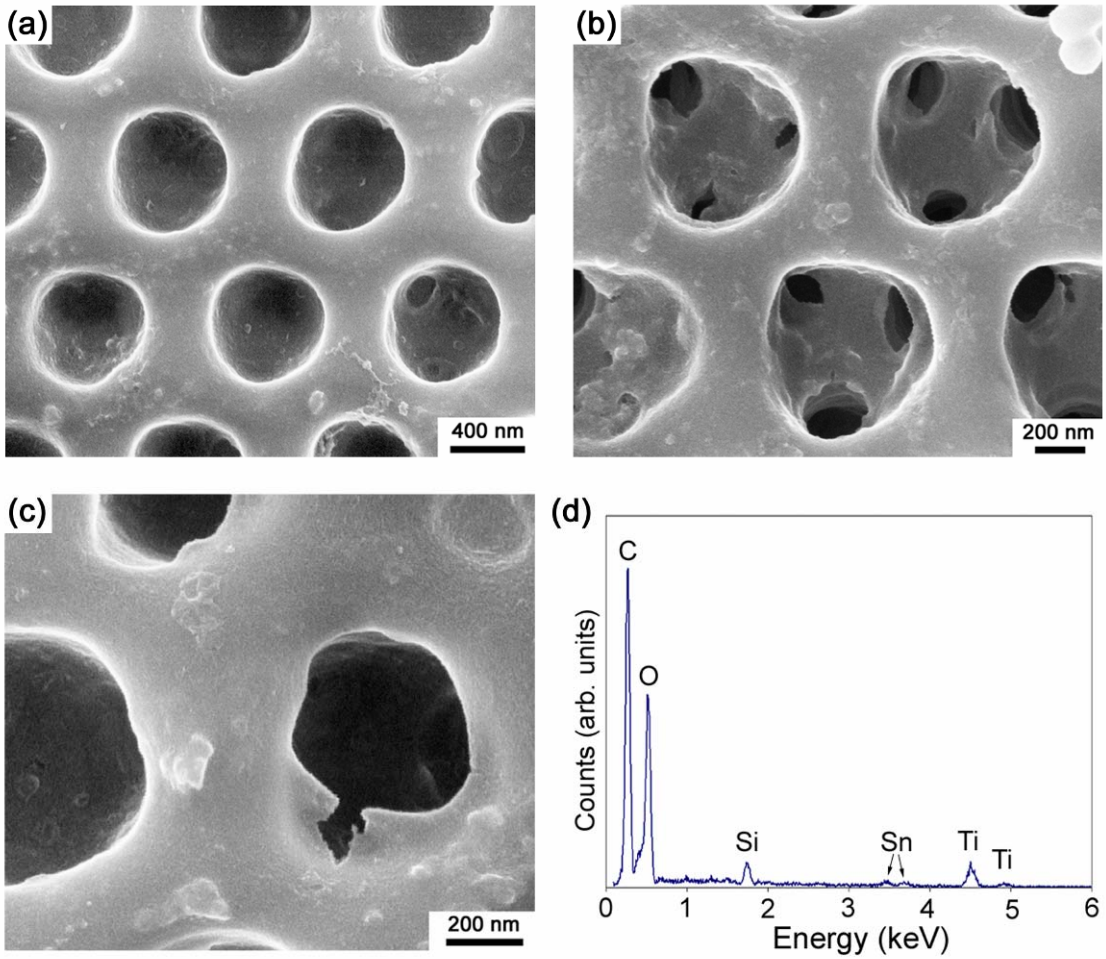

Figure 6.4: (a)-(c) SEM images of the SU-8 PC treated with Tris for 20 min and then coated with 20 surface sol-gel deposition cycles using a 0.1 M Ti (IV) isopropoxide solution doped with 10 mol% Sn (IV) isopropoxide. The corresponding EDS analysis (d) confirmed the presence of both Ti and Sn on the SU-8 PC structure.

throughout the structure. Thus, it was necessary to develop a lower temperature approach for crystallizing the applied coating.

Several researchers have reported that the amorphous-to-anatase or amorphous-to-rutile titania phase transformations can be accomplished at temperatures ranging from room temperature to 80°C in highly acidic solutions [20-24]. The majority of this research has aimed at producing rutile powders, and most of these techniques produce needle-like rutile precipitates. For example, Li *et al*. has reported that hydrolyzing $TiOCl_2$ at a pH of 0.14 resulted in needle-like rutile morphologies at 40°C [20]. They have also reported that seeding a $TiCl_4$ sol with nanosized rutile titania particles provides nucleation sites which lowered the activation energy required to form rutile during the liquid hydrolysis of $TiCl_4$ solutions [23]. Sahni, et al. reported that powder mixtures of both anatase and rutile could be obtained at 80°C by hydrolyzing titanium tetra *n*-butoxide with high concentrations of HCl [24]. Previously, Kunitake et al, demonstrated that infiltrating a latex opal structure with titanium (IV) butoxide and then submerging the coated structures in a 0.08 M HCl solution at 70°C for 48 h resulted in the conversion of the amorphous coating to anatase [25]. Of considerable note, Ristić *et al.* have demonstrated that hydrolyzing Sn (IV) isopropoxide with excessive amounts of water and then drying at 55°C for 48 h will result in the direct crystallization of the precursor to cassiterite (i.e., rutile SnO_2) [26]. In the present work, the formation of rutile titania coatings on the SU-8 PC templates was examined by simply immersing the tin oxide-doped titania-coated templates into an acidic solution.

To crystallize the coatings that were applied to the PC structures shown in Figure 6.4, the coated templates were immersed in a 0.1 M HCl solution (pH = 1.1) at 80°C for 2

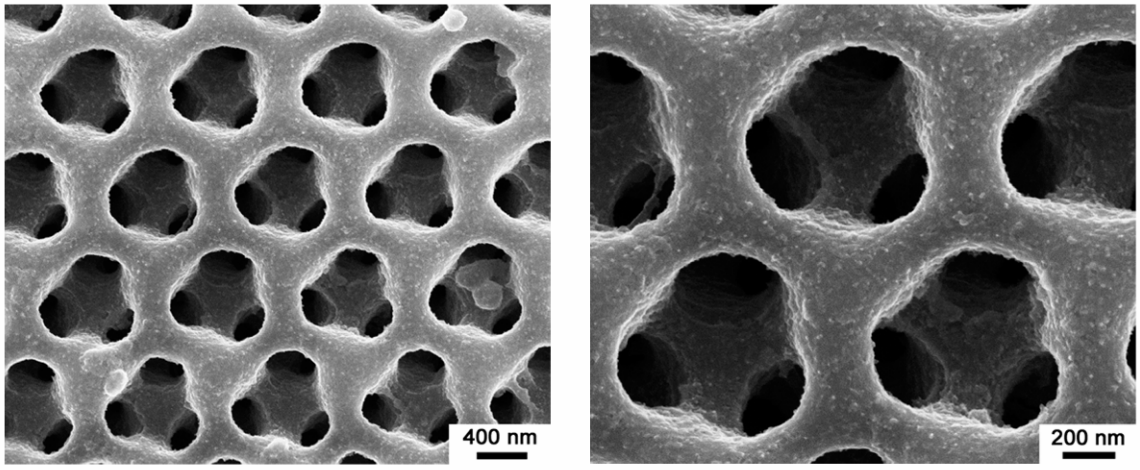

Figure 6.5: SEM images obtained after soaking the coated SU-8 PC structures observed in Figure 6.4 in a 0.1 M HCl solution at 80^{o}C for 2 days.

days. The sample was then removed and washed with copious amounts of water and dried at 80^{o}C for 3 h. Figure 6.5 reveal SEM images of the coated templates after immersion in the HCl solution. The coating appeared to be more granular than the coating observed before the HCl treatment (Figure 6.4). Also, the HCl treatment did not cause any detectable damage to the overall PC macrostructure (i.e., no apparent crack growth occured).

FTIR measurements were also performed on the coated structures treated with HCl (Figure 6.3). Deeper absorption bands for the O-H stretches were readily apparent and were attributed to adsorption of water during the HCl treatment. The C-H stretches were also enhanced as a result of the bound alkoxide precursor during the coating process. Fabry-Perot fringes (wave like features between 2-2.7 μm) were observed on the coated structures whereas they were not observed on the uncoated SU-8 template. The presence of such fringes provided a good indication to the high quality of the applied coating.

To assess the continuity of the coating on the SU-8 template and to obtain a sample for TEM analysis, the underlying SU-8 template was decomposed using an oxygen plasma treatment at 29.6W for 8 h. The oxygen species generated by the plasma (O^+, O^-, O^{2+}, O^{2-}, O, O^3 etc.) interact with the organic species present in the sample and decompose them to CO_2, CO, and H_2O products which are removed by the vacuum [27-29]. This process provides a gradual decomposition of the organic material, as opposed to rapid combustion in the case of thermal pyrolysis, and also enhances further condensation of the unreacted alkoxide molecules in the coating [27-29]. The porous network of the SU-8 template provided access of the oxygen plasma to the entire polymer lattice for complete decomposition of the SU-8. King, *et al.* utilized this technique to effectively decompose the SU-8 polymer template from their ALD coated amorphous titania structures with no apparent adverse effects to the amorphous film [18].

Figure 6.6 reveals SEM images of the oxygen plasma-treated structures. It is apparent that the inverse opal structure of the crystal remained intact after the plasma treatment. In fact, the uniformity of the entire crystal (excluding the edge regions) was comparable to that shown in the lower magnification image. EDS analyses revealed that nearly all of the SU-8 template had been removed (Note: the drastic decrease in the intensity of the carbon peak relative to the EDS analysis in Figure 6.4). The presence of the Si, Na, and Mg peaks in the EDS spectra were attributed to the glass slide which the SU-8 structure is sitting on. EDS analyses were performed over 20 different arbitrarily chosen regions of the crystal to assess the relative concentration between the Sn and Ti in the sample. The average atomic ratio between Sn:Ti was found to be 10.2% which was in reasonable agreement with the doping concentration of the precursor. This signified

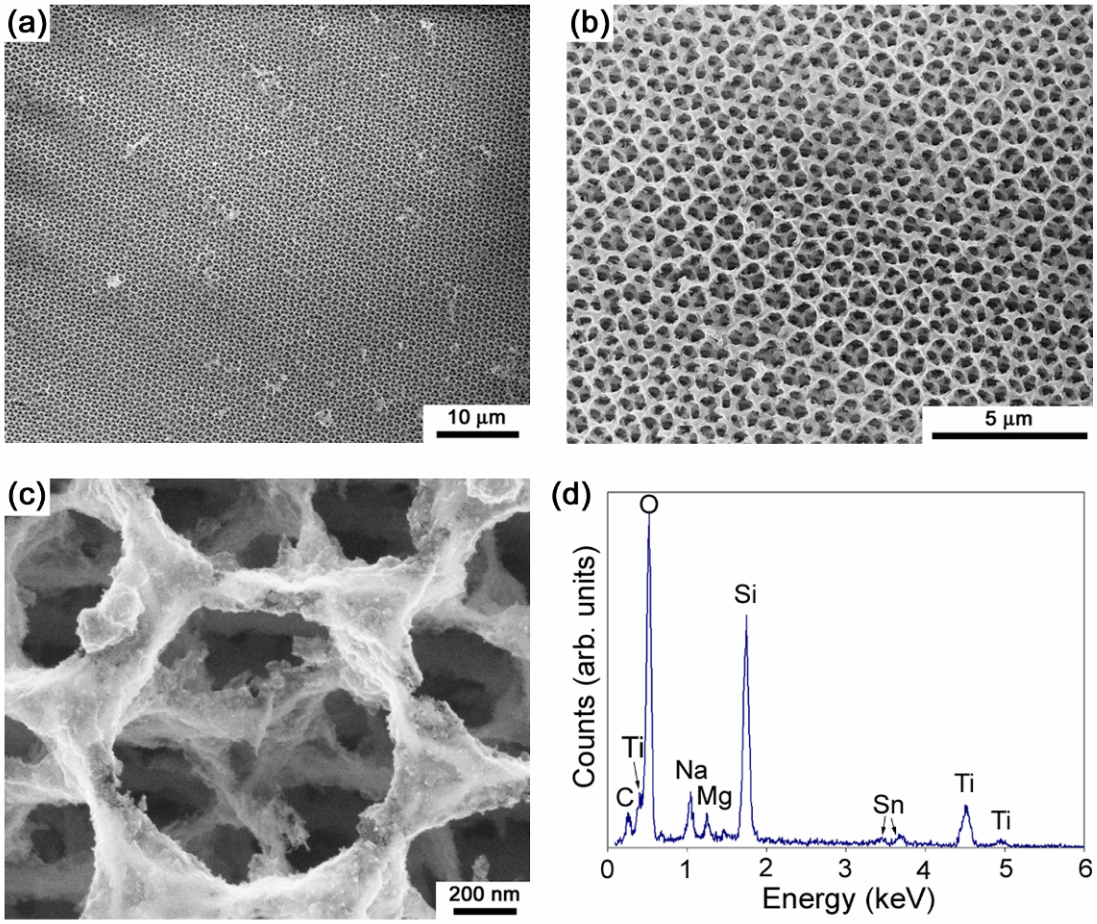

Figure 6.6: (a)-(c) SEM images of the coated PC after etching the SU-8 with an oxygen plasma. The corresponding EDS spectrum (d) reveals that nearly all of the C (i.e., SU-8) had been removed as a result of the plasma etching. The Si, Na, and Mg peaks in the spectrum are a result of the underlying silicate glass slide.

that the doped solution successfully cohydrolyzed during the surface sol-gel deposition process. FTIR analyses (Figure 6.3) confirmed that the vast majority of the underlying SU-8 structure had successfully been decomposed as a result of the plasma treatment due to the decrease in the observed C-H absorption band (observed more clearly in the inset figure). Well-defined Fabry-Perot fringes were also observed after the SU-8 had been removed. The presence of such fringes provides a further indication of the general preservation in the periodicity of the PC template after plasma removal of the underlying SU-8 template.

A TEM sample was obtained after the plasma treatment by scrapping an edge portion of the crystal with TEM tweezers and placing it on a lacey carbon TEM grid. Figure 6.7 reveals the TEM analyses which were conducted by Dr. Ye Cai (Georgia Institute of Technology). Figure 6.7(a) is a low magnification TEM image which shows a crushed specimen (due to the sample preparation) that had been treated with HCl and plasma etched. The average size of the crystallites was measured to be ~14 nm and appeared to be spherical in nature as shown in the dark field image of Figure 6.7(b). The SAED rings shown in Figure 6.7(c) were indexed to diffraction from the (110), (101), (111), (210), (211), (002), and (301) planes of rutile titania. There was also one ring which matched well with the 99.8% intensity peak for the (211) plane of brookite titania. Thus, the inverted opal structures presented in Figure 6.6 provide the first examples of a nanocrystalline rutile titania-based inverted opal structure that was fabricated from a sol-gel-coated polymeric PC template.

A mechanism for the conversion of amorphous titania to anatase has been provided by Yangisawa *et al.* [21]. They reported that water molecules (which possess

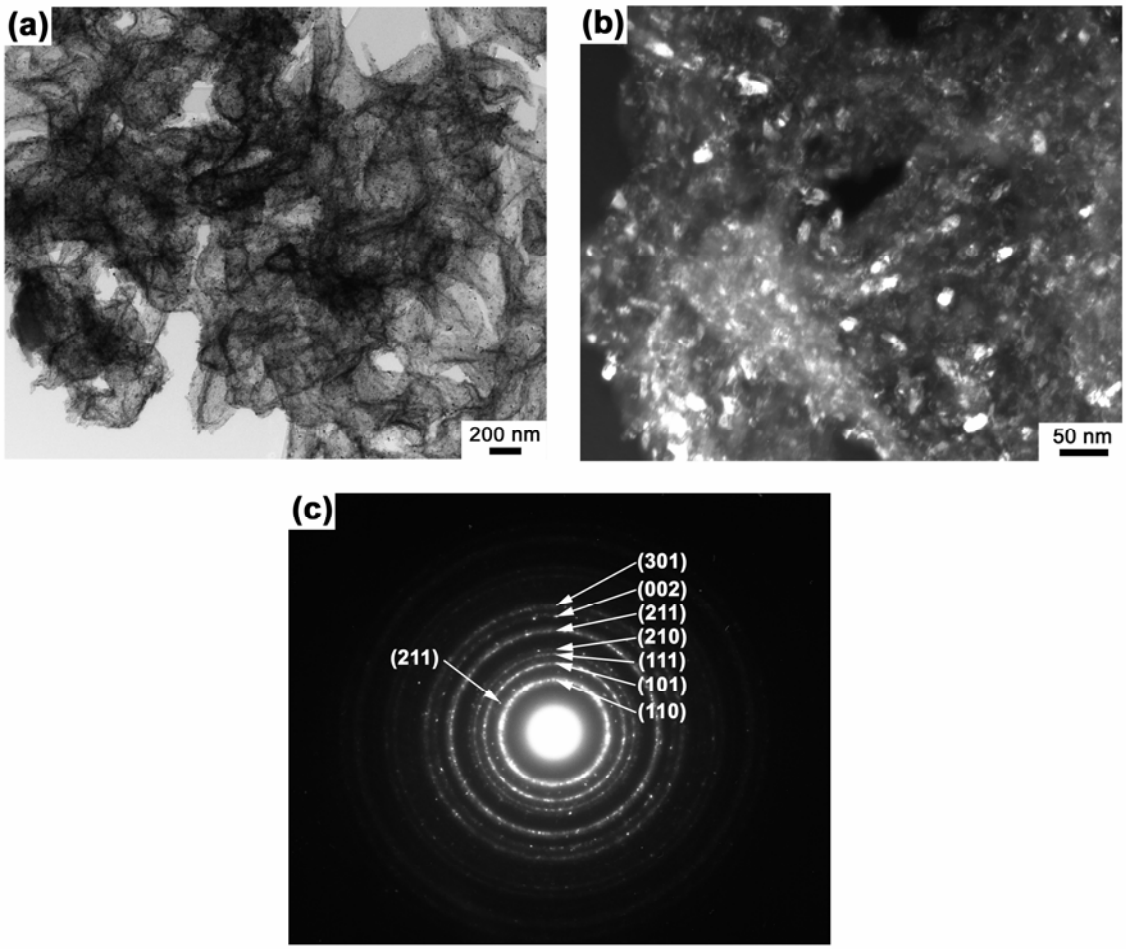

Figure 6.7: TEM analyses performed on the PC structures after they were coated and plasma etched. The lower magnification image (a) shows that the coating is continuous and made up of nanometer sized crystallites. The higher magnification dark-field TEM image (b) reveals that the crystallites are ~ 14 nm in diameter. Electron diffraction analyses (c) reveal well defined diffraction lines from the (110), (101), (111), (210), (211), (002), and (301) planes of rutile titania with one ring indexed from the (211) plane of brookite titania.

two lone pairs of electrons on the oxygen atom) will form bridges between neighboring TiO_6 octahedra, thereby aligning the octahedra so as to share faces (anatase) after dehydration. Li *et al.* further postulate that the presence of H^+ or H_3O^+ will catalyze the dehydration of the surface OH groups between the neighboring octahedra which only share one vertex, thereby causing such octahedra to share an edge [20]. In our system, the cassiterite SnO_2 phase will only align to share edges, thereby forming the rutile structure. Therefore, it is possible that as a consequence of the cohydrolysis in the tin oxide-doped titania system, the TiO_6 and SnO_6 octahedra are bridged with the water molecules to form hydrogen bonded linear chains of the octahedra. Therefore, immersing the coated structures in an acidic solution will cause dehydration of the bridging water molecule as suggested by Li *et al*. thus linking the TiO_6 and SnO_6 octahedra by edges to form the rutile structure.

6.4 Summary and Outlook

Conformal layer-by-layer coatings of rutile titania were obtained on the SU-8 patterned PC substrates using an automated surface sol-gel process. To obtain conformal coatings, the hydrophobic nature of the SU-8 template was modified using TRIS to promote the formation of surface hydroxyl groups. Contact angle wetting measurements and FTIR spectroscopy confirmed that the SU-8 were successfully functionalized with OH groups due to a decrease in the wetting angle and the increase in the OH absorption band observed in the FTIR spectra. Controlled layer-by-layer film growth was achieved on the functionalized SU-8 templates using an automated surface sol-gel pumping system to sequentially expose the SU-8 template to a tin-doped (10 mol% SnO_2) titanium (IV) isopropoxide solution followed by rinsing with an anhydrous solvent and subsequent

hydroxyl reactivation. As a result of the cohydrolysis of the tin oxide-doped titania precursor, the TiO_6 and SnO_6 octahedra are bridged with water molecules to form hydrogen bonded linear chains of the octahedra. Immersing the coated structures in a 0.1 M HCl solution led to the dehydration of the surface OH groups between the neighboring TiO_6 and SnO_6 octahedra thereby promoting such octahedra to share edges and crystallize in the rutile phase. TEM analyses revealed that the coating was nanocrystalline and comprised of ~ 14 nm rutile crystallites. Brookite was also observed in the TEM analyses. Treatment of the coated and crystallized SU-8 templates with oxygen plasma led to the gradual decomposition of the underlying SU-8 template. After removal of the template, the integrity of the crystal remained in tact which provided further indication that the coating was continuous and conformal throughout the entire photonic crystal structure. Also, the oxygen plasma treatment had no observable adverse effects on the integrity of the photonic crystal (i.e., no propagating cracks throughout the template).

This demonstration opens up new opportunities in the photonics crystal world, given that it is possible to quickly fabricate all five 2-D and all fourteen 3-D Bravais lattices using holographic lithography. Such patterned structures may now be conformally coated and converted into nanocrystalline rutile titania using the surface sol-gel process and conversion methods outlined in this Chapter.

6.5 References

[1] E. Yablonovitch, *Optics and Photonics News*, **18**, 12-13 (2007).

[2] E. Yablonovitch, *Scientific American*, **285**, 47-55 (2001).

[3] J. E. G. J. Wijnhoven, L. Bechger, W. L. Vos, *Chemistry of Materials*, **13**, 4486-4499 (2001).

[4] E. Yablonovitch, *Physical Review Letters*, **58**, 2059-2062 (1987).

[5] S. John, *Physical Review Letters*, **58**, 2486-2489 (1987).

[6] T. Wilk, S. C. Webster, A. Kuhn, G. Rempe, *Science*, **317**, 488 (2007).

[7] J.-Y. Kim, M.-K. Kwon, K.-S. Lee, S.-J. Park, S. H. Kim, K.-D. Lee, *Applied Physics Letters*, **91**, 181109 (2007).

[8] L. Zeng, Y. Yi, C. hong, B. A. Alamariu, J. Liu, X. Duan, L. C. Kimerling, *Materials Research Society Symposium Proceedings*, **891**, 251-256 (2005).

[9] Y. A. Morch, I. Donati, B. L. Strand, G. Skjak-Braek, *Biomacromolecules*, **8**, 2809-2814 (2007).

[10] R. W. J. Scott, S. M. Yang, G. Chabanis, N. Coombs, D. E. Williams, G. A. Ozin, *Advanced Materials*, **13**, 1468-1472 (2001)

[11] M. J. Escuti, G. P. Crawforf, *Optical Engineering*, **43**, 1973-1987 (2004).

[12] M. Campbell, D. N. Sharp, M. T. Harrison, R. G. Denning, A. J. Tuberfield, *Nature*, **404**, 53-56 (2000).

[13] R. Biswas, M. M. Sigala, G. Subramani, K.-M. Ho, *Physics Reviews B*, **57**, 3701 (1998).

[14] K. Bush, S. John, *Physics Reviews E*, **58**, 3896 (1998).

[15] E. D. Palik, ed., *Handbook of Optical Constants of Solids*, (Academic Press, San Diego, CA, 1985).

[16] S. Yamasaki, N. Hata, T. Yoshida, H. Oheda, A. Matsuda, H. Okushi, K. Tanaka, *Journal of Physics (Paris), Colloquium*, **42**, C4-297 (1981).

[17] X. Wang, M. Fujimaki, K. Awazu, *Optics Express*, **13**, 1486-1497 (2005).

[18] J. S. King, E. Graugnard, O. M. Roche, D. N. Sharp, J. Scrimgeour, R. G. Denning, A. J. Turberfield, C. J. Summers, *Advanced Materials*, **18**, 1561-1565 (2006).

[19] M. Nordström, R. Marie, M. Calleja, A. Boisen, *Journal of Micromechanics and Microengineering*, **14**, 1614-1417 (2004).

[20] Y. Li, N.-H. Lee, D.-S. Hwang, J. S. Song, E. G. Lee, S.-J. Kim, *Langmuir*, **20**, 10838-10844 (2004).

[21] K. Yanagisawa, J. Ovenstone, *Journal of Physics and Chemistry B*, **103**, 7781-7787 (1999).

[22] A. Pottier, S. Cassaignon, C. Chanéac, F. Villain, E. Tronc, J.-P. Jolivet, Journal of Materials Chemistry, 12, 877-882 (2003)

[23] Y. Li, Y. Fan, Y Chen, *Journal of Materials Chemistry*, **12**, 1387-1390 (2002).

[24] S. Sahni, S. B. Reddy. B. S. Murty, *Materials Science and Engineering A*, **452-453**, 758-762 (2007).

[25] Y. Li, T. Kunitake, S. Fujikawa, *Journal of Physics and Chemistry B*, **110**, 13000-13004 (2006).

[26] M. Ristić, M. Ivanda, S. Popović, S. Musić, *Journal of Non-Crystalline Solids*, **303**, 270-280 (2002).

[27] J. Huang, I. Ichinose, T. Kunitake, A. Nakao, *Langmuir*, **18**, 9048-9053 (2002).

[28] S. Fujikawa, T. Kunitake, *International Journal of Nanoscience*, **1**, 617-620 (2002).

[29] S. Fujikawa, T. Kunitake, *Langmuir*, **19**, 6545-6552 (2003)

CHAPTER 7: CONCLUSIONS

The aim of the work presented in this dissertation was to develop an inexpensive and highly versatile automated sol-gel-based deposition tool which was capable of applying controlled, conformal, and continuous metal oxide coatings on nanostructured templates. The vast majority of the work presented herein was devoted towards coating biologically-derived, 3-D, nanostructured templates. Such templates were obtained in the form of silicified microshells derived from diatom frustules, or from biopolymer chitin-based scales which decorate the wing of a blue *Morpho* butterfly and endow it with beautiful iridescent properties. These templates are attractive in nanoscience owing to their genetically-controlled nanostructures which are preserved on a massive scale through the reproduction process. Synthetic 3-D polymer-based photonic crystal structures were also utilized as nanostructured templates in this work which were fabricated by exposing a negative photoresist (SU-8) with four coherent laser beams. This technology is very promising in the rapidly expanding field of photonic crystals. However, in all cases, the native chemistry of the template has limited the device potential of the nanostructure. Thus, the intent of the work presented in this dissertation was to chemically alter the nanostructured templates with sol-gel-based coatings while preserving the fine nanofeatures of the template.

Biologically-derived silica-based diatom frustules are not chemically compatible with $BaTiO_3$. Thus, the frustules had to be converted into MgO-based replicas in order to obtain a crystallized $BaTiO_3$-based coating on the frustule. The frustules were converted to MgO using a gas/solid displacement reaction inside of sealed steel tubes. It was found that by reacting the frustules with Mg(g) in a molar ratio as high as 2.5:1 ($Mg:SiO_2$), the

fine features of the frustules were well preserved in the MgO/Si composite replicas. It was also shown that the proximity of the reactant oxide relative to the vapor source will have a direct impact on the extent of conversion inside of the sealed steel tubes. Deposition of a barium titanate-based alkoxide precursor on the MgO/Si-based composite replicas was achieved by utilizing a reflux/evaporation protocol. It was shown that severe mud-cracking of the coatings could be avoided by charging the system with a higher template surface area which allowed for the polymerization of the precursor to take place on more available adsorption sites. The underlying magnesia could then be dissolved with hydrochloric acid so as to yield barium titanate replicas of the diatom frustules. Photoluminescent diatom frustules were obtained by doping the barium titanate alkoxide precursor with europium nitrate. The Eu^{3+}-doped $BaTiO_3$-bearing frustules exhibited bright red emission upon stimulation with a 337 nm (UV) light source. This work demonstrated the feasibility of synthesizing photoluminescent microparticles of controlled shape and size through the use of biologically derived microshell templates. However, coating the nanostructured diatom frustule templates using the reflux-evaporation method did not provide control over the coating thickness on the frustules. This deposition method also produced excess inorganic particles in the solution and on the frustules.

An automated surface sol-gel system was built to overcome the issue of uncontrolled sol-gel-derived coating thicknesses on the nanostructured templates. The system was designed around vacuum filtration and utilized a computer to control peristaltic and vacuum pumps which pumped solutions into a filter unit containing the sample and subsequent evacuation of the solutions. The peristaltic pumps were housed

within a controlled-atmosphere dry nitrogen glove box to prevent premature hydrolyzation of the alkoxide precursors. This system added an element of control for performing the surface sol-gel process which has been lacking over the past decade.

Tin oxide coatings were applied on silica-based diatom frustules using the automated surface sol-gel system. An organic hyperbranched amine-acrylate coating was developed to amplify the hydroxyl concentration (by terminating the acrylate layer with glucosamine) on the surface of the frustules. It was shown that surface sol-gel reactions were initiated on the frustules that possessed an amplified concentration of hydroxyl groups provided by this hyperbranched method, however, coatings were not initiated on the native silica frustules or the frustules that were treated with an oxidizing RCA-1 solution. The continuity of the coating that was obtained on the hydroxyl rich frustules was assessed using transmission electron microscopy and electrochemical (gas-sensing) analyses.

Rutile titania coatings were accessible on the scales of a blue Morpho butterfly wing by doping a titanium alkoxide precursor with a rutile nucleating agent (i.e., Sn (IV) isopropoxide). Controlled layer-by-layer film growth was achieved using an automated surface sol-gel pumping system to sequentially expose the wing specimens to a tin-doped (15 mol% SnO_2) titanium isopropoxide solution followed by rinsing with an anhydrous solvent and subsequent hydroxyl reactivation. The thickness and structural integrity of the coating on the scales was dependent upon the number of deposition cycles performed. Rutile titania replicas of the scales were obtained after a modest heat treatment at 450^{o}C for 4 h in air. Control experiments, performed by coating the scales with non-doped titania precursors, demonstrate the need for utilizing doped precursors to obtain rutile

TiO_2 coatings with nanocrystalline grains which thereby preserve the intricate nanoarchitectural framework of the scales. Precipitation trials revealed that the anatase to rutile titania phase transformation can be completely avoided by doping the titanium (IV) isopropoxide solution with as little as 7 mol% tin (IV) isopropoxide.

Rutile titania coatings were also applied on holographically-defined synthetic polymer (SU-8) photonic crystal templates. The surface of the SU-8 template was first functionalized using tris(hydroxymethyl)aminomethane (TRIS) to provide hydroxyl functionalities to initiate adsorption of the alkoxide precursor. Contact wetting angle measurements and FTIR spectroscopy confirmed that the SU-8 template was enriched with hydroxyl functionalities. Controlled layer-by-layer film growth was achieved on the SU-8 templates using an automated surface sol-gel pumping system to sequentially expose the functionalized SU-8 template to a tin-doped (10 mol% SnO_2) titanium (IV) isopropoxide solution followed by rinsing with an anhydrous solvent and subsequent hydroxyl reactivation. The cohydrolysis of the tin oxide-doped titania solution on the SU-8 surface provided TiO_6 and SnO_6 octahedra that were bridged with water molecules to form hydrogen bonded linear chains of the octahedra. Therefore, immersing the coated structures in a 0.1 M HCl solution led to the dehydration of the surface OH groups between the neighboring TiO_6 and SnO_6 octahedra thereby promoting such octahedra to share edges and crystallize in the rutile phase. Indeed, transmission electron microscopy analyses confirmed the coating was polycrystalline and comprised of ~ 14 nm rutile titania crystallites. The underlying SU-8 template was gradually decomposed by exposing the coated template to an oxygen plasma treatment. This reaction protocol, i.e., controlled surface sol-gel depositions with a tin-doped titanium (IV) isopropoxide

precursor, crystallization in an acidic solution, and removal of the organic template with an oxygen plasma, led to an inverse opal rutile titania photonic crystal structure. This is the first reported instance in which a rutile titania coating with such small grain size has been obtained on such structures.

It is the author's opinion that the surface sol-gel process will find a niche in the world of nanocoatings. The results presented in this dissertation demonstrate that the obtained coatings from the surface sol-gel process are continuous, conformal, and nanocrystalline. The versatility of this process has also been demonstrated by applying conformal coatings on a variety of substrate surfaces (i.e., ceramic, bio-polymer, synthetic polymer). Also, multi-component chemistries are accessible which range from common alkoxide solutions (e.g, barium titanium ethyl-hexano isopropoxide) or by mixing two compatible alkoxides together as was the case for the Ti (IV) isopropoxide and Sn (IV) isopropoxide solutions. This opens new avenues to access different chemistries that are not easily accessible by other layer-by-layer techniques which require volatile reactants.

APPENDIX A: OPERATION OF THE AUTOMATED SURFACE SOL-GEL PUMPING SYSTEM

The automated surface sol-gel pumping system is controlled using LabView 8.0 as described earlier in Chapter 2 of this dissertation. The purpose of this appendix is to provide a detailed step-by-step explanation of how to operate the pumping system. This appendix is written with simplistic instructions to provide a novice user with step-by-step instructions explaining how to operate the system.

LabView Instructions

1. Open the LabView 8.0 software by double clicking the LabView 8.0 icon on the desktop.
2. Open the program named "Automated Sol-Gel.vi" located under the "Open" window. An Automated Sol-Gel.vi window will then appear as shown in Figure A-1. Each of the green LED buttons (labeled 0-6) correspond with either the blow dryer, vacuum pump, or peristaltic pumps. LabView 8.0 opens programs in the edit mode (note the checkerboard appearance of the background shown in Figure A-1) and so it is possible to change the name of the pumps in this mode. However, it is not possible to operate the pumps in the edit mode.
3. To change from the edit mode to the run mode click on "Operate" and then "Change to Run Mode" as shown in Figure A-2 (Note: the checkerboard background appearance will disappear).
4. To run the "Automated Sol-Gel.vi" program, the arrow in the upper left hand corner must be depressed as shown in Figure A-3. After depressing the arrow, the various system components can be turned on and off by clicking the LED buttons.

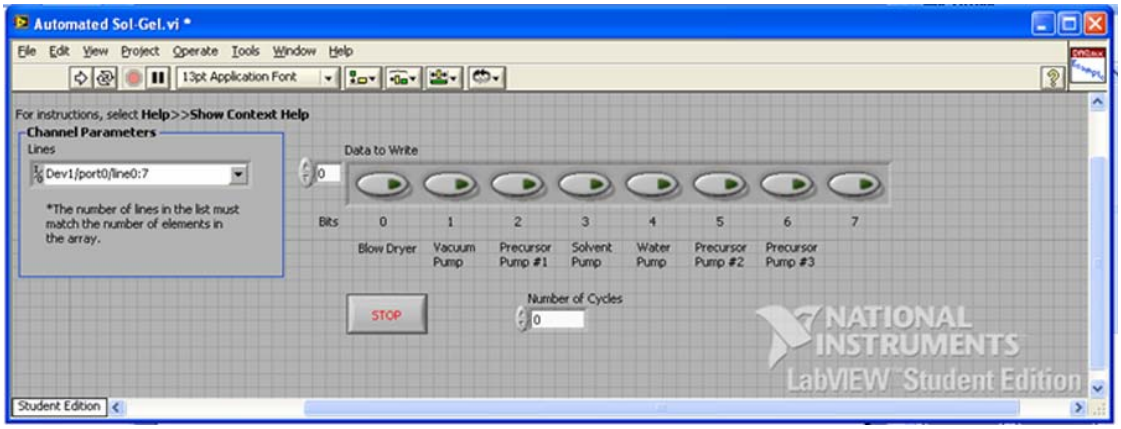

Figure A-1: Automated Sol-Gel.vi LabView program used to control the automated pumping system. Each of the green LED buttons will control whether a system component is turned on (LED button is illuminated) or off (LED button is not illuminated). The checkerboard appearance of the window background signifies that the program is in the edit mode.

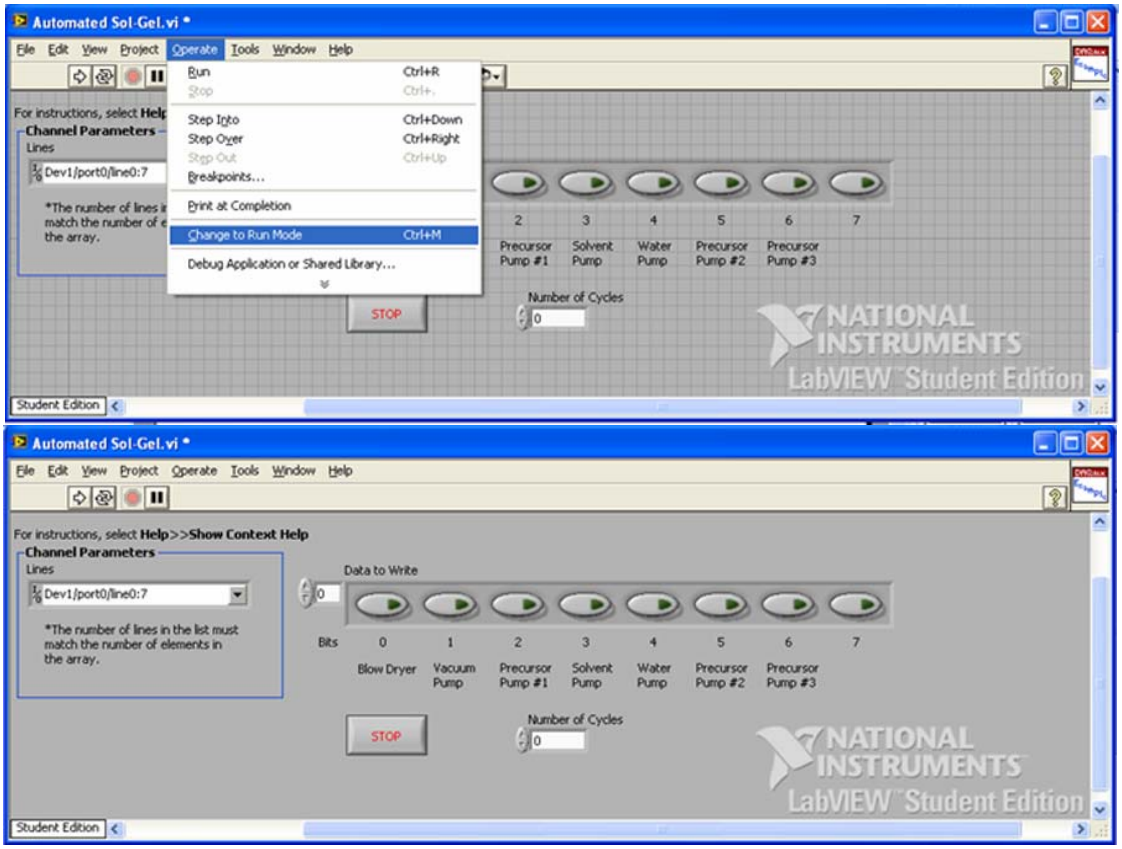

Figure A-2: Changing from edit mode to run mode (Note: the checkerboard appearance of the background disappears once you click on "Change to Run Mode").

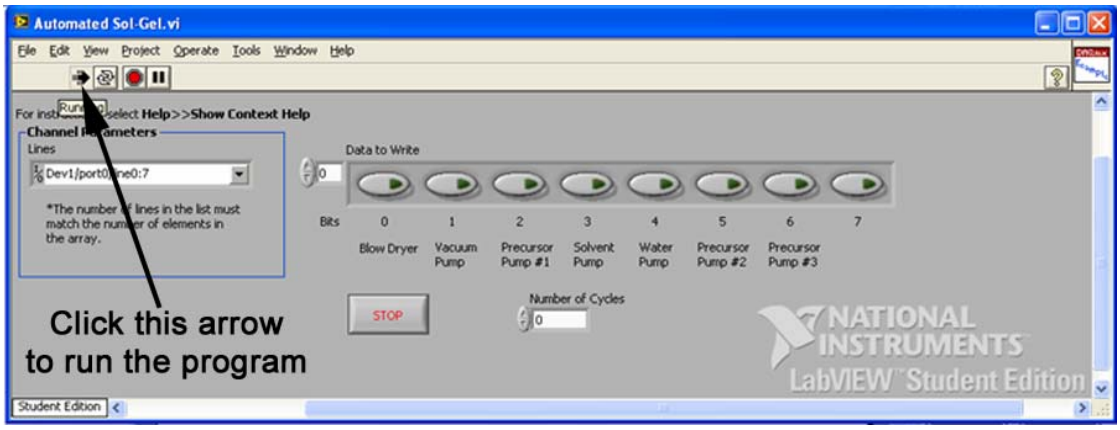

Figure A-3: To run the "Automated Sol-Gel.vi" program the "run" arrow must be depressed as shown above. Once the arrow is depressed the various system components can be energized by simply clicking on the corresponding green LED button.

The automated surface sol-gel system components can be controlled by clicking on the LED buttons once the "Automated Surface Sol-Gel.vi" is in the run mode. AutoIt V3 was used in this dissertation to automate the mouse clicks which turned the LED buttons on and off to control the individual system components. Due to the cyclic nature of the coating process, the AutoIt program was coded for one complete coating cycle and then it was looped for the desired number of deposition cycles. A sample program is provided below.

Each of the LED buttons of the "Automated Surface Sol-Gel.vi" program is located at specific X and Y pixel coordinates on the screen. To obtain these X and Y coordinates, the AutoIt program has a window info screen which will provide the coordinates of the location of the mouse at any position on the screen. To access the AutoIt window info screen click on "Start" then "AutoIt V3" then "AutoIt Active Window Info". A window will appear as shown in Figure A-4. The window is activated by clicking any random position on the screen. The X and Y mouse coordinates (circled

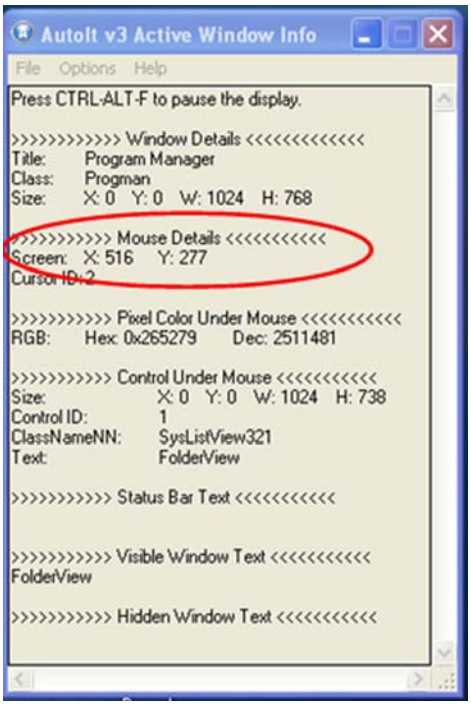

Figure A-4: AutoIt Active Window Info window which is used to obtain the X and Y mouse coordinates to plug into the AutoIt control code.

in red in Figure A-4) will change pixel-by-pixel via any mouse movement. Thus, to obtain the X and Y coordinates of any of the LED buttons on the "Automated Surface Sol-Gel.vi" program, simply position the mouse cursor over the desired LED button and record the coordinates.

AutoIt utilizes a very simple Visual BASIC-like language which is fairly straight forward. To automate the mouse clicks the code requires the desired function (such as mouse click), which button to click (right or left), the X and Y coordinates (obtained from the AutoIt Ative Window Info screen) of the desired mouse click, and the number of desired mouse clicks. To control how long a pump is turned on you simply tell the program to "Sleep" for that amount of time (Note: the programming language is written for millisecond time scales). The number of coating iterations is simply controlled in a

loop and can be altered in the third line of the sample code provided below. To stop the program at any time the operator simply depresses Ctrl-Alt-x at the same time, otherwise, the program will continue to run for the programmed number of deposition cycles.

Once the code is entered the operator can run the script by double clicking the program Icon or by right clicking on the program icon and then clicking on "Run Program". In the sample program provided below the green text after the semicolon in each line of the program explains the function of the code.

Sample AutoIt Program Utilized to Control the "Automated Surface So-Gel.vi" Program

```
; Script Start - Add your code below here

HotKeySet("^!x", "MyExit")
For $i = 1 to 15 Step 1; For 15 successive coating iterations
MouseClick("left", 455, 158, 1, 0); Turn on Precursor Pump
Sleep(1000); Allow precursor recirculation pump to run 1 second
MouseClick("left", 455, 158, 1, 0); Turn off Precursor Pump
Sleep(300000); Allow precursor to react with the surface for 5 minutes
MouseClick("left", 396, 158, 1, 0); Turn on Vacuum Pump
Sleep(18000); Allow vacuum pump to run for 18 seconds to evacuate
precursor
MouseClick("left", 516, 158, 1, 0); Turn on the solvent pump
Sleep(4000); Allow solvent pump to run 4 seconds
MouseClick("left", 516, 158, 1, 0); Turn off the solvent pump
Sleep(10000); Allow solvent to be evacuated
MouseClick("left", 516, 158, 1, 0); Turn on the solvent pump
Sleep(4000); Allow solvent pump to run 4 seconds
MouseClick("left", 516, 158, 1, 0); Turn off the solvent pump
Sleep(10000); Allow solvent to be evacuated
MouseClick("left", 516, 158, 1, 0); Turn on the solvent pump
Sleep(4000); Allow solvent pump to run 4 seconds
MouseClick("left", 516, 158, 1, 0); Turn off the solvent pump
Sleep(18000); Allow solvent to be completely evacuated
MouseClick("left", 396, 158, 1, 0); Turn off the Vacuum Pump
Sleep(20000); Allow vacuum to completely dissipate
MouseClick("left", 575, 158, 1, 0); Turn on the Water Pump
Sleep(4000); Allow water pump to run 4 seconds
MouseClick("left", 575, 158, 1, 0); Turn off the Water Pump
Sleep(60000); Allow water to react with sample for 1 minute
MouseClick("left", 396, 158, 1, 0); Turn on Vacuum Pump
Sleep(18000); Allow the vacuum pump to run for 18 seconds to evacuate
the water
MouseClick("left", 516, 158, 1, 0); Turn on the solvent pump
Sleep(4000); Allow solvent pump to run 4 seconds
MouseClick("left", 516, 158, 1, 0); Turn off the solvent pump
Sleep(10000); Allow the solvent to be evacuated
MouseClick("left", 516, 158, 1, 0); Turn on the solvent pump
Sleep(4000); Allow solvent pump to run 4 seconds
MouseClick("left", 516, 158, 1, 0); Turn off the solvent pump
Sleep(10000); Allow solvent to be evacuated
MouseClick("left", 516, 158, 1, 0); Turn on the solvent pump
Sleep(4000); Allow solvent pump to run 4 seconds
MouseClick("left", 516, 158, 1, 0); Turn off the solvent pump
Sleep(300000); allow vacuum to asperiate past the sample for 5 minutes
to dry the sample
MouseClick("left", 396, 158, 1, 0); Turn off Vacuum Pump
Sleep(60000); Allow the vacuum to fully dissipate from the system for 1
minute
MouseClick("left", 459, 271, 1, 0); Increment the number of cycles by 1
Next
Func MyExit()
    Exit
EndFunc
```

VITA

Michael Raymond Weatherspoon was born in Idaho Falls, Idaho on October 1, 1977, the son of David and Denice Weatherspoon. After graduating from West Side High School in Dayton, Idaho in 1996, he served a two year mission for the Church of Jesus Christ of Latter-Day Saints to Raliegh, North Carolina. After returning from his mission, Michael married Kendra Rae Peterson in February of 1999. Michael attended one semester of college at the Idaho State University, Pocatello, Idaho, before transferring to the University of Idaho, Moscow, Idaho, in the Fall of 1999. In the Spring of 2002, Michael and Kendra were blessed with their first child, Sydney Rae Weatherspoon. Michael received his Bachelor's of Science degree from the University of Idaho in Metallurgical Engineering in the Spring of 2003. Michael transferred to the Georgia Institute of Technology in the Fall of 2003 for graduate studies. In the Spring of 2005, Michael and Kendra were blessed with their second child, Jacob Michael Weatherspoon. In April of 2008, Michael earned the degree of Doctor of Philosophy in Materials Science and Engineering.